國立台灣大學電機資訊學院生醫電子與資訊學研究所

博士論文

Graduate Institute of Bio-informatics and Bioelectronics,

College of Electrical Engineering and Computer Science

National Taiwan University

Doctoral dissertation

智慧電漿子實驗室晶片系統之核酸感測研發

Smart Plasmonic Lab-on-a-Chip System for DNA based Biosensing

吳子珩

Tzu-Heng WU

指導教授：林啟萬 博士/林致廷 博士/歐赫里昂 布雍 博士

Advisor: Chii-Wann LIN ,PhD/ Chih-Ting LIN ,PhD /Aurélien BRUYANT ,PhD

中華民國 106 年 3 月

March 2017

doi:10.6342/NTU201700804

Acknowledgement

Well, can’t believe that this is the moment. After all the excitement, frustration and hard works, here we are, a guy tapping along in front of his computer, thinking back about this bitter sweet journey, like countless of other traveler before him.

My shear gratefulness is not only upon the completion of the thesis, that is just the final product of the work. I am glad for all those amazing explorations that we have made during the process. To begin with, I thank prof. Chii-Wann LIN and prof. Aurelien BRUYANT for support me in every single aspect to pursuit for a joint PhD. Until today, I still feel excited about this precious chance to learn how to foster international collaboration, to travel between two great institutes where different idea meets and to listen to amazing perspectives. None of this would have come true, if it were not you, my two mentors, who have the experience and wisdom to build up the first NTU-UTT joint PhD case. I am glad that we have published enough of works that draw more chance of funding and resources, that , I sincerely hope, will open up more channel for other PhD students to have the same opportunity to start their adventures. Again, I attribute the glory to my wonderful advisers.

I thank all my lab mates and “helpers”, in France and in Taiwan, 陳盈秀、王姿懿、陳一銘、王超、范樂陶、許偉恩、楊景旭、林威佐、任恩、呂彗歆博士、魏世忠博士、張家禎博士、莊崇亮博士、尤濬博士、Yi Haung、julien Vaillant、彭瑛、Mme. Pascal Denis、Dr. Abeer Mohtar、李后珊、沈庭瑤、Mandy Lee、prof. Gilles Lerondel, you made my PhD student life a wonder and enjoyable one. Thanks for your help in solving administrative work, for providing insightful discussions, for helping me on connection, for sample preparation, for helping of opto-electronics and DNA sequence design and for all your supports.

I thanks my family and my wife for their understanding and encourage. There are just too many people that I owe you my sincere thanks and gratitude, but don’t worry finding your name here, you have my thank deep in my hearts.

doi:10.6342/NTU201700804

摘要

近年來，人口快速增長伴隨著社會老齡化，為醫療照護系統帶來日漸沉重之負擔。因應此社會現象，居家定點照護成為許多學術研究以及新創產業的熱門方向。透過適當的設計，結合消費性電子元件強大的軟硬體，以往僅能在實驗室運作的生物感測器將可以被引入居家生活中提供即時而精確的醫療診斷。

本論文旨在探索如何運用智慧型手機作為整合之核心平台，建構可攜式表面電漿共振生物感測器實驗室晶片系統。於論文第一部分，利用單股核糖核相對於雙股核糖核酸更能夠有效地避免鹽類誘發之金奈米粒子聚集特性，我們於智慧型手機上建構了一個核糖核酸檢測裝置。在此一平台，智慧型手機扮演了幾個重要的角色。首先，透過 3.5 釐米音訊孔與自製電路之整合，智慧型手機可以驅動 650 奈米之射源，並透過輸入電極接收雷射光訊號，來進行金奈米粒子吸收度量測。透過軟體鎖相放大器來解調射源之震盪訊號，百分之八十以上的環境雜訊可以被排除，使該平台成為一個具有-63 dB 優良訊躁比的顯色儀。最後，所有資訊可以直接在自製之應用程式上被顯示、分析，不需要任何額外裝置。透過我們提出的平台，我們能夠在智慧型手機上，於十五分鐘內解析最低 0.77 nM 的核糖核酸樣品，甚至優於某些商用桌面型可見光－紫外光光譜儀在單一波長的解析極限。

接續第一部分的實驗，我們提出了一種全新的相位式表面電漿共振生物感測器。許多文獻指出，相位式表面電漿感測器比強度式更加的靈敏(約 100 倍)。然而，因為需要相位震盪器、易受到同徑雜訊影響以及需要過多光學組件等諸多議題的限制，相位式表面電漿感測器之商業化應用至今仍未成功，遑論手持式應用。然而，相位式表面電漿感測器的額外靈敏度，在定點照護中具有相當重要的價值。為此，本論文提出了剪干涉式表面電漿共振生物感測器。剪干涉式表面電漿共振生物感測器，具最小化同徑干擾效應、減少光學零組件需求、以及透過電流調變作為相位調等優點。為了處理強度與相位同頻率震盪的干涉訊號，本論文提出一種新的相位擷取方式。此方法，改良自泛用式鎖向放大器，可以在相位震盪深度($\Delta\phi_a$)為 3.83 且已知雷射波長-電流調變係數(S)等特殊條件下，解調出相位資訊。在電漿層膜厚為 47 奈米的情況下，剪干涉式表面電漿共振生物感測器可以達到 1.26x10^{-6} RIU 之最低解析度，約比強度式靈敏 20 倍。透過適體修飾以及心肌蛋白之檢測，本論文也初步展示剪干涉式表面電漿共振生物感測器之應用潛力，並提出一套結合嵌入式系統以及消費性電子元件之應用架構。

關鍵字：表面電漿共振生物感測器、消費型電子元件、鎖相放大、相位檢測、實驗室晶片系統、核糖核酸

doi:10.6342/NTU201700804

Abstract

This thesis is dedicated to integrate consumer electronics devices (CED) with advanced plasmonic sensors into Lab-On-a-Chip system for point-of-care application, with a main focus on design of compact plasmonic sensor.

In the first part of the thesis, a short strand DNA biosensor combining single-wavelength colorimetry and digital Lock-in Amplifier within a smartphone is proposed. The principle of the detection is that single strand DNA tends to protect gold nano-particle from salt induced aggregation, as compare to double strand DNA. The salt induced aggregation is then detected from absorbance at 650 nm wavelength. Using 3.5 mm audio channel to integrate laser driver and photo-detector, together with a tailor-made software lock-in amplifier (sLIA), we have achieved a 15 mer DNA detection down to 0.77 nM within 15 minutes on smartphone. Due to sLIA, the measurement noise-to-signal ratio is greatly reduce to -63 dB, which lead to four times smaller limit-of-detection as compared to a desktop UV-Vis spectrometer.

Encouraged by the results of the first part, we proceed to explore the possibility of smartphone based interferometric plasmonic sensor. Conventionally, phase sensitive Surface Plasmon Resonance (SPR) biosensor is not viable outside laboratory setting due to cost and performance consideration. Therefore, to pursue portable SPR application with high sensitivity, in the second part of the thesis, a Shearing Interferometer based Surface Plasmon Resonance (SiSPR) biosensor, which has not been reported elsewhere, is proposed. The SiSPR chip uses shearing interferometer without the need of extra optical parts. This design together with differential interferometry greatly reduce noises. To avoid the use of costly phase modulator, a current induced sinusoidal wavelength modulation is applied with a novel phase extraction method. We demonstrate that the detection limit of the SiSPR, at 47 nm of plasmonic layer thickness is down to 1.26x10^{-6} RIU, about 20 times better than amplitude sensing. From our data, we estimate that SiSPR can be more sensitive if film thickness is near 49 nm. We have also demonstrated preliminary results on protein sensing using aptameric probe. The further integration of SiSPR with CED and future perspectives are incorporated in the end of the thesis.

Key words: Lab-On-a-Chip, DNA aptamer, Consumer Electronic Device, Surface Plasmon Resonance, Lock-In, Phase detection

doi:10.6342/NTU201700804

Table of Content

doi:10.6342/NTU201700804

Table of Content of Figures

doi:10.6342/NTU201700804

doi:10.6342/NTU201700804

Chapter 1. General introduction

The past ten years have seen two major socio-economic factors affecting the research field of handheld sensors, notably for health-related applications. The first factor is related to the continuous increase of the world population, which is reaching 7.5 billion this year. If we look at the population structure across the developed countries, we find that around 12~20% of the population is over 65 years. The ageing and the growth of such a large population has fundamental consequences on the entire society, especially on medical care delivery system. According to statistical data from Organization for Economic Co-Operation and Development (OECD)[5], in France, the maintenance of socio-health care system takes up nearly 11% of the annual Growth Domestic Product (GDP), which corresponds to about 230 billion of euros per year[a]. In Taiwan, also the health sector takes up around 6.6 % of the GDP annually. In other words, a tremendous burden is now placed on our health care delivery systems due to the ever-growing population as well as longer life expectancy.

The second major and obvious trend is the booming of consumer electronic device market such as smart phones, feature phones and tablets. Around 70% of the world population owns at least one mobile devices. These devices are undoubtedly the most

---

[a] Considering that France has a GDP of 2133 billion in 2016.

ubiquitous and powerful devices ever for integrating Point-Of-Care (POC) sensors. Smartphones are already equipped with a number of integrated sensors and now offer a large processing power, but they also possess sufficient inputs and outputs for a wired or wireless control of external sensors and data acquisition. For example, the smartphone audio jack (cf. **Fig. *1***), with proper electronic integration, serves as a 16 bits analog/digital converter (1 input, 2 outputs) - which is comparable to a number of performant acquisition cards – to extract and process data from sensors. In addition, the audio jack has synchronized data capture time resolution down to 26 μs per point, which is sufficient, in principle, to perform higher end fluorescence time measurements (such as FLIN[b]), or to

Fig. 1 Overview of smartphone I/O capacity

---

[b] FLIN : Fluorescence-lifetime imaging microscopy

extract amplitude and phase of signals modulated at relatively high frequency. To date, the audio jack channel has notably been used in Electrocardiogram (ECG) and pulse oximetry type of measurement[6]. For optical detection systems, we should also mention that smart devices often come with optical sources in the back of the phone (white LED for photo), as well as the front LED screen. Interestingly, the front LED may serve as light source having three emission wavelengths as shown in **Fig. *2***.

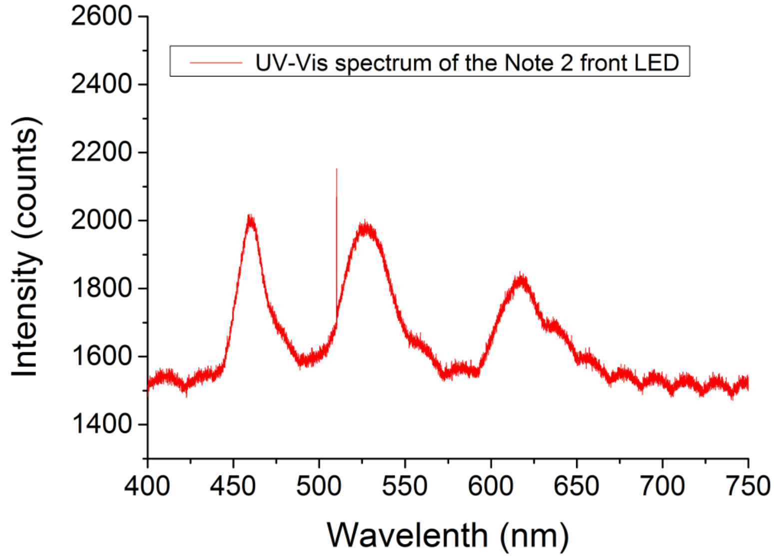

Fig. 2 Samsung Note 2 front LED panel emission spectrum
The spectrum is measured via a commercial UV-Vis spectrometer in National Taiwan University. The Samsung Galaxy note 2 is arbitrarily choose for demonstration.

In some works, the light emitted from smart devices was used to carry our Surface Plasmon Resonance (SPR) detection[7], which is one of the preferred method for bio-sensing. As for the optical detection side, the built-in smartphone CMOS[c] camera can also

---

[c] CMOS : Complementary metal–oxide–semiconductor. The CMOS sensor is now more common than the CCD camera in consumer electronic devices.

doi:10.6342/NTU201700804

be used as a point detector for optical powermeter measurement[4, 8, 9]. Finally, regarding connectivity, we should note that smartphones provide seamless connection to other embedded system through USB-OTG[d] or wireless access. Except for high power devices, the connection can also provide a stable power supply to small diagnostic devices.

Therefore, with a more and more equipped population facing health issues, the concept of m-health[e] is emerging as a disrupting health care approach. The generalized use of smartphone as a smart platform for Point-Of-Care (POC) technology could certainly alleviate part of the healthcare costs and increase global disease prevention. With POC diagnostic tools integrated in smartphone, a large portion of the population across the world and developing countries could benefit of a new, decentralized, medical access, in contrast with conventional health care delivery model. As a result, the cost of transporting medical resource to hospital and number of medical personnel can be reduced. This scenario is supported by reports from public sector. For example, the US Food and Drug administration recently mentioned in *Mobile Medical Applications* (2015):

~"*The Food and Drug Administration (FDA) recognizes the extensive variety of actual and potential functions of mobile apps, the rapid pace of innovation in mobile apps,*

---

[d] USB-OTG : USB On-The-Go. This common term specifies that the USB device performs both master or slave roles in establishing a communication link with another USB device via specific protocols.

[e] *m-health* stands for "mobile health" and typically refers to diagnostics or intervention done through smartphones or equivalent devices. The term e-health (electronic-health) is more generic.

doi:10.6342/NTU201700804

and the potential benefits and risks to public health represented by these apps."

We have also seen World Health Organization stating that [10]:

~"*Mobile technologies have the potential to bridge systemic gaps needed to improve access to and use of health service, particularly among underserved populations.*"

Beyond public sector, we have also been observing a fast growth in the m-health market[11] with the emergence of new products.

To sum up, diagnostic tools traditionally centralized in laboratories and hospitals have the opportunity to be integrated onto mobile Consumer Electronic Devices (CEDs) to provide timely diagnostic assistance without geographic and temporal hindrance. However, such goal cannot be simply realized without gathering cross-disciplinary skills and efforts to produce the required integrated technologic platforms. The sensor optical designs, the electronic readout, the software integration have to be considered carefully, and most importantly, relevant diagnostic scenario with identified end-users have to be proposed to promote the m-health approach.

In this thesis, we want to tackle part of these objectives by proposing smart integrated optical devices for mobile-based POC diagnostic. To achieve this goal, we combine the know-hows of the Micro-Sensor and System Laboratory of the biomedical department of National Taiwan University (NTU) and the Laboratory of Nano-optics and Optical Instrumentation (LNIO) of the Université de Technologie de Troyes (UTT). In the context of m-health, the constraints we set on ourselves it that the system should sensitive, very affordable, and versatile in term biologic targets. To achieve this goal, we focus on

doi:10.6342/NTU201700804

biosensors based on well-established Surface Plasmon Resonances and work on the system integration and performance improvement strategies beyond the state-of the-art for handheld devices.

In the first part of the thesis, we focus on building a DNA biosensor combining single wavelength colorimetry and digital Lock-In Amplifier (LIA) within a smartphone. In this section, we explore the possibility of utilizing audio jack in building a LIA-based optical biosensor. First, we give an introduction on the background of conventional method for integrating gold nano-particle colorimetry (AuNP) colorimetry with smartphone. A detailed literature review on smartphone based diagnostic tool is then given, which should serve to provide a general background for the thesis. The working principle of classical Lock-In Amplifier (LIA), the synthesis of AuNP, and the hardware /software integration are provided. We discuss the relevance of the smartphone audio-jack channel for conducting such measurement by evaluating its performances. Finally, at the end of this first part of the thesis, we demonstrate a 15-mer DNA detection within 15 minutes of diagnostic time down to 0.77 nM, using a software-based LIA.

In the second part, we take advantage of the developed LIA approach to explore phase-sensitive measurement of Surface Plasmon Resonance (SPR) biosensor for future portable application. As will be discussed, compared to traditional SPR, phase sensitive based SPR usually excels in terms of sensitivity. Such superior sensitivity can be highly

doi:10.6342/NTU201700804

desirable when the sensor is challenged with complex bio-sample (i.e., urine, saliva or serum). In this part, we present a novel phase sensitive detection design, named "Shearing Interferometry based Surface Plasmon Resonance" (SiSPR). SiSPR, together with a novel phase extraction method, will be demonstrated. To show the feasibility of SiSPR in diagnostic application, we have targeted am atherosclerosis relevant protein—cardiac Troponin I (cTnI)—as potential biomarker. Performance of SiSPR, surface modification of the chip as well as a scheme for constructing laboratory prototype will be detailed.

doi:10.6342/NTU201700804

Part 1. DNA biosensor combining single-wavelength colorimetry and digital Lock-in Amplifier within a Smartphone

doi:10.6342/NTU201700804

Chapter 2. Introduction to smartphone based colorimetry

With the possibility of increasing the accessibility of medical resources and reducing health expenditure, smartphone based diagnostic tool has been a focus of research recently[4, 7, 9, 12]. This trend stands on several important facts. First, a smartphone contains numerous powerful devices that can transform it into a laboratory level sensing device. In contrast to the relatively bulky and expensive gold standard diagnostic tools, such as UV-Visible spectrometer, a smartphone based diagnostic tool offers an alternative diagnostic solution that can be applied in point-of-care setting. With about 4.75 billion mobile users around the world[11], smartphone based diagnostic tools may become the most efficient approach to deliver medical assistance across geographical boundaries[13], as outlined in the general introduction.

Among a range of possible diagnostic tools, smartphone camera based gold nano-particle colorimetry (SCB-AuNP colorimetry) has shown great potentials[3, 14-16]. The use of add-on camera replaces the need of a spectrometer to quantify the colorimetry results, thereby making on-site AuNP colorimetry feasible, such as on-site DNA sensing. In SCB-AuNP colorimetry DNA detection, a single strand DNA (ssDNA) used as probe is added to the solution to protect AuNP from aggregation under salt solution. When a *target* complementary ssDNA presents in the solution, hybridization between probe and target occurs. The resulting double strand DNA (dsDNA) is much more rigid in its molecular

doi:10.6342/NTU201700804

structure and therefore cannot protect AuNP from aggregation as effectively as ssDNA. The aggregation leads to an apparent color change of the AuNP solution, which can be detected via smartphone camera. The color change of the particle corresponds to a spectral shift in the plasmonic resonance of the gold nanoparticles, which is directly related to the effective particle size. The captured image is then analyzed and processed via a specific application. Taking advantage of the User Interface (UI) offered by smartphone, the user can then obtain a well-processed diagnostic report in real-time.

Although SCB-AuNP colorimetry shows good potential for POCT application, the use of camera as optical detector also sets up certain important limitations. First, the add-on camera generally provides a low bit depth (typically 8-bit), limiting the ultimate sensitivity of the SCB-AuNP. This is especially true if we compare this to the 16-bits available via the audio phone jack, where an optical detector can be plugged. Secondly, smartphone camera is very slow in data acquisition (~100 Hz maximum) while the audio jack-reading channel can reach 44.1 kSample/s. The low time resolution prevents SCB-AuNP colorimetry to bridge with more sophisticated tool such as lock-in amplifier (LIA) detection, where high working frequency is preferably used to reach higher signal to noise ratio. In other words, in order to further improve the sensitivity and detection mechanism of smartphone based colorimetry, a new way of implementing colorimetry on smartphone is desirable. To achieve such goal, we propose a new metrologic approach for

doi:10.6342/NTU201700804

implementing colorimetry on smartphone. In our method, the audio jack is used in replacement of the camera to build a low cost yet powerful AuNP colorimetry featuring Smartphone-Based digital LIA (SBLIA). The approach is referred to as SBLIA-AuNP colorimetry in the following.

Herein, SBLIA-AuNP colorimetry sensor is presented and analyzed in detail. Through a tailor-made circuit board, the smartphone audio output channel sinusoidally drives the injection current of a 650 nm laser in the kHz range. As the beam travels through the AuNP solution, the modulation amplitude of the output beam decreases with increasing concentration of the dsDNA in the sample. The audio input channel then reads the beam intensity from a photo-diode and the smartphone process the data with an implemented software LIA. The implemented software LIA picks up our source signal components at the designated frequencies and filters out the noises. Finally, based on the modulation intensity obtained, the user can readily monitor the absorbance of the sample through the UI. Since audio jack plays a vital role as a function generator in our measurement, an examination of the audio jack performances including working frequency limit, intrinsic noise type is first provided. Then, the noise spectrum of the system and corresponding optimized measurement conditions are discussed. Finally, a DNA detection is carried out as an example to demonstrate the efficacy of our system.

doi:10.6342/NTU201700804

Chapter 3. Literature review on smartphone based diagnostic tool

In recent year, smartphone has been widely applied in physical sensors for diagnostic purposes. Due to the ubiquitous existence of audio jack, the audio jack has been considered not only as a source of sensor integration but also for energy harvesting. For example, through a diode bridge, audio jack AC output voltage can be transformed into DC power supply[17] (cf. **Fig. 3**). The power hijacking can be used to power up certain diagnostic devices with low power consumption. For example, Verma et. al. have applied the audio jack as a source for electro-cardiogram measurement (ECG)[1]. In more advanced model, smartphone also comes with USB 3.0 protocol where a 5V output with 400 mA upper current limitation is provided.

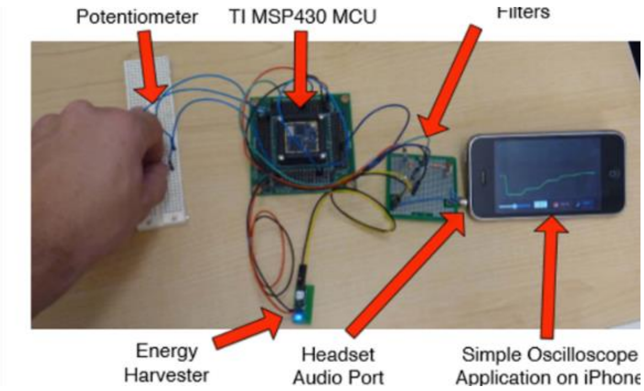

Fig. 3 Power hijacking from audio jack.

Beyond conventional physical sensor like ECG or pulse oximeter[6], complex bio-chemical sensors have also been proposed (cf. **Fig. 4**). In 2014, Jiang et al. from Cornell university

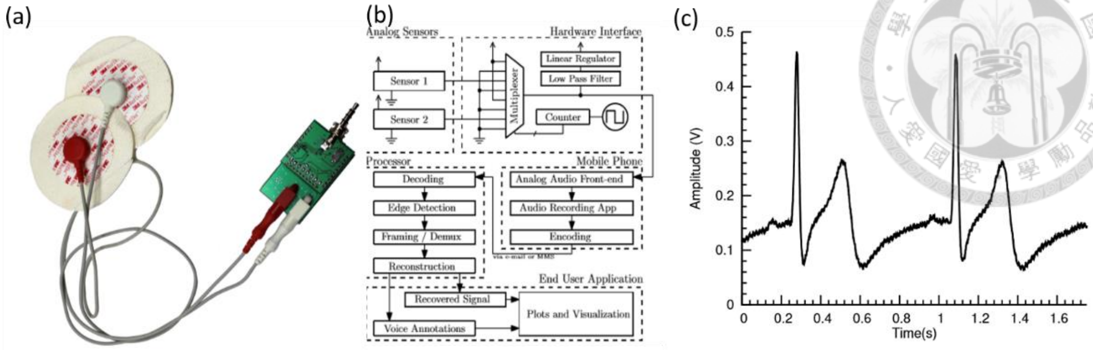

Fig. 4 Audio jack based ECG measurement device from Ann Harbor University[1] .

have notably reported[4] “Solar thermal polymerase chain reaction for smartphone-assisted molecular diagnostics” (cf. **Fig. 5**). The authors showed that, using a micro-controller unit (MCU), smartphone can readily monitor the temperature conveyed by sun light to heat a micro-flow through polymerase chain reaction (PCR) disk. In this way, energy consumption of the PCR is kept at minimum and thus rendering both durability and portability of the device. Through the use of a primer sequence, viral DNA of Kaposi’s Sarcoma herpesvirus is amplified by PCR reaction for detection of the virus. The product of PCR is then monitored by an add-on camera to feedback the detection results.

Besides PCR, colorimetry is yet another diagnostic tool where smartphone add-on camera find new application[18] (cf. **Fig. 6**). For example, also in 2014, Wei. et. al. from University of Los Angeles, California, have demonstrated a smartphone-based water mercury pollution sensor using gold nano-particle colorimetry (AuNp colorimetry)[3].

In the mentioned work, 10-mer DNA is added to the gold nano-particles as a probe

doi:10.6342/NTU201700804

sequence (5’-TTT TTT TTT T-3’). When Hg^{2+} is present in the solution, the probe DNA is forced to leave the AuNps, forming a Hg^{2+} complexed double helix, resulting in

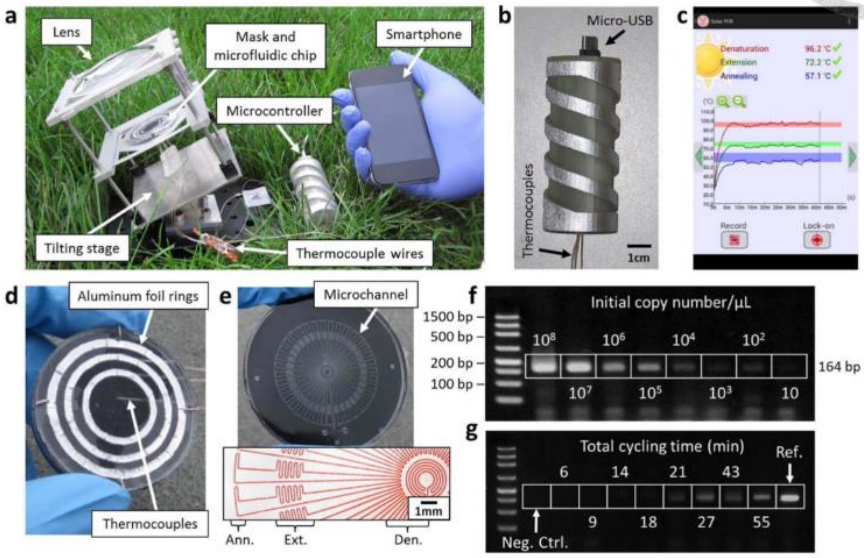

Fig. 5 Smartphone based Karposi’s Sarcoma herpesvirus detection[4].
(a) an overview of sensor device (b) micro-controller and temperature sensor unit. (c) user-interface of the application (d) heating unit of micro-flow through PCR disk. (e) structure of the proposed micro-flow through PCR disk (d) electrophoresis result of the PCR (for verification purposes).

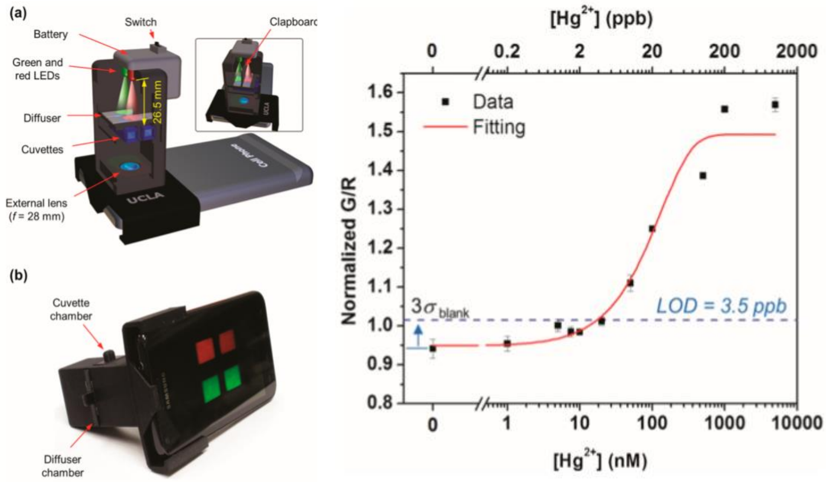

Fig. 6 Smartphone based AuNp colorimetry biosensor for monitoring water pollution[3]
(a) an overview of sensor device (b) calibration curve of the sensor

salt induced aggregation of the AuNp solution. The color shift is then detected via a smartphone with its rear add-on camera. The device helps to quantify the level of absorption (using the ratio between the absorption at a wavelength λ=532 nm and λ=625 nm) of the AuNp solution, and consequently to determine the level of Hg^{2+} in water. The tailor-made sensor is reported to have a limit of detection down to 3.5 ppb which reaches the gold standard of the public health sector.

Beside Localized Surface Plasmon Resonance (LSPR) biosensor, such as AuNP colorimetry, we can also find fiber based SPR integration on smartphone platform. A group of researcher from Purdue University in US has demonstrated the possibility to combine fiber based SPR within the smartphone[19] In this work, the smartphone back LED is filtered and coupled to an optical fiber where part of the fiber is peeled and coated with a gold film (cf. ***Fig. 7***). The fiber output light intensity is measured with the smartphone rear camera. The measured sensitivity in terms of Refractive Index Unit (RIU) is around 7×10^{-5} RIU, which is a bit less sensitive as compared to commercial products (2.5×10^{-5} RIU for BIOSUPLAR™, a commercial SPR from HANDTAKE™ GmbH). To demonstrate the bio-sensing efficiency, the fiber based SPR smartphone sensor is tested with Immunoglobin G (IgG), as shown in **Fig. *8***.

Beside smartphone approach, other systems use tailor-made circuit that contain micro-controller and processor to perform LSPR measurements [2]. As shown in the

doi:10.6342/NTU201700804

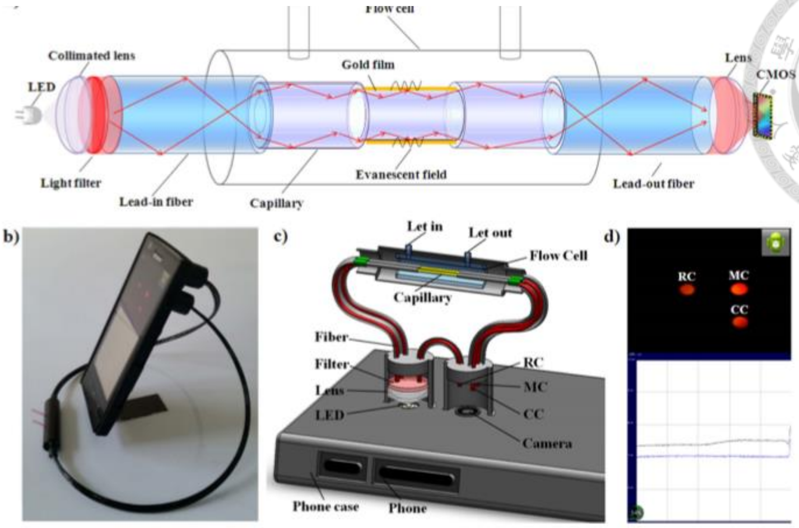

Fig. 7 fiber based SPR biosensor coupled to smartphone.

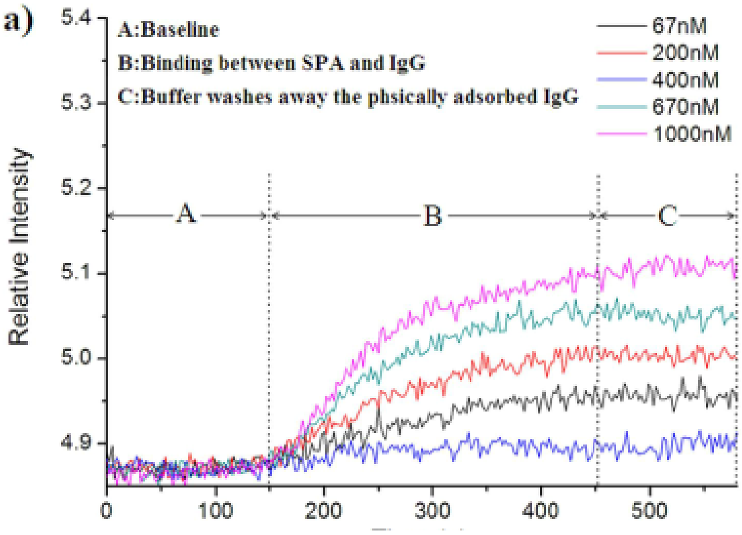

Fig. 8 Probing IgG on smartphone based fiber SPR.

Fig. 9, integrated LSPR system contains motors, imaging system, thermal controller unit, a display as well as a LIA system. It allows multiplexing detection of nine region of interest. Other interesting examples including fluorimeter and other SPR based sensor[9, 14, 20] could also be mentioned. Not all these recent results are reported here for the sake of conciseness, the important point here being to provide a view on how smartphone can be

doi:10.6342/NTU201700804

transformed into optical sensor platform and to outline its capabilities.

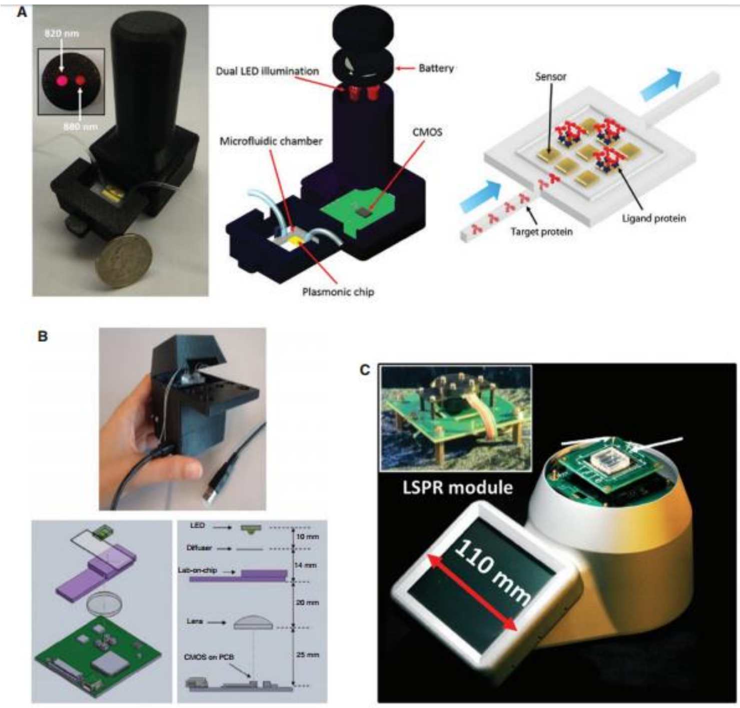

Fig. 9 Portable LSPR sensor integrated system[2].

Chapter 4. Material and methods

Section 4-1. Theoretical background of Lock-in Amplifier

While LIA operation is a very well-documented electronic technique which is used for long, its implementation as a software in smartphone has not been reported yet and we can briefly remind its working principle as we intend to use it for AuNP colorimetry. In a typical LIA detection, the source signal is modulated at a specific frequency:

$$f(t) = V\,sin(2\pi f_S t + \varphi) \quad \textbf{Eq. 1}$$

where φ is phase of the signal, V is the amplitude of the modulation and f_s is the frequency of the modulation. The essence of the LIA is to mix the signal with two reference functions, i.e. a sine and a cosine, and to generate the corresponding “X” and “Y” output:

$$X = \frac{2}{\tau}\int_0^{\tau} V\,sin(2\pi f_S t + \varphi)\,sin(2\pi f_R t)dt \quad \textbf{Eq. 2}$$

$$Y = \frac{2}{\tau}\int_0^{\tau} V\,sin(2\pi f_S t + \varphi)\,cos(2\pi f_R t)dt \quad \textbf{Eq. 3}$$

As it is well known, due to the orthogonality property of the sinusoidal function, only when frequency of the signal (f_s) equals to the frequency of the reference signal (f_R), will X and Y have non-zero output, which means that we have, for a sufficient integration time τ :

$$if\ f_s = f_R, \begin{cases} X = Vcos(\varphi) \\ Y = Vsin(\varphi) \end{cases} \qquad if\ f_s \neq f_R, \begin{cases} X = 0 \\ Y = 0 \end{cases} \quad \textbf{Eq. 4}$$

doi:10.6342/NTU201700804

and using these X and Y outputs, we can find amplitude (V) and phase (φ) of the source signal. The amplitude and phase are then given by:

$$V = \sqrt{X^2 + Y^2} \quad \textbf{Eq. 5} \; and \;\; \varphi = arctan2(X, Y) \quad \textbf{Eq. 6}$$

We note that the integration time τ determines the number of periods summed in order to determine the amplitude V. Thus, increasing τ provides an averaging effect to suppress noise, as we will see in later section.

In our case, the signal is the modulated laser intensity, and its amplitude of modulation is monitored via the LIA output (V). Some other important properties of LIA should also be noted here. First, the LIA outputs exclude all the signal frequencies from DC to the highest frequency possible, except the signal at the reference frequency. In other words, the LIA can be simply regarded as a powerful, narrow, bandpass filter that helps to greatly exclude out-of-band signal. This is a very favorable characteristic in point-of-care application, where ambient light variation and noises are expected. In other words, the proposed SBLIA- AuNP colorimetry is not vulnerable to ambient light change nor do we need a nicely sealed measurement environment to provide accurate results.

Section 4-2. Digital LIA algorithm

The algorithm of digital LIA can be found in **Fig. 10**. In SBLIA, the raw waveform, received by the audio jack, is first digitally mixed with the reference signal. Then, it is

doi:10.6342/NTU201700804

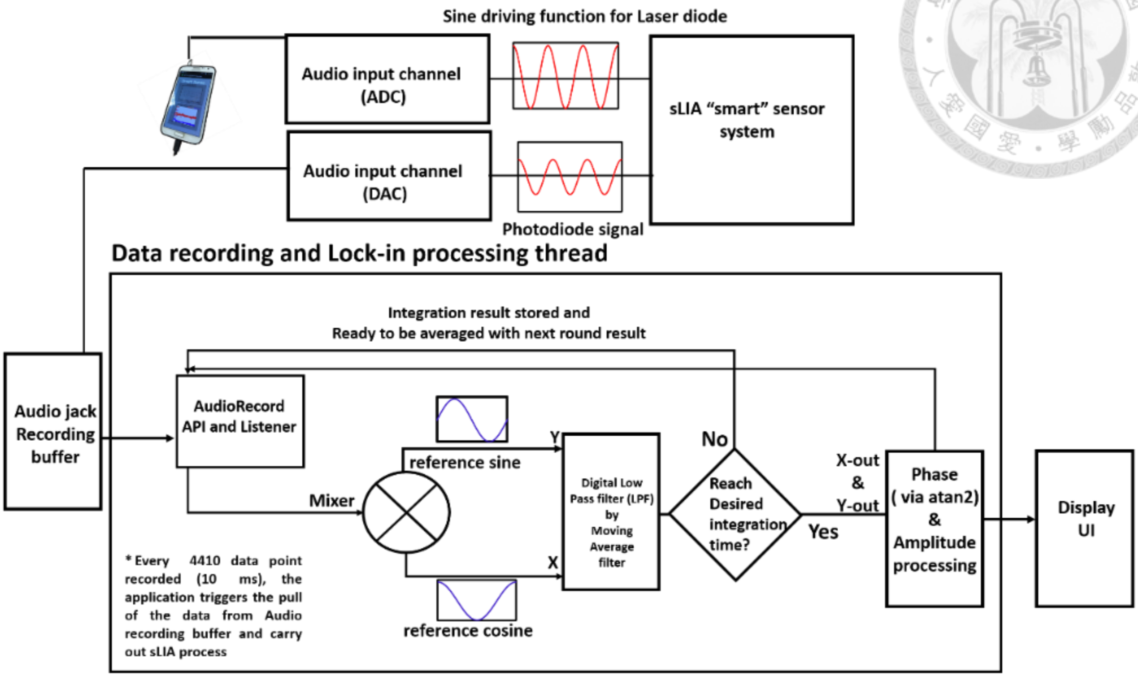

Fig. 10 Digital Lock-In Amplifier Algorithm.

passed through a digital low pass filter (LPF) which is realized by an averaging filter. The low pass filter controls the integration time (τ) of the LIA. The value of τ can be adjusted during the experiment through the UI. Increasing τ will increase the number of data point being averaged. This action narrows LIA pass band and consequently reduces the noises.

Section 4-3. SBLIA-AuNP colorimetry system

The SBLIA system design can be seen in **Fig. 11 (a)**, while the top view and side view of the system can be seen in **Fig. 11 (b)** and **(c)**. During SBLIA-AuNP colorimetry DNA sensing measurement, AuNP sample with different levels of target DNA is placed in the cuvette for measurement. The intensity of the laser diode (ADL65052TL from Roithner LaserTechnik) is sinusoidally modulated. The modulation waveform is provided by the

doi:10.6342/NTU201700804

audio output channel. A voltage offset to the laser is needed to drive the laser in a linear working range. In this work, the smartphone USB-OTG is used to provide an offset to the laser. During detection, the laser beam travels through the AuNP sample. The modulated output intensity is collected by a FDS-100 Si photodiode from Thorlabs Inc. and read by the audio input channel. The implemented digital LIA then extract amplitude information, using the recorded signal waveform data (upper window in “Oscilloscope” in **Fig. 11 (d)**). The amplitude sensogram is presented to the user as shown in the lower window in **Fig. 11 (d)**. When the sample’s absorption increases/decreases, the amplitude of the laser modulation decrease/increase correspondingly. The absorbance of the sample can then be inferred from the data. The opto-mechanical holder made in PMMA helps either to fix the system on a table for laboratory application or to work as a portable detection unit. The smartphone arbitrarily used in this work is a Galaxy Note 2 from Samsung. We note that audio channel does not follows a universal industrial protocol, and is therefore subject to minor changes in reading and output capacity. However, the audio cards of the mainstream mobile phones have comparable performances, and the following investigation serves to provide the important essence of implementing SBLIA for biosensing application that remains universal between different smart device models.

doi:10.6342/NTU201700804

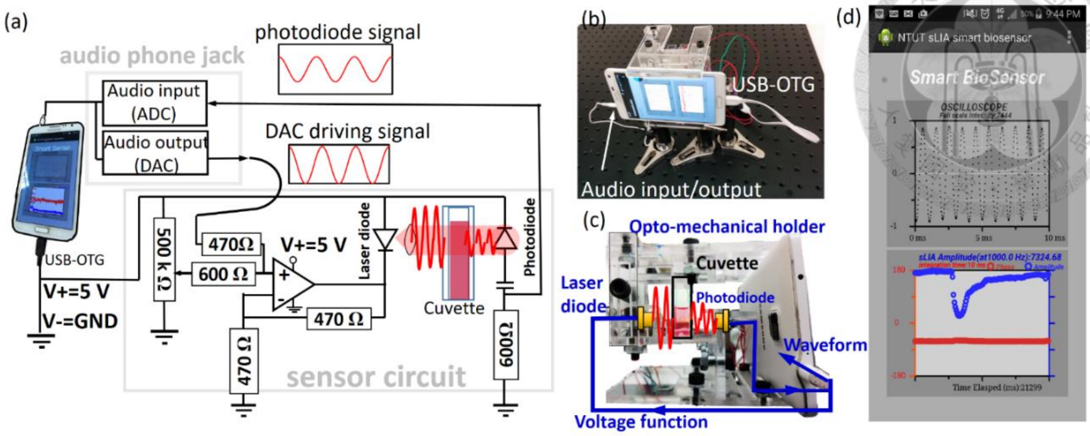

Fig. 11 SBLIA-AuNP colorimetry system overview.
(a) The electrical circuit and the system diagram of SBLIA system (b) reveals system front view, and (c) is the system side view. (d) User-Interface (UI) of the android application. The upper plot shown in the UI is the normalized raw waveform data from audio input channel. The lower plot is the phase/amplitude sensogram data.

Section 4-4. AuNP preparation

The oligonucleotides used for DNA detection experiment were synthesized by Purigo^{TM} Biotech, Taipei, Taiwan and were further purified by high performance liquid chromatography (HPLC). The probe DNA strand used in the sensing experiment is a 15-mer DNA with a sequence of CTA ACA CCC CAC TCA, and the target strand is the complementary strand of the probe. This sequence is designed so that no self-hybridization can occur. The gold nanoparticle is prepared using citrate mediate reduction. A 100 mL aqueous solution of $HAuCl_4$ (41 mg, 1.0 mM) was heated to reflux and stirred vigorously. Later on, a 10 mL of tri-sodium citrate (114 mg, 38.8 mM) solution was quickly added to this solution. The solution was then heated for 10 min and was allowed to cool to room temperature while being vigorously stirred. Before AuNP solution is finally stored at 4 degree, some filtering is necessary. The average diameter of AuNPs was found to be around 13 nm, as determined with a particle size analyzer.

Section 4-5. Sample preparation for target DNA detection

The procedure for target DNA detection is comprised of three steps: DNA hybridization, AuNP-DNA incubation and then the colorimetry measurement.

Step1. (DNA hybridization)

6.4 μL of 10 μM probe ssDNA is incubated with a designated amount of 10 μM target DNA in a 1 ml vial. These 6.4 μL of probe ssDNA correspond to 200 nM in the final detection process. Meanwhile, 0, 0.8, 1.6, 3.2, 4.8 μL of 10 μM target DNA will correspond to 0, 20, 40, 80, 120 nM of target DNA in the final detection. To facilitate optimized hybridization conditions, we add 3 μL of 2 M NaCl and fill the solution with TBE buffer to 27 μL. Finally, we incubate for 5 minutes.

Step2. (AuNP-DNA incubation)

We add 250 μL of AuNP and 150 μL of de-ionized water to the sample solution prepared in step 1, then we incubate 10 minutes before colorimetry measurement (**Step 3**).

At this point we can point out a possible troubleshooting:

The color change may not be very prominent. In such case, we need to adjust the salt concentration in step1 to optimize the colorimetry result. This will greatly enhance the color contrast between samples with different target DNA.

doi:10.6342/NTU201700804

Section 4-6. Converting SBLIA-AuNP colorimetry measurement data into absorbance unit (AU) for comparison

Fig. ***12*** shows a typical result of SBLIA-AuNP colorimetry sensogram. In order to compare important system properties, e.g Noise-to-Signal Ratio (NSR) and Limit of Detection (LOD), between SBLIA and UV-Visible spectrometer, the sensing result must be weighted to obtain the same measurement units. In contrast to a UV-Visible spectrum, the SBLIA will provide a digital value corresponding to an optical intensity that require a conversion. In the present context, absorbance reference level is defined by the AuNP solution that contains only 200 nM probe DNA and zero target DNA (This will be defined as “blank sample” hereafter). Therefore, the data from the SBLIA-AuNP measurement can be converted to AU by definition of absorbance:

$$A_c = -log\left(\frac{I_c}{I_{c=0}}\right) \quad \textbf{Eq. 7}$$

Where I_c is the SBLIA intensity as a function of target DNA concentration C in AuNP. $I_{c=0}$ is the SBLIA intensity when blank sample is placed in the cuvette.

In case of UV-Visible spectrometer, our UV-Visible absorbance data uses air transmission as the reference level (i.e, 100% transmission). In such case, when AuNP solution contains target DNA with a concentration C, the UV-Visible absorbance data can be defined as:

$$A_c^{UV-Vis} = -\,log\left(\frac{I_c}{I_{air}}\right) \quad \textbf{Eq. 8}$$

doi:10.6342/NTU201700804

And for the blank sample, we have:

$$A_{c=0}^{UV-Vis} = -\,log\left(\frac{I_c = 0}{I_{air}}\right) \quad \textbf{Eq. 9}$$

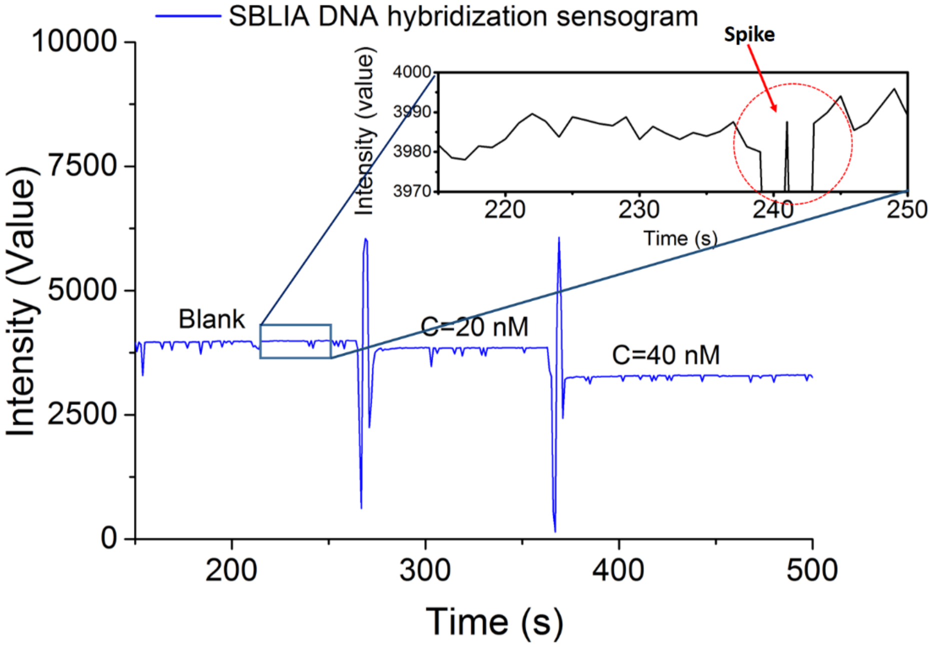

Fig. 12 typical DNA sensorgram of sLIA “smart” biosensor.

We can obtain absorbance, considering the blank sample as reference, simply by subtracting **Eq. 8** with**Eq.** ***9*** **Eq.** ***9***. In this way, we have:

$$A_c = -\,log\left(\frac{I_c}{I_{c=0}}\right) = A_c^{UV-Vis} - A_{c=0}^{UV-Vis} \quad \textbf{Eq. 10}$$

Using **Eq.** ***7*** and **Eq. 10,** results from both systems can be evaluated on the same basis.

doi:10.6342/NTU201700804

Chapter 5. Results and Discussion

Section 5-1. Characterizing audio channel

In the proposed SBLIA system, the audio output channel generates the modulation function to drive the laser as our source signal. Therefore, the quality of the audio output will largely determine the final performance of SBLIA. Meanwhile, the frequency working range of the audio channel also determines the upper frequency limit for our SBLIA. Therefore, audio channel has to be examined in some details. The **Fig. 13 (a)** and **(c)** shows typical audio jack output waveforms which are acquired via a data acquisition card from National Instrument (DAQ-USB X series). **Fig. 13 (b)** is recorded by directly connecting the audio phone output channel to the reading channel. In present context, the audio output is set to provide a sine voltage function to drive the laser diode, i.e.:

$$V_{audio\ out}(t) = V_{audio} sin(2\pi f t) \quad \textbf{Eq. 11}$$

where *f* is the designated digital LIA working frequency. As shown in **Fig. 13 (a)**, the audio phone jack can generate a V_{audio} between 2 to 240 mV, which is sufficient to modulate typical visible/NIR laser diodes. As can be expected, audio phone jack output exhibits noticeable random noises which spans a wide range of frequency (inset of **Fig. 13 (a))**. In addition to this white noise, we observe that a random fluctuation of the amplitude V_{audio} **(Fig. 13 (b))** exists. This “amplitude jittering” noises, is especially visible when V_{audio} is low. The noise is presumably coming from the audio output channel.

doi:10.6342/NTU201700804

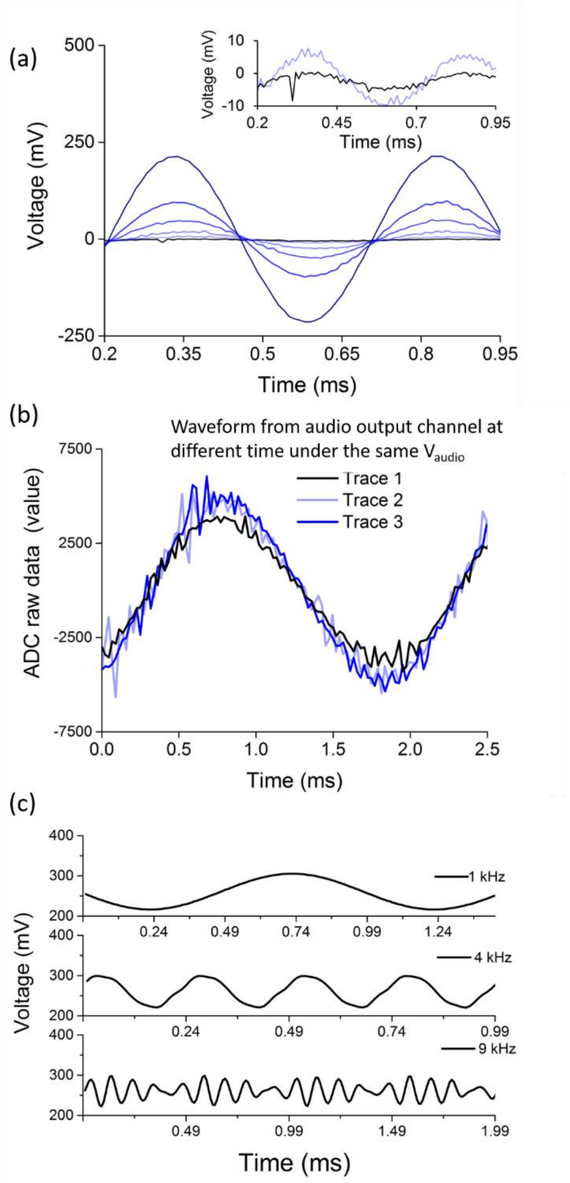

Fig. 13 Evaluating the audio output channel as SBLIA function generator (a) $V_{audio\ out}(t)$ signal from the audio output channel for different V_{audio}. The inset is a magnified view of the $V_{audio\ out}(t)$ waveforms under low V_{audio}. Based on the figure, it is clear that the audio channel noises are more prominent when V_{audio} is relatively small. (b) $V_{audio\ out}(t)$ recorded under the same V_{audio} at different time. (c) $V_{audio\ out}(t)$ with increasing working frequency (from top to bottom: 1 kHz, 4 kHz and 9 kHz respectively).

Judging on the acquired waveforms, a 19% discrepancy in amplitude (from trace 1 to trace 3) is found in extreme cases corresponding to the smallest V_{audio}. However, both noises mentioned above are much less prominent when the audio output level is higher. In brief, instead of assuming an ideal and noise-free driving function from audio output channel, we have a driving function in form of:

$$V_{audio\ output}(t) = (V_{audio} \pm \Delta V_{jittering}) sin(2\pi f t) + V_{random\ noise}$$ **Eq. 12**

doi:10.6342/NTU201700804

where size of V_{audio} and noises in the audio output channel need to be addressed carefully to provide optimized digital LIA performance.

Fig. 13 (c) shows the sinusoidal functions from audio output channel for an increasing modulation frequency. As can be seen, a slight waveform distortion commences near 4 kHz (cf. second trace) and keep increasing with frequency. The distortion in waveform is also accompanied by a gradual decay of the output amplitude (cf. trace at 9 kHz). To sum up, the audio output channel provides sinusoidal signals that are able to drive a laser diode up to about 4 kHz without severe distortion or power decay, and there exist certain noises that need to be addressed by proper filtering.

Section 5-2. SBLIA performance and working parameters

In biosensing, finding optimized working conditions to reduce noise level is of vital importance, as the noise determines the Limit of Detection (LOD), i.e. the minimum detectable amount of analyte with a statistical significance. Therefore, the effect of three SBLIA working parameters, the operation frequency (*f*), audio channel output voltage (V_{audio}) and integration time (τ) are thoroughly investigated in this section.

The inset of **Fig. 14 (a)** demonstrates how the noise level can be accessed from a typical SBLIA amplitude sensogram. In present context, the noise level is defined as the standard deviation of amplitude signal during a sufficient long period (>100 τ). Here, τ ranges from 0.4 ms to 200 ms depending on the given condition. To compare the noise under

doi:10.6342/NTU201700804

different working parameters, NSR is used instead of absolute noise level. The NSR is obtained by dividing the noise with the mean signal level and it is expressed in decibel.

To investigate the noise distribution in frequency space, a noise spectrum is shown in in **Fig. 14 (a)**. The spectrum is made by measuring NSR of SBLIA under different working frequencies.

As in most optoelectronic system, when working frequency increases, the noise intensity decreases rapidly following a power law. It is found that the noise is proportional to frequency in powers of -1.66. These data indicate that, by working above 1 kHz, the SBLIA reduces 85% of the 1/f flicker noise (from ~$8.8\text{x}10^{-3}$ to $1.32\text{x}10^{-2}$ NSR). As discussed in previous section, there exists noises in V_{audio} and the noise has a dependence on V_{audio}. Therefore, the effect of V_{audio} on SBLIA noise level is investigated here (**Fig. 14 (b)**). The result indicates as expected that the noise is reduced when V_{audio} increases. When V_{audio}>40 mV, the NSR reaches a plateau around -49 dB, indicating it is optimized. Based on the results from **Fig. 13 (a)** inset and **Fig. 14 (b)**, we can infer that the noise in audio channel is more or less fixed in size as compared to V_{audio}. Therefore, a large V_{audio} should be used to obtain a better NSR. Hence, $V_{audio}>$ 40 mV is suggested for a proper operation. The effect of τ is shown in **Fig. 14 (c).** We can see that, when τ increases from 0.4 ms to 200 ms, the NSR gradually reduces to a minimum around -63 dB. Based on the obtained results, τ> 60 ms is also suggested for

doi:10.6342/NTU201700804

a proper operation. Also, since this test is held under the lowest 1/f noise (at 2.5 kHz) and V_{audio} noise (V_{audio}=40 mV) possible, we consider -63 dB to be the optimum NSR achievable with our SBLIA at the moment.

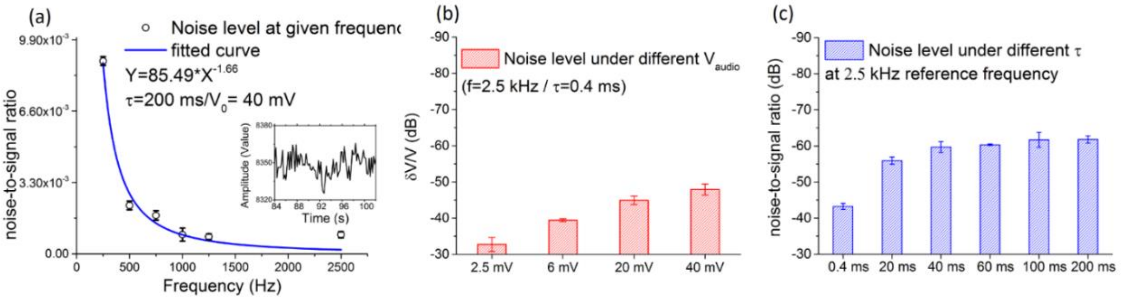

Fig. 14 Noise level and effect of working parameters on the developed SBLIA system. The evaluation of SBLIA performance and working parameter are carried out with the cuvette left empty without AuNP. (a) 1/f flicker noise spectrum. The evaluation is carried out under f=2.5 kHz and τ=200 ms. The inset presents a typical SBLIA sensogram that is used for statistical analysis of NSR. (b) noise measured under different level of output V_{audio}. The evaluation is carried out under f=2.5 kHz and τ=0.4 ms. (c) demonstrates the NSR under different level of τ. The measurement is made under f =2.5 kHz with 40 mV of output V_0 . The standard deviation of estimated noises are made from three independent tests.

Section 5-3. Comparison between SBLIA approach and SCB

Based on all the quantitative results and discussion above, **Table 1** provides a detailed comparison between the SBLIA and the conventional SCB. To begin with, both systems cost between 400~600 USD[21]. Almost all of the cost is attributed to the smartphone itself, since the system integration is relatively cheap (~15 USD). In terms of detection, SBLIA uses the 16 bits audio input jack to read the optical signal from a photodiode. This offers much higher data resolution. As already mentioned, the audio

doi:10.6342/NTU201700804

input channel can also capture data at 44.1 kSample/s, which make SBLIA a viable option on smartphone. Taking the advantage of high operation frequency, the SBLIA greatly reduces 1/f noise, audio channel intrinsic noise and environment noise.

Compared to the latest report on SCB based method[22], SBLIA offers a 15 dB lower noise level (-63 dB *vs* -48 dB). Finally, in settings of POCT where ambient lighting condition changes, SCB based method would need to fix auto-white balance (AWB)[8], carry out further calibration and add a fine enclosure to the system. However, these strategies often come with a price of lower resolution. On the contrary, SBLIA is not affected by normal ambient lighting condition and can largely filter out the lower frequency noises, making SBLIA a much better candidate in POCT setting

Table 1. Comparison of the proposed SBLIA method and the SCB method

Technology	System Cost	Resolution Data/time	NSR	Required hardware	Strategy to avoid ambient noise
SCB method	400 to 600 USD for smartphone[21] And ~15 USD for optical holder	8 to 12 bits 100 Hz	-48 dB[22]	1.optical source 2.Add-on camera	1.Fixing AWB 2.Calibration[18] 3.Fine enclosure
SBLIA method		16 bits 44.1 kHz	-63 dB	1.optical source, 2.photodetector 3.audio phone jack	Not affected

Section 5-4. DNA sensing by SBLIA-AuNP colorimetry

In this part, to demonstrate the SBLIA and its efficacy on AuNP colorimetry, our system is applied to short strand DNA detection with a target DNA concentration of 0,

doi:10.6342/NTU201700804

20, 40, 80 and 120 nM. The target DNA is 15-mer in length and is complementary to a 15-mer probe strand.

The probe ssDNA is always 200 nM for all samples regardless of the target complementary DNA concentration In this experiment, the SBLIA works under the optimized parameter, i.e. f=2.5 kHz, $\tau = 60$ ms and V_{audio}=40 mV. Finally, the SBLIA-AuNP colorimetry results are compared with a commercial UV-Visible spectrometer. UV-Visible spectrometer being generally considered as gold standard tool for colorimetry detection. The spectrometer was set to have an averaging time around 60 ms in order to compare both system on a fair basis. A typical UV-Visible spectrum for AuNP samples with different concentrations of target DNA is shown in **Fig. 15 (a)**. As revealed by the spectrum, the absorbance between 550 nm to 700 nm increases as target DNA concentration increases. This corresponds to a AuNP sample color change as shown in **Fig. 15 (b)** from red to dark purple, when target DNA concentration increases. As explained earlier, this is due to the fact that AuNP tends to aggregate in salt environment when dsDNA presents. This aggregation leads to change in the AuNP sizes which alters the localized surface plasmon resonance spectrum.

Fig. 15 (c) demonstrates a typical DNA SBLIA-AuNP colorimetry sensogram. Judging on the sensogram, SBLIA system shows the similar monotonic change as in UV-Visible spectrometer, the modulation amplitude of the beam drop by 33% from 0 nM to 120 nM

doi:10.6342/NTU201700804

of target DNA. This is again due to the increasing absorbance of the AuNP sample along with increasing dsDNA concentration. In order to further compare the results from SBLIA-AuNP sensogram and UV-Visible spectrometer, the above mentioned detection is repeated four times for both systems and calibration curves are then established. The data from our SBLIA system is converted into the absorption unit (AU) for constructing the calibration curve. The noise is measured in each set of test and presented as averaged results. The calibration curve can be found in **Fig. 15 (d)**. For both systems, the absorbance at 650 nm (A_{650}) has a very similar linear dependence to the concentration (C, in unit of nano-molar) of target DNA. As indicated from the curve, the calibration curve is $A_{650}=1.44x10^{-3}C$ for the SBLIA and $A_{650}=1.1x10^{-3}C$ for the UV-Visible system. Since both systems use a cuvette with the same optical path length, this result is reasonable judging from the Beer-Lambert's law. Further investigation of the systematic noise indicates that the noise form the SBLIA system is 4.3 times smaller than the UV-Visible spectrometer, i.e. 3.7×10^{-4} AU compared to 1.6×10^{-3} AU.

Finally, based on the obtained noise and the calibration curves, the LOD is then calculated to be 0.77 nM for our system which is 5.7 times lower than 4.36 nM achieved by the UV-Visible system.

The importance of the obtained results, beyond the figure of improvement, lies in the insights that they provide into the context and future development of smartphone based

doi:10.6342/NTU201700804

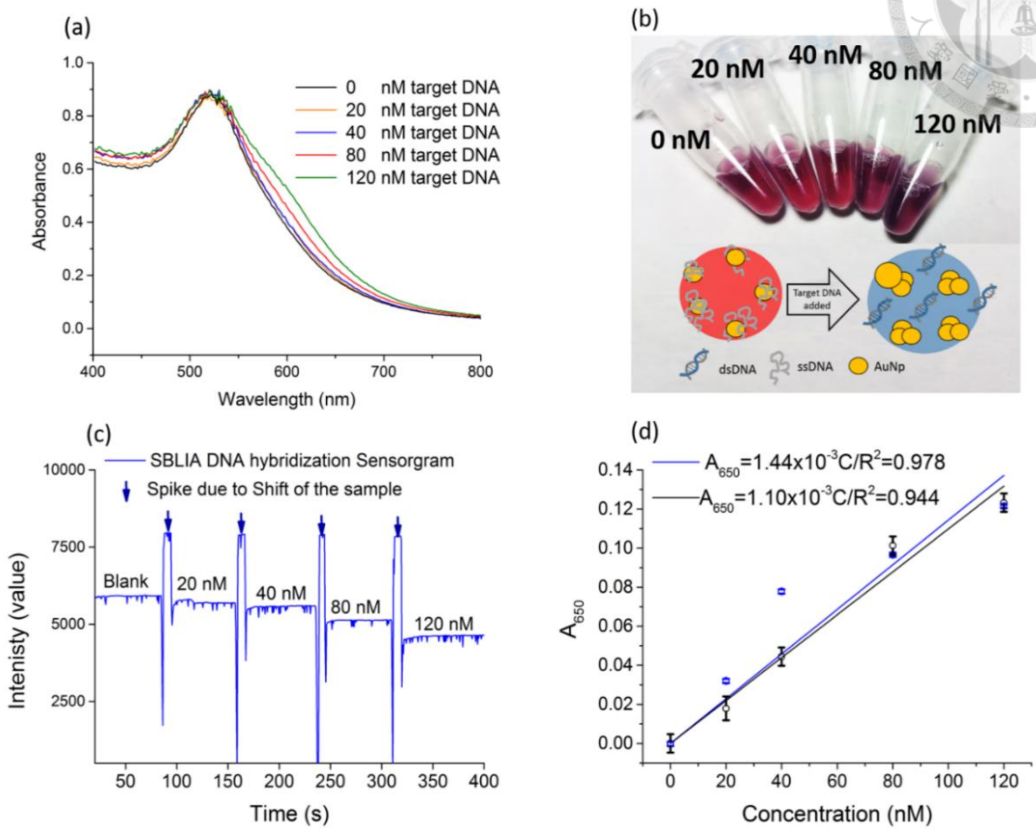

Fig. 15 SBLIA-AuNP colorimetry DNA sensing
(a) UV-Visible spectrum of the AuNP sample solution. The sample solution contains 200 nM of ssDNA with different concentration of target DNA. (b) An image of the sample solutions and a scheme of the AuNP DNA sensing mechanism. (c) SBLIA-AuNP colorimetry DNA sensing amplitude sensogram. The concentration of target DNA is marked and the blue spike in the figure indicate the spike due to change of sample. (d) Calibration curve for the SBLIA-AuNP colorimetry system (blue trace) and UV-Visible spectrometer (black trace).

diagnostic. Firstly and most importantly, the SBLIA proposed herein has high potential for development of further optical based sensor technologies. Although not explicitly used herein, the phase detection noise of our SBLIA system is down to 0.2 degree which could lead to high quality smartphone based phase sensitive detection (**Fig. 16**). For

doi:10.6342/NTU201700804

example, through proper optical design, SBLIA could be applied to build smartphone based LIA enhanced fluorescence tag bio-sensor[23], phase sensitive detection of plasmonic sensor [24] and even holographic measurement (multi-channel phase detection). Hence,

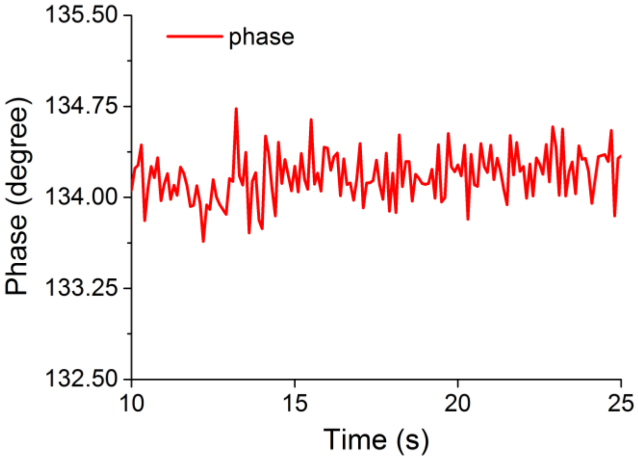

Fig. 16 phase signal extracted with SBLIA.

while smart AuNP colorimetry is undoubtedly an interesting approach to pursue, we believe that the SBLIA itself should spur a wide range of distinct applications in sensing.

Secondly, we note that the ratiometric measurement using a 650 nm/520 nm absorbance ratio is not used here as in our previous report since audio channel provide only one input[25]. As is well known, using 520 nm absorbance to normalized 650 nm absorbance may further enhance the batch-to-batch reproducibility of AuNP colorimetry. In the future, this may be addressed by incorporating new electronic design[6] or by extending SBLIA onto an external embedded system where multiple analog receivers are available. The latter design could add flexibility to SBLIA data resolution, by adding a

doi:10.6342/NTU201700804

number of detection channels. Such approach would also be well adapted to smartphone models where audio jack is absent.

Finally, the ultimate performances of smartphone based diagnostic is still an on-going debate[8] and important design factors need to be considered for applying SBLIA-AuNP system in on-site disease screening. These factors include complex background of physiological sample[26] and the consequent pre-processing issue[27]. Still, some research results report smart diagnostic devices have already reached world health organization (WHO) gold standards[3] or other gold standards[9], and have been applied to on-site application or disease screening[4]. As exemplified by this work, we are expecting more and more smartphone based diagnostic tools with equal or even better performances as compared to some of their laboratory relatives.

Section 5-5. Conclusion

In summary, a SBLIA-AuNP colorimetry sensor is proposed. The SBLIA system employs audio output channel as function generator while audio input channel is employed as photo-detector reader. It is found that SBLIA system can largely reduce the audio output channel intrinsic noise as well as the environmental noises to reach a minimum NSR of -63 dB. This NSR was obtained after optimization of the working parameters of the system (f=2.5 kHz, V_{audio}=40 mV and τ =60 ms). Judging on the results, SBLIA offers better NSR compared to SCB method (-63 dB vs -49 dB). At the

doi:10.6342/NTU201700804

same time, SBLIA provides better data bit resolution while being insensitive to changes in the ambient lighting condition. Finally, SBLIA-AuNP colorimetry was applied to a DNA detection experiment for sensitivity evaluation of the efficacy. Compared to the UV-Visible spectrometer, SBLIA has a LOD around 0.77 nM which is 5.7 times lower than the result form a desktop UV-Visible spectrometer. The main reason behind the improvement is attributed to the excellent NSR offered by SBLIA system. Finally, SBLIA may very likely foster further diagnostic tool, e.g. fluorescence and interferometry, leading to more sensitive “smart” diagnostic for POC applications.

doi:10.6342/NTU201700804

Part 2. "Shearing Interferometer based Surface Plasmon Resonance Biosensor (SiSPR)"

doi:10.6342/NTU201700804

Chapter 6. Introduction on SiSPR

Surface Plasmon Resonance (SPR) biosensor has been widely applied in bio-sensing for diagnostic purposes due to the real-time/label-free detection capacity as well as for its high sensitivity[28, 29]. The most common and widely used SPR optical set-up is the "Kretschmann configuration" as shown in **Fig.** ***17***. In such optical configuration, an optical beam source illuminates a metal layer through a prism coupler in order to reach the plasmonic resonance angle. At this resonance angle, a large portion of the beam is absorbed; therefore, the intensity of the reflected beam is attenuated to a large extent. When a target bio-marker is captured by the probe molecule on the surface of the plasmonic layer, the refractive index in the vicinity of the surface is affected resulting in a shift of the resonance angle. The photo-detector, which is fixed at the resonance angle, then records an increase in optical intensity. In this way, the bio-chemical reaction information is transformed into optical intensity data.

Kretschmann configuration SPR, or so-called amplitude based SPR, has numerous advantages. First, it can study real-time biochemical kinetics without the need of molecular tagging (e.g, fluorescence). Secondly, it is mechanically robust and simple. Only few relevant optical components are needed to build the system. However, Kretschmann configuration SPR has also its shortcomings. It is known that amplitude based SPR has relatively lower sensitivity as compared to a phase-sensitive SPR counter

doi:10.6342/NTU201700804

parts[24, 30]. Based on empirical evidences and theoretical derivation, many reviews suggest that the minimal refractive index resolution (Δn_{min}) of amplitude based SPR is around 10^{-5} Refractive Index Unit (RIU)[31]. Reports also suggest that the SPR limitation comes from intrinsic noise level.

As a result, amplitude based SPR is expected to experience sensitivity issue in low concentration sample (pM to fM range) or low purity sample. Even with proper blocking agent, non-specific bindings during detection may reduce sensitivity over 100 times. Therefore, improving SPR sensitivity is a real challenge for on-site application but also for clinical and laboratory use.

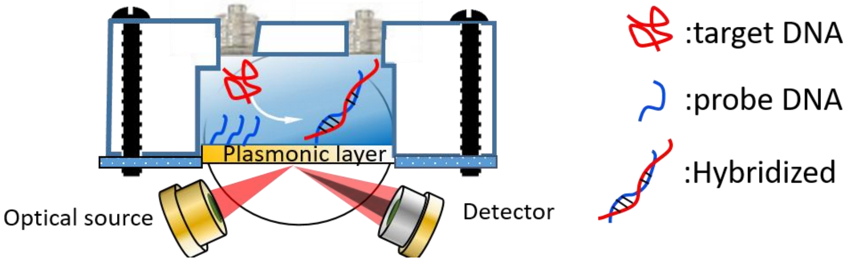

Fig. 17 SPR optical set-up based on Kretschmann Configuration.

Many past literature indicate that phase interrogation SPR can be considered as potential candidate[32-34] to address such sensitivity issue. Considering the phase change over refractive index $(\Delta\phi/\Delta n)$ and the obtained Δn_{min}, the phase interrogation SPR has been claimed to be 100 times more sensitive as compared to its amplitude counterparts. To be more specific, the phase interrogation SPR has been reported to reach Δn_{min} of 10^{-8} RIU. Nevertheless, phase interrogation SPR also suffer from its own shortcomings.

doi:10.6342/NTU201700804

It requires multiple optoelectronic components such as beam splitters, and usually a frequency or phase modulator using a piezo-actuator, an Acousto-Optical Modulator (AOM), a Photo-elastic Modulator (PEM) or a wavelength tunable optical source. These instruments increase complexity, weight and price of the device. Besides drawbacks mentioned above, phase interrogation makes the instrument highly vulnerable to mechanical vibrations. These setbacks have not just limited the on-site application of phase sensitive SPR. In the SPR market, which has Biacore^{TM}, Bio-suplar^{TM}, Sensia^{TM}, GWC^{TM} as major players, there are nearly no commercially available phase sensitive SPR. In other words, the above-mentioned limitation has entirely prevented the commercialization phase interrogation SPR.

Based on the discussion above, we consider that it is desirable to have a new optical scheme that offers the simplicity of Kretschmann configuration while providing a phase interrogation measurement. Most importantly, a monolithic design should be used to strongly minimize the effect of mechanical vibration. In this way, we can have a SPR set-up that is mechanically suitable for point-of-care application and has enough sensitivity to address the low pre-processing level of the sample.

To fulfill such purposes, we introduce a new type of SPR optical set-up, which we will refer to as “Shearing Interferometry based Surface Plasmon Resonance Biosensor (SiSPR biosensor)”. The SiSPR is realized by three key components. The first key component is

doi:10.6342/NTU201700804

the plasmonic chip combining the traditional metal layer and a monolithic interferometer. The second key factor is the use of a low cost spatially and spectrally single-mode laser diode which has a modest wavelength tunability of about 0.079% of its nominal wavelength. The last key component is a newly devised phase retrieval method.

The SiSPR chip and a brief overview of the system can be seen in ***Fig*. 18**. The chip is composed of a glass slide sandwiched by a plasmonic layer and a reflective layer. The extra-reflective layer, lead to division and recombination of the beam wavefront. As a result, a shearing interferometer is integrated within a plasmonic chip.

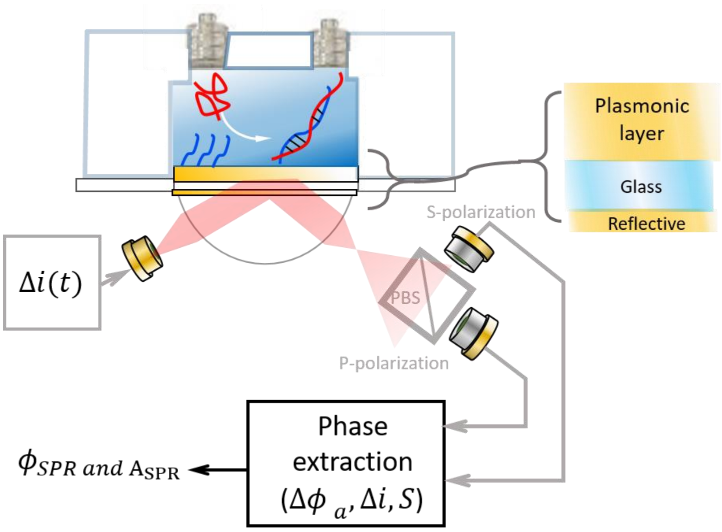

***Fig*. 18** An overview of SiSPR optical set-up.

The monolithic SiSPR chip provides the merit of being less vulnerable to mechanical vibration than other conventional homodyne interferometers. To extract the phase, a sinusoidal modulation of the laser wavelength is used to induce Sinusoidal Phase Modulation (SPM). Although not trivial, several options exist to recover the phase information in presence of a sinusoidal phase modulation. However, the SPM induced by a current modulation makes the phase extraction especially delicate, since a non-negligible amplitude modulation is also induced by this current modulation, exactly at the same frequency.

To solve this problem, we devised a new phase extraction method for SiSPR, where the amplitude of the current modulation "$\Delta \mathrm{i}(\mathrm{t})$", the phase modulation depth "$\Delta\phi_a$", and the wavelength-to-current sensitivity factor “S” are the major parameter to consider for extracting the SiSPR phase “ϕ_{SiSPR}". The merits of SiSPR are listed in **Table 2** in order to illustrate the points discussed above. In the next chapter (chapter 7), a literature review is provided. This review focus mainly on the limitations of homodyne interferometry (including few related patents), the Δn_{min} reported for SPR in past literature and, finally.

Table 2 Comparison of SiSPR with conventional amplitude or phase sensitive SPR

	Amplitude based SPR	**Phase sensitive SPR**	**SiSPR**
1.Sensitivity (RIU)	Moderate (10^{-5})	High (10^{-7})	High (10^{-7})
2.Mechanical noise	Not affected	Affected	Not affected
3.Cost	low	High	Moderate
4.Phase detection	No	Yes	Yes
5.Compatibility with Kretschmann configuration	Yes	No	Yes

The notion of "sensitivity" and the method of estimating Δn_{min} remain topics of debate among different SPR reports. Through selected references, we will detail how these quantities are defined and discuss the possible issues related to the definition. In chapter 8, we detail the SiSPR technology. Starting with the basic working principle of SiSPR, we first provide a wave optics description of the SiSPR. Then, we discuss the angle dependence of the optical path difference in this system and we then describe the fabrication process of the plasmonic chip. At the end of chapter 8, the proposed phase extraction method is derived and analyzed. In order to keep concise the thesis, the main focus in this chapter is to introduce the work flow as well as five related phase extraction parameters. A more detailed derivation is placed in appendix. In chapter 9, the results of SiSPR experiments are finally revealed. Optical images of the SiSPR interferences are provided to validate the above-mentioned working principle. The measurement of "S" and corresponding "$\Delta\phi_a$" are demonstrated. To evaluate the system sensitivity in terms of $\Delta\phi/\Delta\mathrm{n}$ and Δn_{min}, a sensing experiment on a series of glucose reference solution is demonstrated. We then compare $\Delta\mathrm{I}/\Delta\mathrm{n}$ (sensitivity of detection from amplitude information) with $\Delta\phi/\Delta\mathrm{n}$ (sensitivity of detection from phase information) and estimate the ultimate sensitivity advantage of SiSPR. In the final part of the thesis, we perform a surface modification with a 40 mer "tro4" aptameric probe and carried out preliminary protein sensing. The most technical

doi:10.6342/NTU201700804

part for potable prototype integration is demonstrated in appendix.

doi:10.6342/NTU201700804

Chapter 7. Literature Review on phase interrogated SPR

Phase-sensitive SPR set-up is generally divided into several categories, such as: homodyne detection, white-light interferometry, heterodyne detection and polarimetry. The different approaches, are described hereafter with the associated issues and references.

Homodyne interferometry

In essence, most common homodyne interferometric SPR still follow either a Mach Zehnder[35] **(Fig. 19 (a))** or a Michelson (**Fig. 19 (b)**) interferometer configuration. In the above mentioned methods, a single optical source beam is split into the “signal beam” and the “reference beam” by use of a beam splitter. The two beams are then traveling through different optical paths, before being recombined through the same or another beam splitter, to generate fringes characteristic of two-beam interferometry. When the optical frequencies of the two beams are the same, the interferometry is said to be ‘homodyne’ and the fringes are static in time (heterodyne interferometry described hereafter produces a temporal beating). When the two beams are parallel, no spatially variable phase difference exist and the fringes reduces to an homogenous spot, more less bright depending if the beams are in phase or out of phase.

In this convenient configuration, a piezo-actuator driven mirror is usually applied for phase modulation purposes to determine both amplitude and phase information from

doi:10.6342/NTU201700804

the resulting beating.

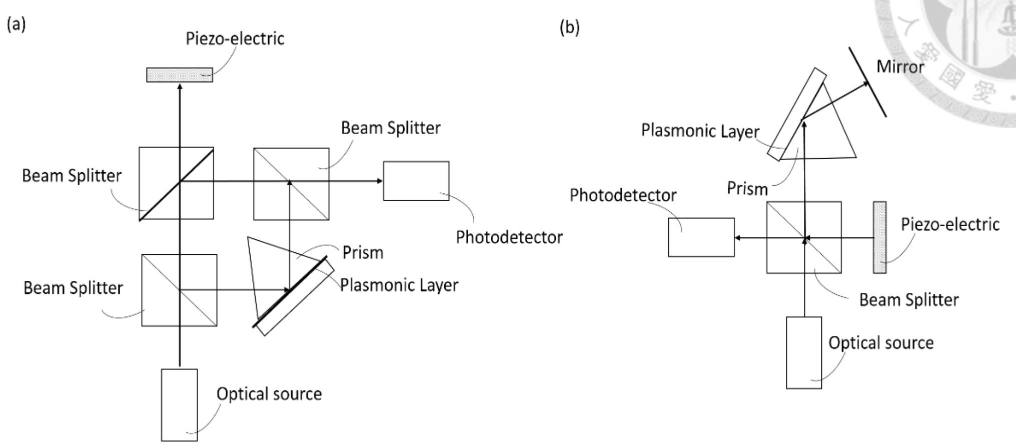

Fig. 19 Homodyne interferometers: (a) Mach Zehnder and (b) Michelson.

White light interferometry

The need for a phase modulator described above can be avoided using white light interferometry, which can be considered as a more ‘static configuration’ in the sense that no time dependent measurement is required to obtain an unambiguous phase information. For example, Siu-Pang Ng et. al. have demonstrated a differential spectral phase sensitive SPR through Michelson interferometer design as can be seen from ***Fig. 20***[36]. By use of a white light source, they are able to carry out phase interrogation over a range of wavelength as shown in ***Fig. 20***.(a). In this case, the phase information is retrieved via a spectral analysis. Due to a slight path unbalance between the two arms, a ‘grooved’ spectrum is obtained, similar to what can be observed in a Fabry-Perot interferometer where the light interferes constructively and destructively depending on the wavelength. The spectral pitch between peaks and valleys change if a phase shift is present, providing

doi:10.6342/NTU201700804

phase information. In the proposed work, the phase stability is improved by making two simultaneous measurements, one for the S-polarized wave and another for the P-polarized wave. The phase of the S-polarized wave is then used as reference phase signal, it does not experience SPR.

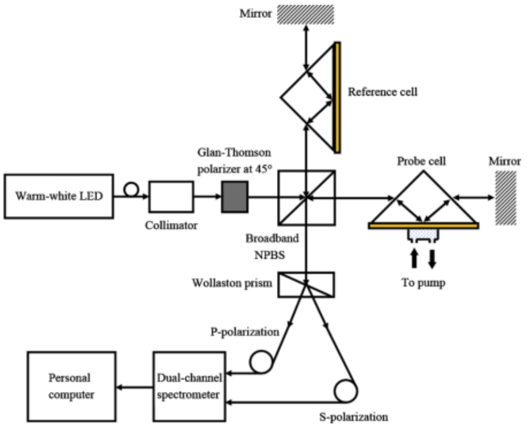

Fig. 20. Differential spectral phase sensitive SPR from Siu-Pang Ng et. al.
A Wollaston prism is used to separate the two polarization components and perform the differential analysis.

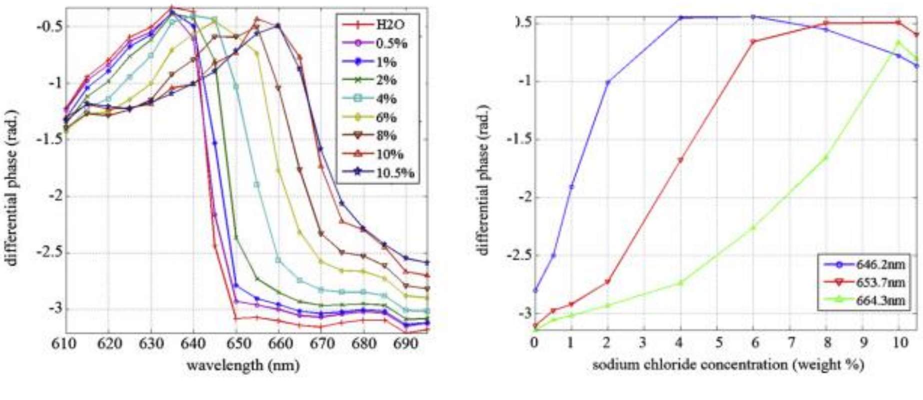

Fig. 21. Phase interrogation result on sodium chloride solution from Siu-Pang Ng et. al.

Vibrational Noise issue and differential measurement

As can be seen in ***Fig. 20***, and the standard interferometers described before, it takes two mirrors and one beam splitter to fulfill the basic interference requirement. These separate optical components experience unsynchronized vibrational displacements at specific frequencies, depending on their weight, shape and fixation as well as the mechanical/acoustical noises in the surrounding. As a result, phase noises are presents due to these optical path fluctuations. The use of a differential measurement (S and P) is a good approach to strongly reduce the impact of such mechanical noises, as we can expect that a “P-S” phasogram would eradicate all the common noise but the SPR phase signal. However, monolithic configurations where the optical elements are not separated but fixed together should be preferred to reduce further the noise.

Estimation of sensitivity

We use now continue to use Siu-Ping Ng’s work to demonstrate how sensitivity can be estimated in phase sensitive SPR. By shifting between solutions with different Sodium chloride concentration (from 0.5% to 10.5%), the author was able to obtain the phase response over a given refractive index. Based on the results, when the 0.5% NaCl solution turns into a 1% NaCl solution (which correspond to refractive index change of $8\mathrm{x}10^{-4}$ RIU), a 0.632 rad phase change is obtained (at a wavelength λ= 646.5 nm). Then, it is estimated that, with a noise level of $2\mathrm{x}10^{-4}$ rad, the sensitivity of the sensor is: $\Delta\mathrm{n}_{\mathrm{min}} = \frac{8\times10^{-4}}{0.632}\frac{\mathrm{RIU}}{\mathrm{rad}} \times 2 \times 10^{-4}\ \mathrm{rad} \sim 2.57 \times 10^{-7}$ RIU.

At this point, we should define “sensitivity” in the SPR context. As a matter of fact, the term sensitivity is not always very clear, in the sense different authors can use different

doi:10.6342/NTU201700804

evaluations. In context of SPR, two different but closely related concepts should be precisely defined.

In one sense, “sensitivity” corresponds to the slope of $I(n)$ corresponding to a change in the signal *amplitude* I for a given refractive index change (near the reflection dip), or , when placed in context of phase sensitivity detection, the slope of $\phi(n)$ given by the *phase* jump at the resonance angle. That is to say “sensitivity” can be defined as either in $\Delta I/\Delta n$ in case of amplitude based SPR or as $\Delta\phi/\Delta n$. This “sensitivity” reveals the intrinsic capacity of the plasmonic layer to respond to refractive index change. As can be seen from **Fig. 22**, at a given plasmonic layer thickness, SPR have a steeper “phase jump” across the resonance point. That is to say, phase sensitive SPR can largely increase its sensitivity by tuning the film thickness. On contrary, the slope of two wings of the resonance dip has similar slope between 44-50 nm of plasmonic later. From this perspective, it is reasonable to assume that the phase could give a much greater sensor response for small Δn. This is very often the first argument that suggesting $\Delta\phi/\Delta n$ is more “sensitive” than $\Delta I/\Delta n$, which has been supported empirically from results of Kabashin and Nitkin[37].

However, ΔI and $\Delta\phi$ are not in the same dimension, therefore direct comparison is not possible. In order to compare the performance of two difference system, the noise of the measurement system has to be considered and thereby yielding the minimum

doi:10.6342/NTU201700804

resolvable signal. In this way, the sensitivity can be compared in terms of refractive index. In case of the bio-sensing processes, where sensor is in real space that has temperature variation and electronics noises, the actual noise density plays a major role in determining the "sensitivity". Therefore, certain reviews report the sensitivity in terms of minimum resolvable refractive index (Δn_{min}). To be more precise, the "sensitivity" mentioned in the latter context is the limit-of-detection (LOD). Therefore, for conciseness of discussion, we will refer to this as minimum resolvable refractive index (Δn_{min}) or LOD throughout the thesis.

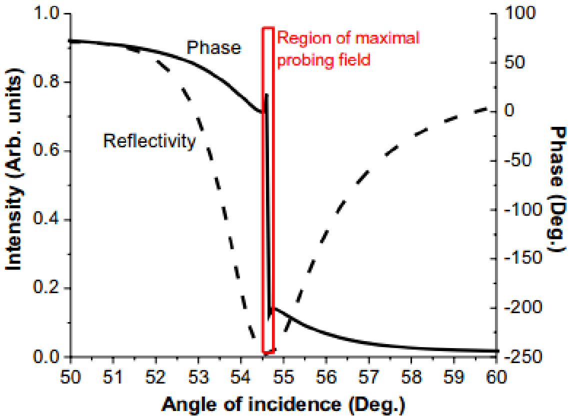

Fig. 22 SPR resonance dip and corresponding phase jump.

In evaluating the Δn_{min} of any SPR system, there are also few other points that are worth noticing. First, considering the difference in the physical quantities measured (ΔI and $\Delta \phi$), Δn_{min} seems to offers a fair ground for comparison of performance between platforms. However, since noise is the key factor in determination of Δn_{min}, there is a certain level of ambiguity as to how this value is calculated. Typically, Δn_{min} is an estimated value based on extrapolation of a SPR phase response on a given sample (e.g.,

doi:10.6342/NTU201700804

alcohol, glucose or NaCl solution). By considering both the noise over a given period of time and slope of phase response ($\Delta\phi/\Delta n$), Δn_{min} is then estimated as shown in the work from Siu-Pang Ng et. al.[36]. These measurements are made with refractive index changes much larger than the real Δn_{min} in order to exclude the influence of baseline drifting and other noise issues. In other words, a large Δn_{sample} is applied to induce large $\Delta\phi$, the result is then used to estimate Δn_{min} with the estimated noise. The $\Delta n_{sample}/\Delta n_{min}$ is typically on order of 10^2 ~10^5.

With this type of "extrapolation", Δn_{min} is strongly affected by data sampling and processing method. For example, one literature review on Texa's Spreeta (a discontinued amplitude based portable SPR sensor product) applied a large amount of signal processing to address noise issue including baseline drifting correction and intense averaging. In result, the author reported an intriguing LOD around 10^{-9} RIU, much better than standard commercial SPR system and even better than phase sensitive SPR.[38]

The comparison of SPR performance across different platform is not, however, the main focus of the present study, since our major aim is to present a new type of SPR that offers cost, design and performance advantages. The discussion herein serves mainly to clearly define the term used in the thesis.

Heterodyne

Another way to interrogate the optical beam phase information is to use a heterodyne

doi:10.6342/NTU201700804

method. An example of heterodyne interferometer[34] can be found in **Fig. 23 (a)** and **(b).** In this **Fig. 23 (a)**, the signal and reference beams are frequency shifted by acousto-optical modulators (AOMs), generating a 40 MHz-shifted beam and a 40.06 MHz-shifted beam. When the two beams are multiplexed by a beam splitter, a low frequency beating occurs at the frequency difference (i.e. 60 kHz) as shown in (cf. **Fig. 23 (b)**). Then, any change in the signal phase induces a phase lag or a phase advance in the observed beating. In this way, the phase information can be extracted by measuring the phase of the beating signal. This is practically achieved by using a standard Lock-in amplifier working at the beating frequency.

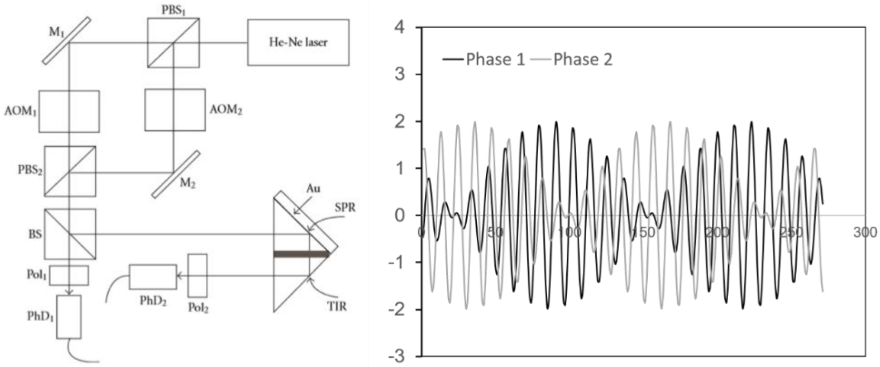

Fig. 23 Heterodyne detector (a) optical set-up (b) corresponding interferogram.

Noise and cost issue in Heterodyne method

In this Mach Zehnder based heterodyne detection, three beam splitters, two mirrors and two AOMs are used. This large amount of optics requires a rather mechanically stable environment. Without advanced method for vibrational noise exclusion, this design would not be a viable option for portable application. Also, the use of AOM greatly

doi:10.6342/NTU201700804

increases the cost of device.

Polarimetry

Alternatively, we can also retrieve SPR phase information by polarimetry[33] as shown in ***Fig. 24***. This approach takes advantage of the fact that the S polarized part of the beam is reflected on the probed interface without a noticeable change in its phase. On the contrary the P polarized part elicits a surface mode and is subject to a noticeable phase change when the interface environment is changed, producing a change in the reflected beam polarization. To exploit this property for phase extraction, a photo-elastic modulator (PEM) is used to modulate the polarization of the reflected beam. In this way, the detector would receive S and P that are sinusoidally modulated in time. As results, this measured polarization ellipticity can be used for extracting phase information.

Noise filtration advantage in Polarimetry

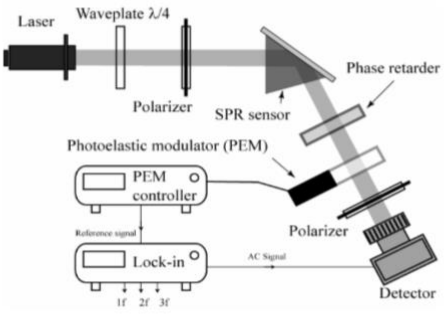

Fig. 24 Polarimetry interferometer.

This common path approach is interesting in term of noise, as contrast to first two method where mechanical noise affect the device noticeably. In polarimetry method, mechanical

doi:10.6342/NTU201700804

noises mostly impacts both polarization in the same way resulting in an overall noise reduction since S serves as a reference. However, the use of PEM is again a issue in size of device as well as in cost.

Compact and monolithic design

As discussed above, vibrational noise issue remains to be one of the major challenge for phase sensitive SPR device. One possibility to solve the drawback of interferometric phase sensitive SPR sensor is to use a monolithic interferometer. As taught by US. Pat. No. 0218738A1 (cf. **Fig. 25**), a monolithic phase sensitive chip can be made through the use of micro-nano fabrication. Through photolithography and evaporation process, this type of monolithic chip gathers the required optical components on a single chip by performing integrated wave-front division and recombination. Typically, two areas with different film thickness are designed. Consequently, an optical path different of about half a wavelength is generated, leading to clear interference effect when the beam is recombined. Since all component are in one piece, this kind of design is largely vibrational noise free.

Still, challenges remains. With nanostructured monolithic chip, a wavelength tunable source is required consider the optical path length difference. Also, the photolithography and multiple evaporation process would greatly increase the cost of the chip.

Most importantly, because the device is made of one chip, the sensor receives almost

doi:10.6342/NTU201700804

no vibrational noise. We have proposed herein an alternative way of making a monolithic phase sensitive chip which is now under the WIPO PCT patterning process through a law firm.

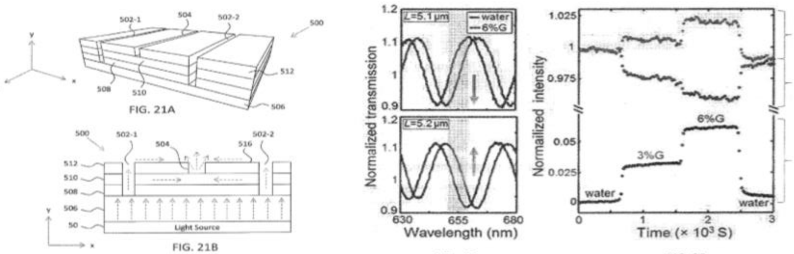

FIG. 21A FIG. 21B FIG. 19 FIG. 20

Fig. 25 Monolithic phase sensitive sensor chip from US. Pat. No. 0218738A1.

Remark on the literature review

Through the above literature review, we aimed to point out the possible strategies that could be used for making handheld phase sensitive SPR. The challenge is mainly to find a cost effective phase interrogation mechanism, to avoid vibration noises that are omnipresent in a common environment and to avoid the use of a large amount of optical component. As discussed in the introduction, these issues impede the potential of phase sensitive SPR for further application. The chapter 8 hereafter details the solution we propose to address these issues.

doi:10.6342/NTU201700804

Chapter 8. Methodology

Section 8-1. Working principle of SiSPR

In this first section on the methodology, the fundamental working principle of SiSPR is introduced. **Fig. 26** shows an optical beam emitted from a laser diode impinging on the SiSPR set-up. As can be seen from **Fig. 26**, a hemi-spherical lens is used as a coupling prism instead of a trapezoid lens or the most commonly used hemi-cylindrical lens. By placing the laser diode at the focal point of the hemi-spherical lens, the diverging beam emitted from the diode is collimated upon entering the coupling prism. In this way, the hemi-spherical lens is acting as both collimator and prism coupler, eliminating the need for an extra optic. Except a reduced number of the optical parts needed, the hemi-spherical lens also has other merits. For example, it provides almost full working range of incident angle. In our final prototype, it can work with an incident angle ranging from 0 degree to around 75 degree, which is much larger compared to trapezoidal lens coupler. From now, we will refer the beam portion in **Fig. 26** as “beam 1”. To be more precise, beam 1 starts from the laser emitting point and ends right at the reflection on the first flat interface. Part of beam 1 undergoes a Fresnel reflection and generate corresponding beam 2 (cf. **Fig. 27 (a))**. Since Beam 2 is not affected by SPR effect, it is regarded as reference beam in SiSPR. Again, due to the use of hemi-spherical prism coupler, beam 2 will focus on the focal

doi:10.6342/NTU201700804

point after exiting the prism (cf. **Fig. 27 (a)**). Note that the beam center is marked by a black dashed line. Asides from reflection, part of the beam 1 is transmitted and will generate our signal beam (beam 3) as shown in **Fig. 27 (b)**. Beam 3 interacts with the SPR layer, and carries on the molecular binding event information. Finally, beam 3 will is reflected by the plasmonic layer forming our final signal beam (beam 4) (cf. **Fig.27**). Note how the beam center of the beam 4 has been laterally shifted, as compared to the beam center of the beam2. This lateral shift is associated with a difference in optical path

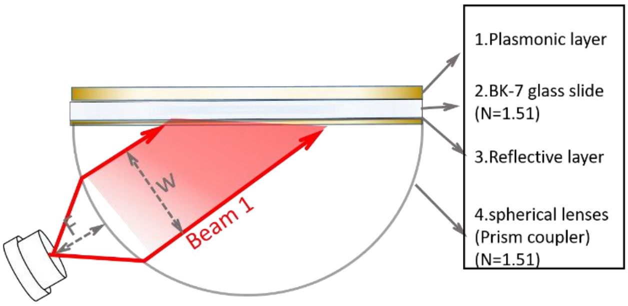

Fig. 26 Major optical component and beam 1 of SiSPR comprising a bi-reflective layer (metal coating on each side).

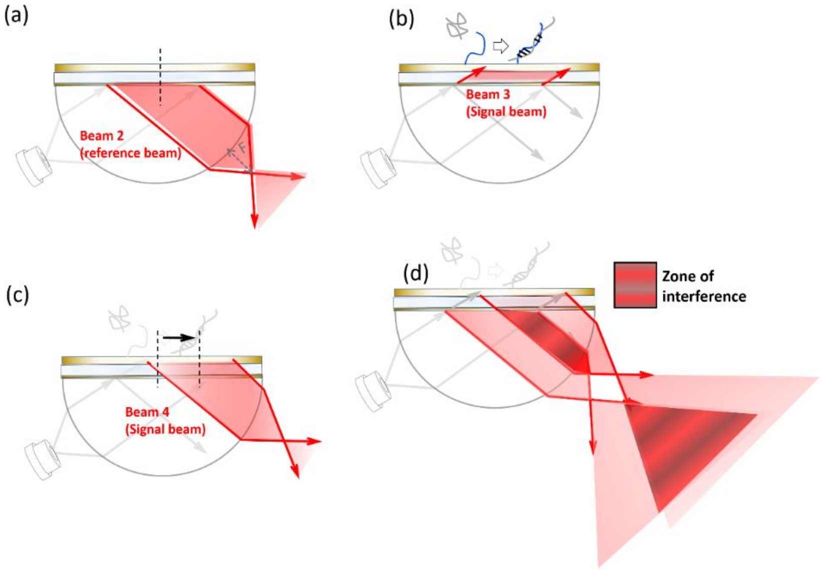

Fig. 27 Different beam portions within the SiSPR.

traveled by the beam 4 and beam 2. Due to this very reason, this type of interferometer can be regarded as a “shearing interferometer”[39]. As can be seem in **Fig. 27 (d)**, beam 4 and beam 2 overlap and finally lead to interferences effect. We note that there are three factors that determine the width of the overlapping zone: beam width (w), thickness of the glass slide and incident angle.

Section 8-2. Wavefront analysis on SiSPR

In this section, we perform an analysis of the optical paths travelled by the beam wavefronts, which are angle-dependent. As will be detailed, Optical Path Difference (OPD) is an important variable in SiSPR phase extraction process because our phase modulation will be directly proportional the OPD.

The path differences between the signal beam and reference beam in SiSPR are better understood by considering ***Fig. 28*** **(a)** and **(b)**. As shown in ***Fig. 28*** **(a)**, the leftmost portion of the beam is noted “sub-beam 1”, and the rightmost one is noted “sub-beam 2”. In this representation, the wavefronts are perpendicular to the propagation axis,

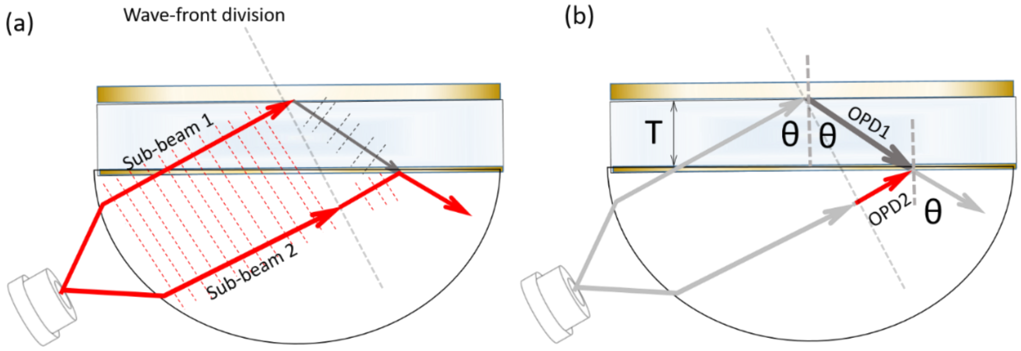

Fig. 28 Wave-front division and OPD calculation in SiSPR.

doi:10.6342/NTU201700804

and sub-beam 1 and sub-beam 2 have no wave-front difference until the division point indicated by the black dashed-line. After the wavefront division point, the plasmonic layer reflects sub-beam 1, thereby creating a wave-front direction change. Then the wavefront division ends as the two sub beams are merged again upon the reflection of sub-beam 2. Since we know the start and the end of the wavefront division, we can now calculate the optical path difference.

The OPD1 shown in the figure can be defined as:

$$OPD1 = n_{BK-7} \times \frac{T}{cos(\theta)} \quad \textbf{Eq. 13}$$

Where T is the glass slide thickness, and OPD2 is defined as:

$$OPD2 = n_{BK-7} \times \frac{T}{cos\theta} \times cos(\boldsymbol{\pi} - 2\theta) = n_{BK-7} \times \frac{T}{cos(\theta)} \times cos(\boldsymbol{\pi} - 2\theta) \quad \textbf{Eq. 14}$$

As result, the OPD in our system is:

$$OPD = OPD1 - OPD2 = n_{BK-7} \frac{T}{cos(\theta)} (1 + cos\, 2\theta) \quad \textbf{Eq. 15}$$

Since $1 + \cos 2\theta = 2cos^2\theta$, we then have:

$$OPD = 2n_{BK-7} T\, cos\, \theta \quad \textbf{Eq. 16}$$

We can therefore obtain the angle dependence of the OPD as shown in ***Fig. 29,*** as marked by blue line. The OPD decreases with increasing incident angle, following a cosinusoidal form. As demonstrated in the inset, for the typical Kretschmann angle which is around 65~68 degree of incidence (under water), the OPD is between 1.26~ 1.12 mm.

doi:10.6342/NTU201700804

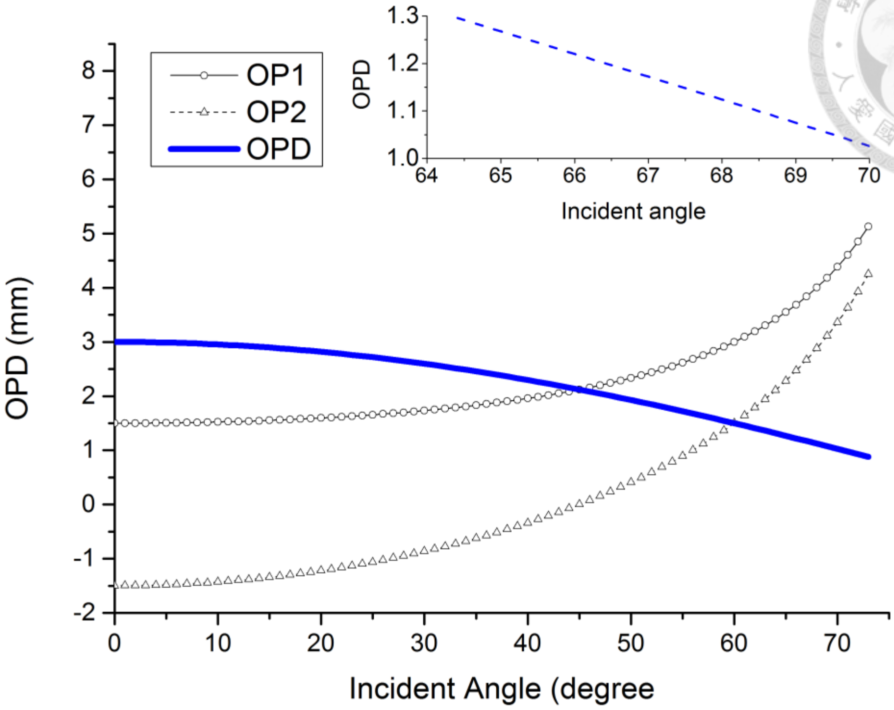

Fig. 29 Angle dependence of OPD in SiSPR.
The blue line indicates the OPD while the black line with circle symbol indicates OPD1 and the triangle symbol mark the OPD2. The inset provides OPD-incident angle dependence between 64-70 degree of incidence.

Another case: the glass slide based shearing interferometer

As shown in **Fig. 30**, the simplest shearing interferometer is a glass slide as demonstrated by Bates in 1947 [39]. In our approach, such simple glass slide interferometer (without prism and plasmonic layer) can serve to calibrate the wavelength-to-current sensitivity factor (S) of our laser source. (It can also be used as a first step to select a proper glass substrate for the SiSPR fabrication process, judging on the interference quality). To express latter on the wavelength-to-current sensitivity factor, it is important that we introduce glass slide based shearing interferometer and its OPD in this part.

Fig. 30 (a) demonstrates how in general the glass slide based shearing interferometer is set-up, and **Fig. 30 (b)** and **(c)** reveal the wavefront divisions and show how the OPD can be calculated. Again, we will performance our analysis on two sub-beams, i.e. Sub-beam1 (gray) and 2 (purple). In this example, the beam source first impinge from air (n=1) into the glass (n=1.5). Due to the difference of refractive index, beam 1 will be refracted while the beam 2 is reflected. Finally, beam 1 will be reflected again and undergoes another refraction and then over-lap with the beam 2.

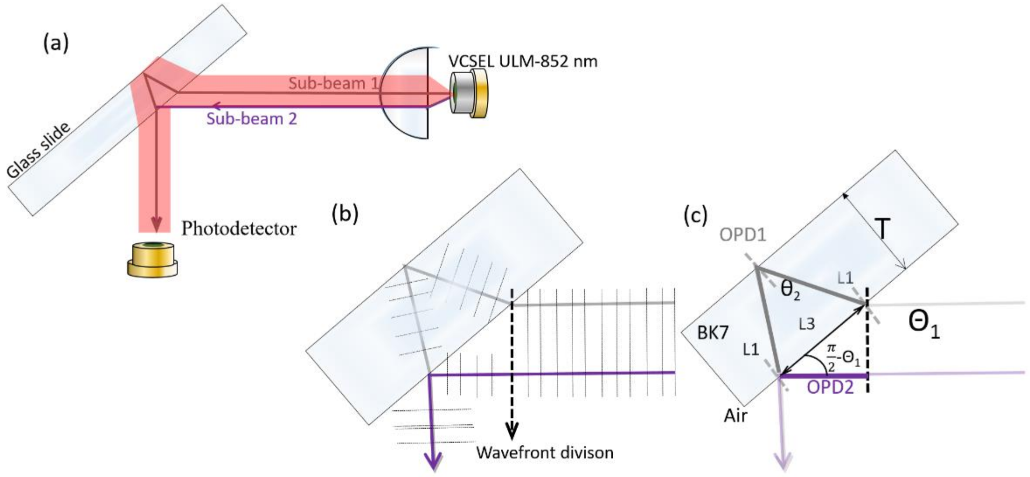

Fig. 30 Glass slide based shearing interferometer
(a) optical set-up of a glass slide based shearing interferometer (b)-(c) wave-front analysis in a glass slide based shearing interferometer for a given beam incident angle.

In **Fig. 30 (b),** the wavefronts of the two sub-beams are depicted using gray dashed lines. To calculate the OPD, we first consider the path length between the points of wave-front division and the recombination point for both beams. In case of sub-beam 1, it has traveled a length ‘OPD1’ while sub-beam 2 has traveled a length ‘OPD2’ (cf. **Fig. 30 (c)**).

doi:10.6342/NTU201700804

Another variable that is important in present discussion is the incident angle of the beam (θ1). When sub-beam 1 travels into the glass, it is first refracted as discussed earlier and then reflected by the glass-air interface with an angle of θ2. Finally, the sub-beam 1 is refracted again and combined with the sub-beam 2. According to Snell's law, θ2 is simply:

$$\theta_2 = sin^{-1}\left(\frac{n_{air}}{n_{BK-7}} \times sin\theta_1\right) \quad \textbf{Eq. 17}$$

With n_{BK-7} the refractive index of the glass material (e.g. BK-7 glass). Since we know θ_2, we can then determine OPD1 by following equation:

$$OPD1 = 2n_{BK-7}L_1 = 2 \times n_{BK-7} \times \frac{T}{cos(\theta_2)} = 2 \times 1.5 \times \frac{T}{cos(\theta_2)} \quad \textbf{Eq. 18}$$

Where for BK-7 glass slide that we use, the thickness of the slide is around 1 mm. To further calculate OPD2, L3 must be known. Therefore, we found that L3 equals to:

$$L_3 = 2 \times \frac{T}{cos\theta_2} \times sin\theta_2 \times cos\left(\frac{\pi}{2} - \theta\right) = 2T \times tan\theta_2 \times sin\theta_1 \quad \text{Eq. 19}$$

We therefore have OPD2 equals to:

$$OPD2 = 2 \times 1.5 \times \frac{T}{cos(\theta_2)} - 2T \times tan\theta_2 \times sin\theta_1 \quad \textbf{Eq. 20}$$

Fig. 31 blue trace shows the angle dependence for this OPD. Having established the OPD, we can now detail how the phase can be extracted in our compact system. As demonstrated in the inset, the OPD range between 2.7~2.3 mm from 40 degree incidence

doi:10.6342/NTU201700804

to 70 degree incidence.

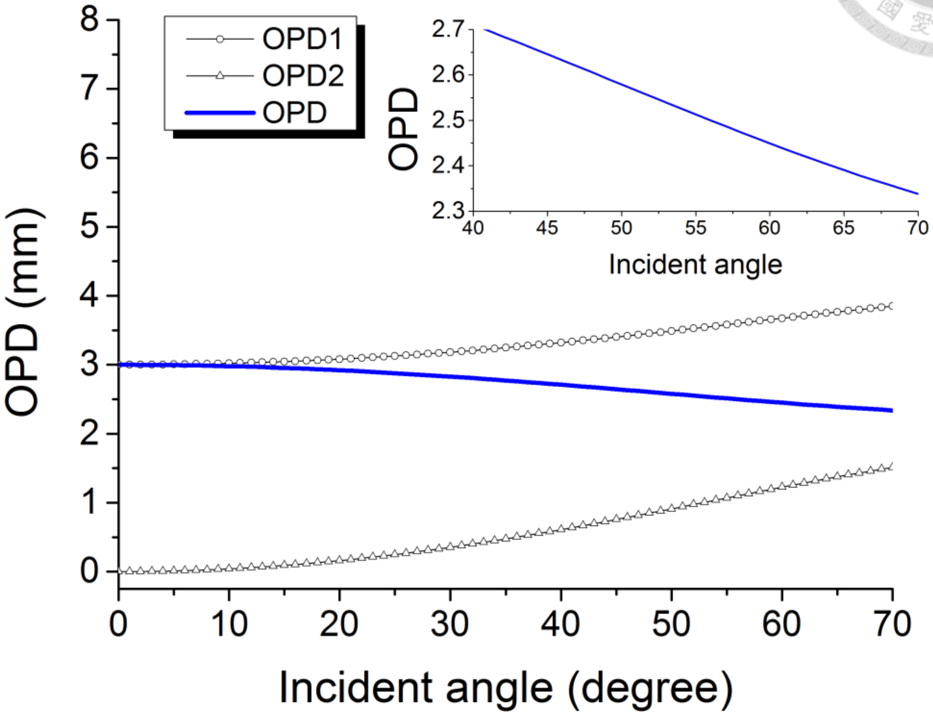

Fig. 31 Angle dependence of OPD in glass slide based shearing interferometer. The blue line indicates the OPD while the black line with circle symbol indicates OPD1 and the triangle symbols mark the OPD2. The inset provides OPD-incident angle dependence between 40-70 degree of incidence.

Section 8-3. SiSPR interferogram and phase retrieval method

After this introduction on how interferences are generated in SiSPR and the OPD, this section will take a mathematical turn by describing how the phase can be extracted from an interferogram generated by a sinusoidal phase modulation within our system. The main focus of this section is to walk through the essence of the developed phase extraction method. For this purpose, our main focus here is on the six parameters that are involved in our phase extraction method, i.e. phase modulation depth ($\Delta\phi_a$), amplitude of current

doi:10.6342/NTU201700804

modulation (di), wavelength-to-current sensitivity factor (S), OPD (L), AC to DC ratio of laser intensity (μ). Through a brief mathematical introduction, we shall reveal what is the interplay between these variable and how do they affect the interferogram as well as the phase extraction method. To avoid an overly lengthy discussion, part of the derivation is actually shifted to the appendix while keep only the essence of it. Interested readers are encouraged to find detailed discussion in this appendix as well in the provided reference 39[40] on generalized lock-in amplifier method.

Before we start the mathematical development, it is important to state again the purpose of SiSPR and the corresponding problematics. As mentioned within the literature review we made, one of the major goal is to provide a phase sensitive SPR that does not require the use of expensive optoelectronic component such as piezo-acutator, AOM, PEM or wavelength tunable source with a large tuning range. These components mainly serves to provide a mean of phase modulation for phase extraction. It is then clear that one of the major challenge herein is to induce phase modulation for a lock-in amplifier based phase extraction, without using any of the above-mentioned item. Consequently, in terms of phase extraction, wavelength modulation of the laser source is the only viable solution for phase modulation. Moreover, this has to be done with a diode that is reasonably low cost (below 250 USD), such as laser diodes. This prevents the use of widely tunable laser source for portable application. In general, the wavelength modulation is induced by

doi:10.6342/NTU201700804

placing a current modulation on laser diode. In case of low wavelength tunability laser diode, this current modulation action would induce not only phase modulation but also amplitude modulation at the same time. This adds complexities for solving the phase as amplitude information cannot be readily distinguished from phase information. To be more specific, in present study, we will be dealing with a Sinusoidal Phase Modulation (SPM) with a strong Amplitude Modulation (AM) at the same frequency. Such situation is not well addressed by conventional methods.

Herein, the Sinusoidal Phase Modulation is considered over a linear one due to noise consideration[f]. We will first use a SPM interferogram signal without AM to introduce the SPM interferogram. Using less complex SPM signal without AM as a starting point, we may introduce the nature of the signal in a more elegant fashion while these concepts are still pertinent to the case SPM with AM. Then a derivation for phase extraction method for SPM interferogram signal with AM is presented. Instead of using conventional lock-in amplifier for phase extraction, a modification of previously reported generalized lock-in amplifier is applied.

Section 8-3-1. SPM interferogram without AM

The **Eq.** ***21*** below gives the mathematical representation of a SPM interferogram without AM:

---

[f] Sawtooth modulations induces so called “flyback” problem.

doi:10.6342/NTU201700804

$$I_{det}(t) = I_0[1 + mcos(\phi_{mod} - \phi_s)] \quad \textbf{Eq. 21}$$

Where $\mathrm{I_{det}}$ is the interferogram signal, $\mathrm{I_0}$ is a constant (no AM), “m” represents the contrast of the interferogram and L is the OPD. Since the ***Eq. 21*** is a case of two beam interferometry, we know that ϕ_{mod} an be expressed as $\phi_{\mathrm{mod}}(t) = \frac{2\pi L}{\lambda(t)}$. In this way, we have:

$$I_{det} = I_0\left[1 + mcos\left(\frac{2\pi L}{\lambda(t)} - \phi_s\right)\right] \quad \textbf{Eq. 22}$$

In case of SPM, where wavelength is modulating sinusoidally with an angular frequency of ω, we can rewrite ***Eq. 22*** :

$$\mathrm{I_{det}} = \mathrm{I_0}\left[1 + \mathrm{mcos}\left(\frac{2\pi \mathrm{L}}{\lambda_0^2} \times \mathrm{d}\lambda \times \sin\omega \mathrm{t} - \phi_s\right)\right] \quad \textbf{Eq. 23}$$

Where $d\lambda$ represent minute change in wavelength. Despite that ***Eq. 23*** provide us with expression of SPM signal, it is not feasible to use $d\lambda$ as variable, since SPM is realized by modulating the current of diode. The current modulation typically leading heating or cooling of laser, which finally lead to wavelength modulation. Simply put, amplitude of current modulation (di) is a more convenient from of variable as compared to wavelength modulation. Consequently, it is more practical to rewrite Eq**. 23** into:

$$\mathrm{I_{det}} = \mathrm{I_0}\left[1 + \mathrm{mcos}\left(\frac{2\pi \mathrm{L}}{\lambda_0^2} \times \frac{\mathrm{d}\lambda}{\mathrm{di}} \times \mathrm{di} \times \sin\omega \mathrm{t} - \phi_s\right)\right] \quad \textbf{Eq. 24}$$

In **Eq. 24**, we have found an intrinsic character of laser, $\frac{d\lambda}{di}$, which is referred to as wavelength-to-current sensitivity factor and will be noted as “S” hereafter. If we replace $\frac{\mathrm{d}\lambda}{\mathrm{di}}$, we then have our final expression for SPM interferogram with $\mathrm{I_0} = cte$ (no AM)

doi:10.6342/NTU201700804

$$I_{det} \sim I_0 \left[1 + m\cos\left(\frac{2\pi L}{\lambda_0^2} \times S \times di\, \sin(wt) - \phi_s\right)\right] \quad \textbf{Eq. 25}$$

Wavelength-to-current-Sensitivity factor (S) and phase modulation depth ($\Delta\phi_a$)

Again, "S" is an empirical property of a given laser which, judging from its formula, determines the degree of wavelength variation we can achieve with a given amount of current modulation. For the diode that is used in present work (VCSEL-ULM852-SingleMode-V22), this value is typically around 0.6 nm/mA. From above discussion, we can see that S will ultimately determine the extent of phase modulation. The laser with large S, such as tunable laser, could provide large range of phase modulation. While in case of VCSEL, considering its limited current working range and low wavelength tunability, the maximum extent of phase modulation naturally becomes a critical issue, if lock-in based method is applied.

To qualitatively comprehend the role of S in phase modulation, we should introduce now another important variable in SiSPR. That is the phase modulation depth, which will be noted as $\Delta\phi_a$ hereafter. $\Delta\phi_a$ can be expressed as:

$$\Delta\phi_a = \frac{2\pi L}{\lambda_0^2} \times S \times di \quad \textbf{Eq. 26}$$

thereby modifying **Eq. 25** into:

$$I_{det} \sim I_0[1 + m\cos(\Delta\phi_a \sin(wt) - \phi_s)] \quad \textbf{Eq. 27}$$

It is easier to understand the physical meaning of the $\Delta\phi_a$ by expanding the **Eq. 27**,

doi:10.6342/NTU201700804

giving:

$$I_{det} \sim I_0[1 + m[cos(\Delta\phi_a\, sin(\omega t))cos\phi_s - sin(\Delta\phi_a\, sin(\omega t))\, sin\phi_s] \quad \textbf{Eq. 28}$$

and through *Jacobi-anger expansion* we have

$$I_{det} \sim I_0 + I_0 m cos\phi_s[J_0(\Delta\phi_a) + 2\sum_{n=1}^{N} J_{2n}(\Delta\phi_a)\, cos(2n\omega t)] -$$

$$I_0 m sin\phi_s[2\sum_{n=1}^{N} J_{2n-1}(\Delta\phi_a) sin[(2n-1)\omega t] \textbf{Eq. 29}$$

Where $J_{\mathrm{i}}(\Delta\phi_a)$ is the Bessel function of the first kind of *i^th^* order and having $\Delta\phi_a$ as argument. In other words, an SPM interferogram (without AM) is a signal that is composed of a series of even and odd harmonics and the intensity of each harmonic component is determined by the value of $\Delta\phi_a$. For example, if $\Delta\phi_a$ = 3.8317 rad (the value that we will be using in practice), the interferogram can be represented by:

$$I_{det} \sim I_0 + I_0 \mathrm{m cos\phi_s}[-0.402 + 0.806 \cos(2\mathrm{\omega t}) + 0.51 \cos(4\mathrm{\omega t}) + \cdots]$$

$$- I_0 \mathrm{m sin\phi_s}[0.8406 \sin(3\mathrm{\omega t}) + 0.226 \sin(5\mathrm{\omega t}) + \cdots]$$

Since $\mathrm{J}_0(3.8317) = -0.402$, $\mathrm{J}_1(3.8317) = 6.84 \times 10^{-4}$, $\mathrm{J}_2(3.8317) = 0.403$, $\mathrm{J}_3(3.8317) = 0.4203$, $\mathrm{J}_4(3.8317) = 0.25535$ and $\mathrm{J}_5(3.8317) = 0.113$.

Additional remarks on $\boldsymbol{\Delta\phi_a}$ and S

The value of $\Delta\phi_a$ determines the waveform of the interferogram. ***Fig. 32*** shows examples of waveforms obtained for different $\Delta\phi_a$. Due to the property of Bessel function $J_{\mathrm{i}}(\Delta\phi_a)$, for large $\Delta\phi_a$ values, our interferogram will have more weight on higher harmonics. All of these harmonics are transporting an information on the signal

doi:10.6342/NTU201700804

phase via a factor $\cos(\phi_s)$ for even harmonics and $\sin(\phi_s)$ for odd harmonics. To determine unambiguously the phase information, both $\cos(\phi_s)$ and $\sin(\phi_s)$ should be extracted. LIA on two harmonics can be used to do so (one odd and one even). Alternately, a Generalized LIA can be used to extract the phase from all the harmonics simultaneously. Confined by the length and scope of the thesis, readers are encouraged to find more detail in the appendix Section A1-A2.

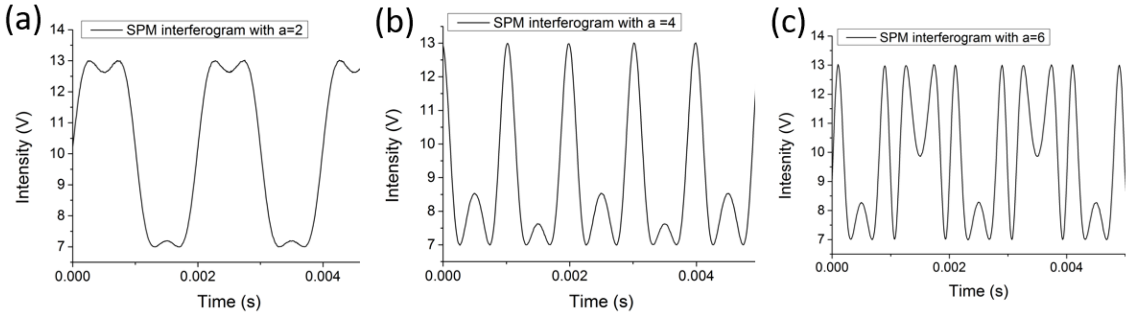

Fig. 32 The SPM interferogram for several phase modulation depths (a)$\Delta\phi_a$=2 rad, (b)$\Delta\phi_a$=4 rad, (c) $\Delta\phi_a$=6 rad.

Another point that worth discussion is the dependence of $\Delta\phi_a$ on L, di and S. In reality, for the lasers we have considered, S is typically on order of ~1 nm/mA, and the maximum value of di should be within the working range of the laser diode. In consequence the achievable phase modulation depth $\Delta\phi_a$ is also limited and the thickness of the glass also matters.

Section 8-3-2. Phase extraction in SPM interferogram with AM

Now, we will consider the phase extraction in SPM interferogram with an additional AM, which is the case in practice. Therefore, in contrast with **Eq. *10***, we now have:

doi:10.6342/NTU201700804

$I_{det} \sim I_0(1+\mu sin(\omega t))(1+mcos\left(\Delta\phi_a sin(\omega t)+\phi\right)$ **Eq. 30**

We note that μ is the ratio between the modulation amplitude of the laser intensity and the averaged intensity of the laser. The extraction process can be divided in 3 steps as shown in **Table 3**. It can be shown that the phase extraction process is immune to the AM for $\Delta\phi_a = 3.8317$ rad (“criterion”).

Table 3. Working flow of phase extraction in SiSPR

Criterion	$\Delta\phi_a = 3.8317$rad
Step 1	Pass the SPM signal with AM through a high pass filter (f_{3db}= 20Hz)
Step 2	Generalized Lock-in Amplifier (G-LIA) process with the following reference functions: Reference X= cos(3.8317sin(ωt)) Reference Y= cos(3.8317sin(ωt))
Step 3	Phase extraction from the R_X and R_Y outputs of G-LIA (from their analytical expressions)

To begin with, the **Eq. *30*** can be further expanded into:

$I_{det} \sim I_0[1+mcos(\Delta\phi_a sin(\omega t)+\phi)]+\mu sin(\omega t)[1+mcos(\Delta\phi_a sin(\omega t)+\phi)]$ **Eq. 31**

To extract the phase, we need to exclude I_0 through a high pass filtering (step 1). From $Idet \sim I_0[1+mcos(\Delta\phi_a sin(\omega t)+\phi)]+\mu sin(\omega t)[1+mcos(\Delta\phi_a sin(\omega t)+\phi)]$ **Eq. *31***, we shall separate the signal into two parts:

doi:10.6342/NTU201700804

$$I_{det-part1} \sim I_0[1 + mcos\big(\Delta\phi_a sin(\omega t) + \phi\big)] \quad \textbf{Eq. 32}$$

$$I_{det-part2} \sim \mu sin(\omega t)[1 + mcos\big(\Delta\phi_a sin(\omega t) + \phi\big)] \quad \textbf{Eq. 33}$$

As mentioned, the signal is first passed through a high pass filter, giving

$$\widetilde{I_{det-part1}} = \; mI_0 cos\big(\Delta\phi_a sin(\omega t) + \phi\big) - mI_0 cos(\phi) J_0(a) \quad \textbf{Eq. 34}$$

And

$$\widetilde{I_{det-part2}} \sim m\mu sin(\omega t) + m\mu cos\phi \; sin(\omega t)[J_0(\Delta\phi_a) + 2\sum_{n=1}^{N} J_{2n}(\Delta\phi_a) \, cos(2n\omega t)] \; - m\mu sin\phi \; sin(\omega t)\big[J_1(\Delta\phi_a) sin(\omega t) + 2\sum_{n=2}^{N} J_{2n-1}(\Delta\phi_a) \, sin\big((2n-1)\omega t\big)\big] - \frac{1}{2} m\mu sin\phi J_1(\Delta\phi_a) \quad \textbf{Eq. 35}$$

These signals are then digitally mixed with our reference function giving:

$$R_X = \frac{1}{T}\int_0^T [\widetilde{I_{det-part1}} + \widetilde{I_{det-part2}}] \times cos(\Delta\phi_a \, sin(\omega t)) \, dy \quad \textbf{Eq. 36}$$

$$R_y = \frac{1}{T}\int_0^T [\widetilde{I_{det-part1}} + \widetilde{I_{det-part2}}] \times sin(\Delta\phi_a \, sin(\omega t)) \, dy \quad \textbf{Eq. 37}$$

As is shown in detail in appendix section A2, we obtain the following results:

$$R_X = \frac{I_0 m}{2} cos\,\phi[1 + J_0(2\Delta\phi_a) - 2J_0^2(\Delta\phi_a)] + \frac{I_0 m\mu}{2}[J_1(2\Delta\phi_a) - 2J_1(\Delta\phi_a)J_0(\Delta\phi_a)]$$

$$R_y = \frac{I_0 m}{2} sin\phi\big(1 - J_0(2\Delta\phi_a)\big) + \mu I_0 J_0(\Delta\phi_a) J_1(\Delta\phi_a) + \frac{\mu m I_0}{2} J_1(2\Delta\phi_a) cos\phi$$

Now that we have the full expression of R$_X$ and R$_Y$ for carrying out phase extraction of SPM interferogram with AM signal, there are just few steps before we can extract the phase. As mentioned previously in the ***Table 3*** without any explanation, we have decided $\Delta\phi_a$ =3.8317 rad as a criterion for the phase extraction. For this value, the $\mu I_0(\Delta\phi_a) J_1(\Delta\phi_a)$ term becomes zero making the Rx and Ry much easier to handle. In this way, Rx and Ry are:

$$R_X = \frac{I_0 m}{2} cos\,\phi[1 + J_0(2\Delta\phi_a) - 2J_0^2(\Delta\phi_a)] + \frac{I_0 m\mu}{2} J_1(2\Delta\phi_a) sin\phi \quad \textbf{Eq. 38}$$

$$R_Y = \frac{I_0 m}{2} sin\phi\big(1 - J_0(2\Delta\phi_a)\big) + \frac{\mu m I_0}{2} J_1(2\Delta\phi_a) cos\phi \quad \textbf{Eq. 39}$$

Since we have $\Delta\phi_a$ =3.8317 rad, we have $J_0(2\Delta\phi_a)$ = $J_0(7.66)$ =0.241, $J_0(\Delta\phi_a) = -0.403$ and $J_1(2\Delta\phi_a) = 0.17304$. Therefore, we have

$$R_X = 0.92\,cos(\phi) + 0.17\mu\,sin(\phi) \quad \textbf{Eq. 40}$$

$$R_Y = 0.759\,sin(\phi) + 0.17\mu cos(\phi) \quad \textbf{Eq. 41}$$

Based on this result, we have our final governing equation for phase retrieval:

$$\phi_{SPR} = arctan2\left[\frac{\big(1 + J_0(2\Delta\phi_a) - 2J_0^2(\Delta\phi_a)\big)R_Y - \mu J_1(2\Delta\phi_a)R_X}{\big(1 - 2J_0(2\Delta\phi_a)\big)R_X - \mu J_1(2\Delta\phi_a)R_Y}\right] \quad \textbf{Eq. 42}$$

Final remark on phase extraction method

In this section, we have first defined the problematics and the methodology for SiSPR phase extraction. Through our discussion above, we managed to find a convenient phase modulation depth ($\Delta\phi_a = 3.8317\,rad$) to extract phase information from SPM interferogram with AM. To the best of our knowledge, such method is not proposed in any literature.

In practice, $\Delta\phi_a$ is an implicit variable that can be manipulated linearly by playing with the amplitude of current modulation (di) (cf. **Eq.** *26*). A stronger current modulation, leads to higher $\Delta\phi_a$. In other words, in practice, we control the harmonic components of the time-domain interferogram through di. Arriving at the very specific value $\Delta\phi_a$, in

doi:10.6342/NTU201700804

our case 3.8317 rad, requires pre-knowledge of a number of other variables. These variables includes wavelength of laser ($\lambda_0 = 850$ nm in our case), the optical path difference at Kretschmann angle (~0.78 mm as demonstrated in ***Fig. 29***) related to the cover glass thickness and wavelength-to-current sensitivity factor S (0.6~1.2 nm/mA as will be shown later on). Since OPD and wavelength can be estimated with high precision and di is the controlled variable, this makes the estimation of S an important work. Only when S is

Table 4. Quantities involved in the phase extraction method developed for SiSPR

Variable	**Description**
di	1.Controlled variable (current modulation) 2.limited working range
$\Delta\boldsymbol{\phi_a}$	1.determine the harmonic component of interferogram 2.Linearly dependent on di (Needs to be 3.8317 rad for phase extraction)
S	1.Typically between 0.6 nm/mA~ 1.2 nm/mA 2.The measurement precision on S mostly determines the precision on $\Delta\phi_a$
L	1.Optical path difference (OPD) determined from geometrical analysis 2.Equals to ~0.78 mm for Kretschmann angle in water (and glass thickness of 1mm)
$\boldsymbol{\lambda_0}$	Central wavelength. 850 nm in present work
μ	Relative depth of the amplitude modulation (can be expressed in percents). Empirically before experiment

doi:10.6342/NTU201700804

precisely determined, can we obtain a precise $\Delta\phi_a$ value and extract the phase information from the interferogram. For this purpose, we have set up an optical method for calculating the S value, as will be demonstrated in chapter 9. With the estimated S value, we will obtain the exact working point for the amplitude of di. For a more visual appreciation of the involved variables and their role, the list of parameters is provided in **Table 4**.

Section 8-4. SiSPR Laboratory prototype

A laboratory prototype has been established for SiSPR as shown in **Fig. 33**. The set-up helps to study the theoretical aspect of SiSPR as well as for designing a miniaturized prototype. The VCSEL laser used in present work is ULM852-10-TN-S46FZP with emission wavelength of 852 nm, 0.5 mW minimum emission power. The VCSEL typically has a threshold voltage (V_{th}) at i_{th}=0.56 mA, while the current bias upper limit is 2.0 mA. To precisely reach a $\boldsymbol{\Delta\phi_a}$ of 3.8317 rad**,** the S for each VCSEL should be carefully measured, to makes sure the phase extraction procedure will work.

The VCSEL is mounted on a 1-D translational stage for fine control of the laser position. This allow us to tune the collimation condition. A 3-D printer made spherical lenses holder is fixed onto the goniometer system. The prism holder also has four fixing points to anchor the SiSPR chip and the microfluidic system used to convey the analyte. The goniometer system has an angle resolution down to 0.014 degree. To detect the

doi:10.6342/NTU201700804

inteferogram, our tailor made detector is composed of: a dual channel amplifier/read-out circuit, two photo-detectors and one polarization beam splitter.

.

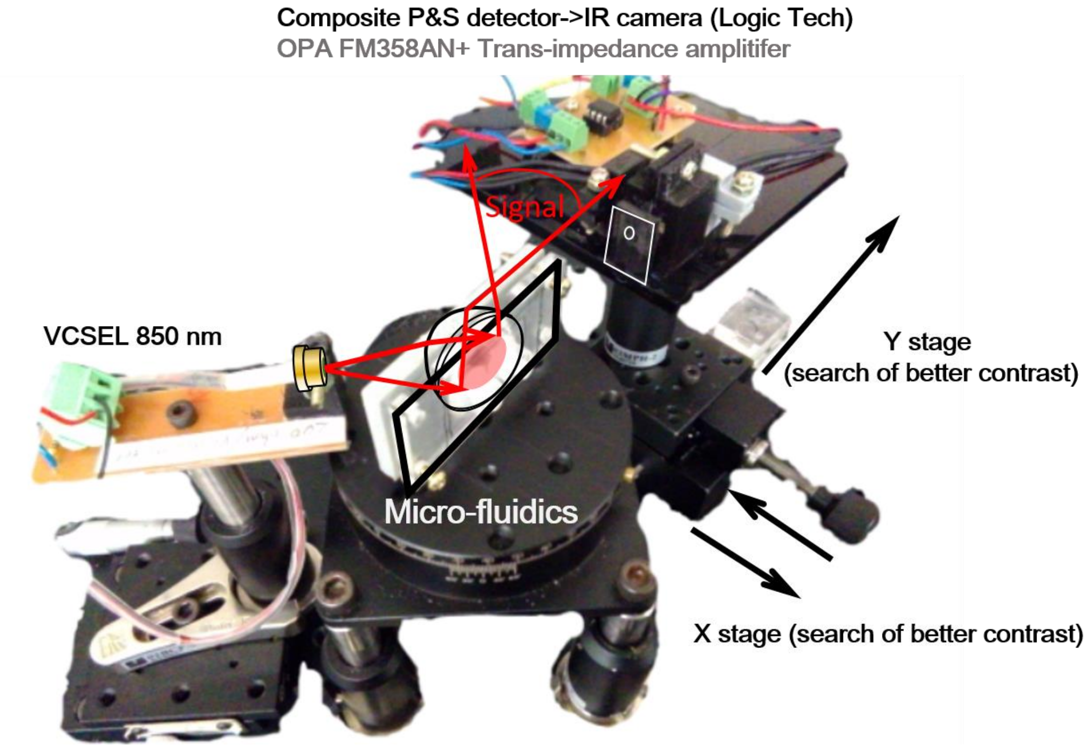

Fig. 33 SiSPR laboratory prototype.

The detectors can then pick-up both S and P signal separately for calculating P-S differential phasogram. The detector is mounted on a rotating bar to search for Kretschmann angle. The bar is actually one arm of a goniometer whose rotation axis coincide with the laser spot on the plasmonic layer. The detector can move freely along the bar and perpendicular to it using a translational stage for fine adjustment. In this way, the detector can be placed at the position providing the best interferometric contrast for sensing. For fluidic sensing experiment, a PMMA microfluidic system is made via Versa

doi:10.6342/NTU201700804

laser^{TM} Computer Numberic Control (CNC) cutter from A Sun Photonic Co. in Taiwan. The PMMA microfluidic has a tailor-made syringe connect that can connect to a syringe via PE-20 tubing. The microfluidic is then combined with SiSPR chip via a double face adhesion.

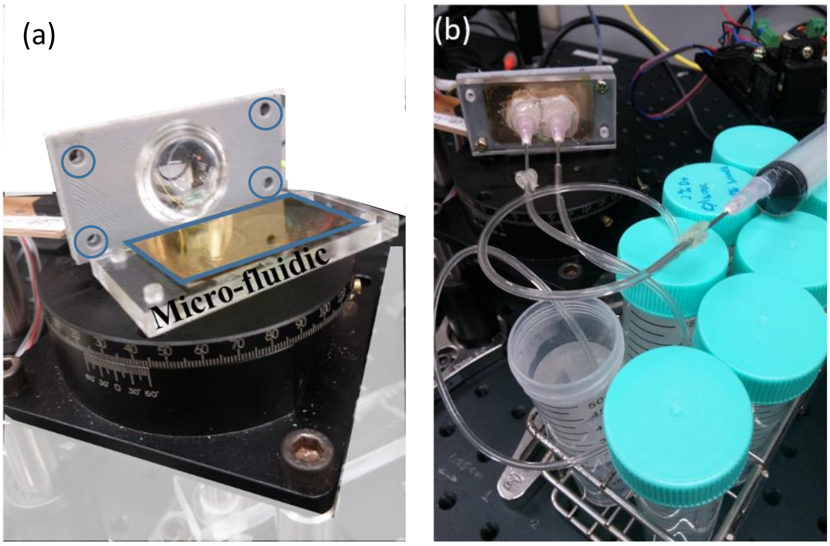

Fig. 34 SiSPR chip with microfluidic system
(a) SiSPR chip coupled with microfluidic before fix onto the laboratory prototype (b) SiSPR chip coupled with microfluidics and fixed onto the prototype for measurement .

The adhesive is shaped by CNC laser cutter to define the microfluidic pattern (Typically, rectangular shape). As shown in **Fig. *34*** (a), the SiSPR chip with microfluidic can be fixed onto the prism holder through four fixing hole with M3 thread. **Fig. *34*** (b) reveal a photograph when SiSPR system is carrying out fluidic sensing.

Section 8-5. Fabrication of SiSPR chip

The fabrication process of SiSPR chip plays a vital role in the signal-to-noise performance of the sensing process. It can be mainly divided into two steps: First,

doi:10.6342/NTU201700804

selection of the cover glass. Second, deposition of metal film.

Unlike conventional SPR, where the condition of the glass substrate has little effect on sensing quality, SiSPR sensing performance is strongly dependent on glass substrate. As in case of any interferometry, the contrast is best when reference wavefront is perfectly collimated and paralleled with the signal wavefront. Having this in mind, we can know that, in SiSPR, the contrast is largely determined by the quality of glass slide surfaces. For example, if two face of the glass substrate is not parallel, the SiSPR would have a reference beam and signal beam with slightly different propagation direction leading to reduced contrast level. Consequently, only glass that is highly parallel is selected for SiSPR.

For selection of glass, a glass slide based shearing interferometer system is set up as shown in the ***Fig. 35*** below, to test the cover glass quality. The same beam source that we used in SiSPR laboratory prototype is used. In case of this set-up, we arbitrarily choose 65 degree incidence. The glass slide that can generate strong contrast without use of iris is selected. The size of the area with good contrast is also important. Some cover glasses have a good contrast over 1 cm area (***Fig. 35*** **(c)-(e)**), while some of them have good contrast in scattered and isolated area over the glass. In general, we use only the glass that has strong contrast over 1 cm. In a box of 100 glass slides, only 5-7% are of sufficient quality for SiSPR application.

doi:10.6342/NTU201700804

After the selection process, gold and ZnO is deposited using a sputter system purchased from Industrial Technology Research Institute of Taiwan (ITRI) or using thermal evaporation (Plassys MEB400, for metal evaporation only, calibrated via AFM measurement of the deposited layer). The reflective layer is composed of 2nm of adhesion layer (zinc oxide) plus 8 nm of gold. The plasmonic layer is composed of 2 nm zinc oxide plus 47 nm of gold. In sputter process, the power of the plasma is around 30 W. For the gold evaporation, a linear calibration on film thickness again evaporation time is established for the system. Typically, 14 minutes 50 seconds of evaporation provides a film thickness of 47 nm.

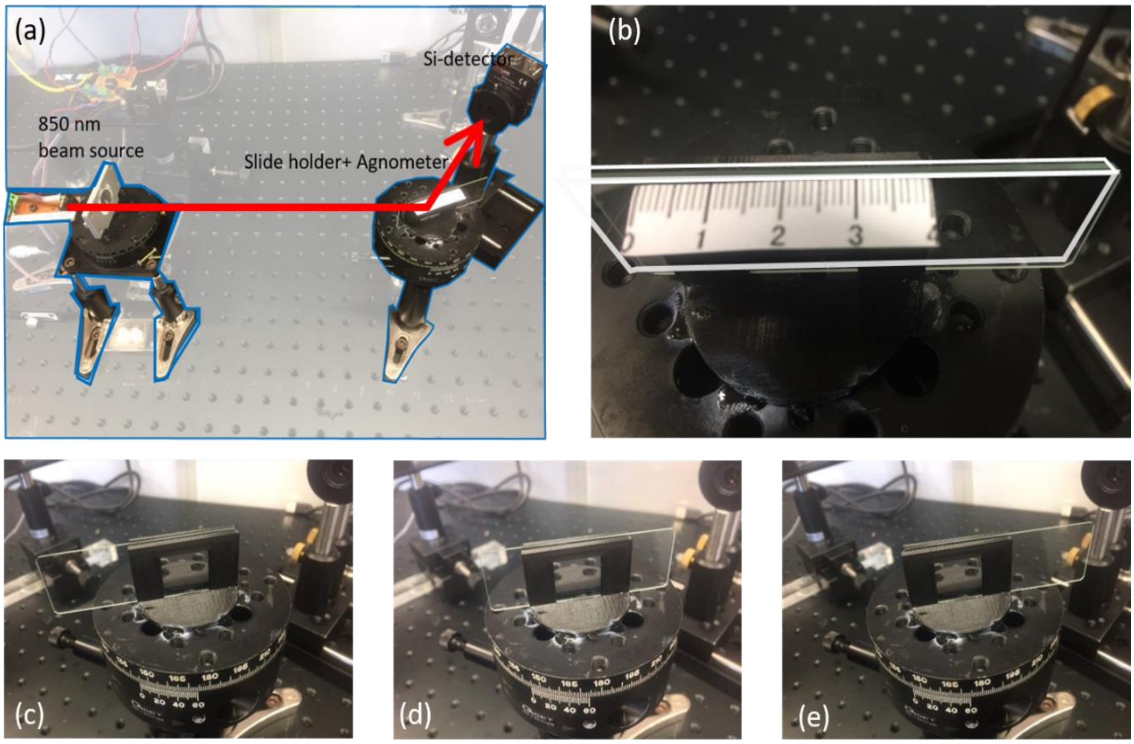

Fig. 35 SiSPR substrate glass selection system.
(a) system overview. (b) rulers for marking different area on the glass substrate. (c)-(e) the holder allows the glass slide to have a degree of freedom to move in the holder, so that contrast level at different area may be examined.

doi:10.6342/NTU201700804

To evaluate the fabrication parameter and the sensitivity of the designed SiSPR chip, we have also carried out numerical simulation based on matlab code that is provided online[g]. The code is modified according to our fabrication parameter which can be found in Appendix Section A3. The simulation is made to calculate the reflectivity of an arbitrary multilayer stack at any angle of incidence, from the knowledge of the thicknesses of the materials and the Fresnel coefficients (determined by the complex refractive indices).

In the simulation, the metal and oxide film thickness is set as our fabrication parameter as shown above, except that plasmonic layer has a thickness between 44-50 nm to study the effect of film thickness on SPR sensitivity in both phase and amplitude. The wavelength is 850 nm. The coupling prism is BK-7 (n=1.514). The refractive index for ZnO is 1.9540, and it is 0.1649+5.374i for the gold layer. The simulation result can be seem in **Fig. 36** and ***Fig. 37***.

As shown in **Fig. 36**, the reflective dip of SPR typically has its sharpest slope on the left edge, irregards of the film thickness. Also, it is worth to note that film thickness has limited effect on the slope of the left edge. This makes amplitude sensing, if we use only the left edge, relatively insensitivity to film thickness[41].

On the contrary, as can be seen in ***Fig. 37***, film thickness can largely tune the slope of

---

[g] http://eceweb1.rutgers.edu/~orfanidi/ewa/, from prof. Sophocles J. Orfanidis at Rutger University in United States

doi:10.6342/NTU201700804

the SPR phase response. As can be seen, the phase response has a 12.3 times difference

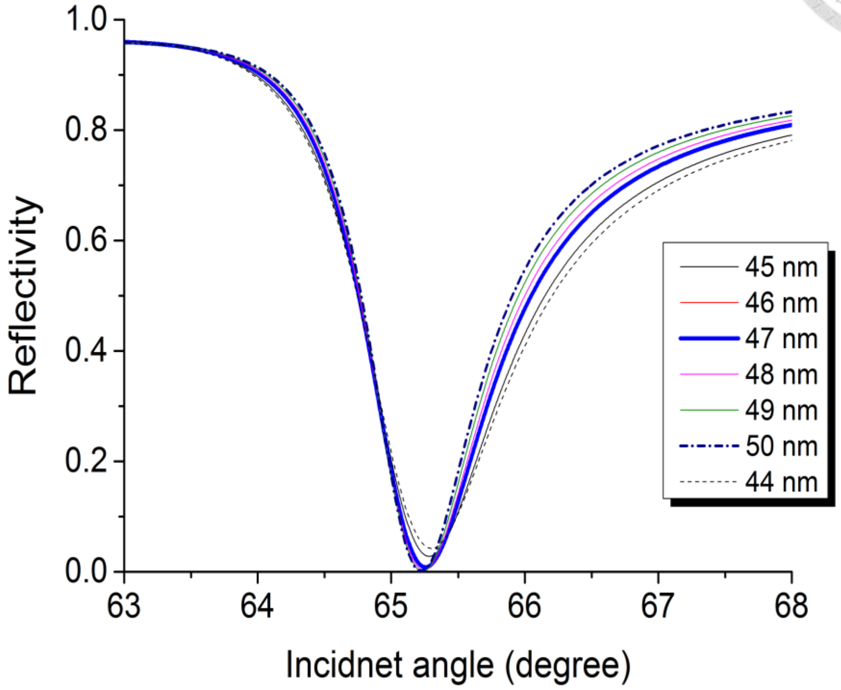

Fig. 36 The simulation of SPR reflective dip with different film thickness.

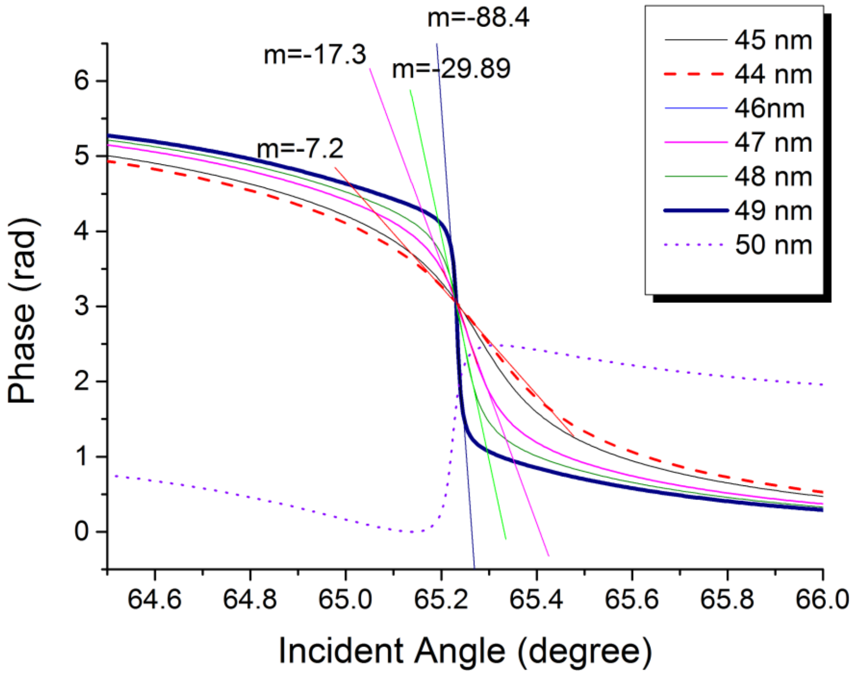

Fig. 37 The simulation of SiSPR phase response with different film thickness.

doi:10.6342/NTU201700804

between film thickness of 44 nm (469 rad/degree) and 49 nm (5771 rad/degree). The sharpest phase response is mostlikely to be found between 49 nm-50 nm of gold thickness. As is well known, the sensitivity and dynamic working range of phase sensitive SPR has a trade off. The higher sensitivity, the narrower linear worknig range. For balance of the two characterisitc, we have choose a film thickness of 47 nm (nomially) for present study.

doi:10.6342/NTU201700804

Chapter 9. Results and discussion

Section 9-1. Numerical Simulation

We will now verify the derived phase extraction method with a numerical simulation. First, a simulated signal in form of SPM inteferogram with AM at $\Delta\phi_a = 3.8317$ rad. Following the working flow in ***Table 3***, the interferogram is sent to a digital 8th order Butterworth filter and then to sent to our phase extraction method. Finally, μ is set at 0.5 which is around the empircal value used in the sensing experiments. The simualtion program is built via National Instrument LabVIEW 2014.

Role of contrast “m” and μ

Fig. 38(a) demonstrate our simulation interferograms signal with different levels of m and μ. The figure reveals the effect of contrast “m”. Although m has no direct role in our phase extraction master equation (**Eq. 42**), it has a direct impact on the signal to noise ratio. As can be seen from the figure, the waveform degenerate from a signal with higher harmonic components into one having nearly only the fundamental frequency. This is because the m determines the magnitude of phase modulation terms in SPM interfergram (cf.**Eq.** ***30***).

In the Fourier spectrum of the interferogram (cf. **Fig. 38 (b)**), we can see the harmonic compositions of the signal under different combination of m and μ. When m is

doi:10.6342/NTU201700804

much smaller than μ, we can see clearly in this frequency domain that the signal has nearly only the fundamental frequency. In real measurement environment, the noise would be eventually larger than the signal harmonic components, when m is too small, resulting in very noisy phasogram as we will see.

Simulated phase extraction

To verify the vadality of the phase retrieval method, ϕ_{SPR} is set to vary from $-\pi$ to π with a slope of 0.1 radian per step as demonstrated in **Fig. 39**. The retrieved ϕ_{SPR} is then compared to the actual ϕ_{SPR}.

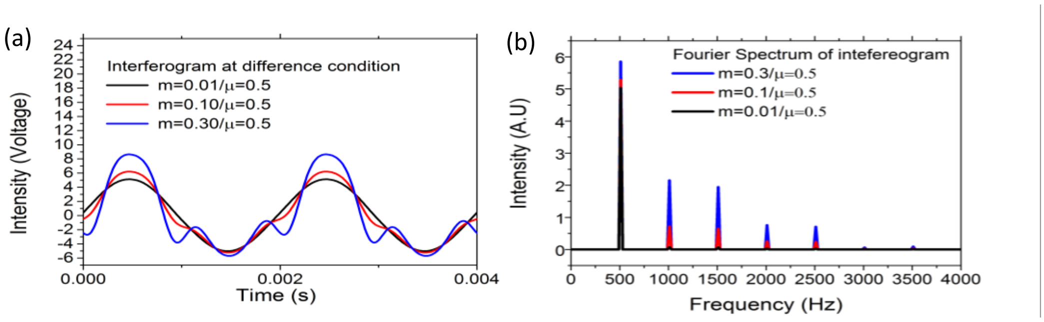

Fig. 38 Simulation signal of SPM intergerogram with AM.
.(a) waveform of the interferogram when μ=0.5 under different m. (b) The Fourier spectrum of the interferogram in (a).

In the figure, the black curve is the ϕ_{SPR} while the red curve is the retrieved phase with m=0.01 and μ=0.5 (very weak contrast and large current modualtion condition). We can see that even under such circumstances, the retrieved phase faithfully follows the ϕ_{SPR} between the entire $-\pi$ to π range, verifying the vadlidity of the proposed method.

To see the effect of noise at low contrast, we carried out another round of phase extraction simulations, in the difficult case of a very weak contrast and a large AM

doi:10.6342/NTU201700804

(m=0.01 and μ=0.5). A Gaussian white noise with a standard deviation of 0.1 is added. The result is shown in **Fig. 39** with a blue trace. As can be seen from the figure, due to the use of Lock-in, ϕ_{SPR} can still be extracted in the entire $-\pi$ to π range. However, noise is very strong making highly precise measurement impossible.

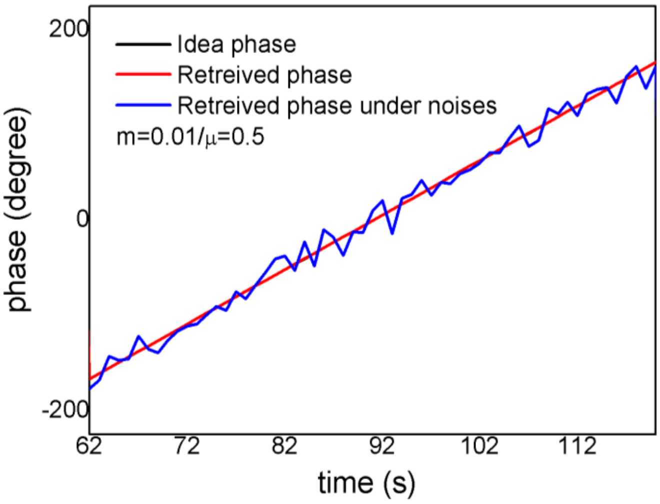

Fig. 39 Simulation of ϕ_{SPR} retrieval.
The difference between ideal ϕ_{SPR} (black line) and the retrieved phase (red line) without noise is negligible so that two curves are actually merged together. Blue curve indicates the phase retrieved under condition of large noises and very weak contrast.

In conclusion, the proposed phase extraction method can work between $-\pi$ to π full range. To guarantee a high signal-to-noise ratio in phase, it is very important to select glass with high contrast.

Section 9-2. Determining “S” of VSCEL and “$\Delta\phi_a$” of the SPM

To determine the S, the Linear Phase Modulation Interferometry (LPMi) is applied on the SiSPR chip using the laboratory prototype shown in **Fig.** *33*. To precisely determine

doi:10.6342/NTU201700804

the OPD, and thereby precisely determiner S, the SiSPR chip is placed at total internal reflection (TIR) angle for glass-air interface (41.8 degree). TIR angle if firstly obtained by the laboratory set-up without the SiSPR chip, by observing the vanishing of refracted beam. After arriving at TIR angle, SiSPR chip is placed onto the laboratory prototype, and a saw-tooth function is applied to the VCSEL laser diode. The saw-tooth current ramp has an amplitude (Δi) of 1.404 mA on the VCSEL laser ($\lambda_0 = 850$ nm) with a constant DC bas of 0.5 mA.[h] At TIR angle, the OPD in SiSPR is around 2.26 mm (optical thickness). The LPMi interferogram is then picked up by our detector. The resulting interferogram can be seen in ***Fig. 40***.

As can be seen in the figure, the interferogram has a sinusoidal function atop its saw-tooth function. It is expected since in case of LPM interferogram (with $I_0 = cte$) the signal is:

$$I_{det} = I_0(t)[1 + mcos(\Delta\phi)] = I_0(t)[1 + mcos(\frac{2\pi L}{\lambda_0^2} S\Delta i)] \quad \textbf{Eq. 43}$$

Where I(t) in this case is in form of piece-wise linear function. Based on above equation, we can drive that:

$$\Delta\phi = \frac{2\pi L}{\lambda_0^2} S\Delta i \quad \textbf{Eq. 44}$$

The advantage of this linear phase modulation interferogram is that the amount of phase

---

[h] Δi=1.404 mA is achieved by setting laser diode at Vdc=2.0 V with a rampe of 0.6 V (The a current limiting resistor of 220 ohm is connect in serie with VCSEL)

doi:10.6342/NTU201700804

change ($\Delta\phi$) can be simply judge from the waveform peak-and-trough, since it follows a simple sinusoidal function. For example, as marked in the figure with the black arrow, as Δi increases, we can observe $\Delta\phi$ from the waveform. Through a collection four of $\Delta\phi/\Delta i$ relation ship (from $\Delta\phi$=0 to 3π), spaced by π), we are able to construct a linear regression between $\Delta\phi$ and Δi (cf. ***Fig. 40***). From the fitted linear regression relationship in ***Fig. 41*** , we know empirically that:

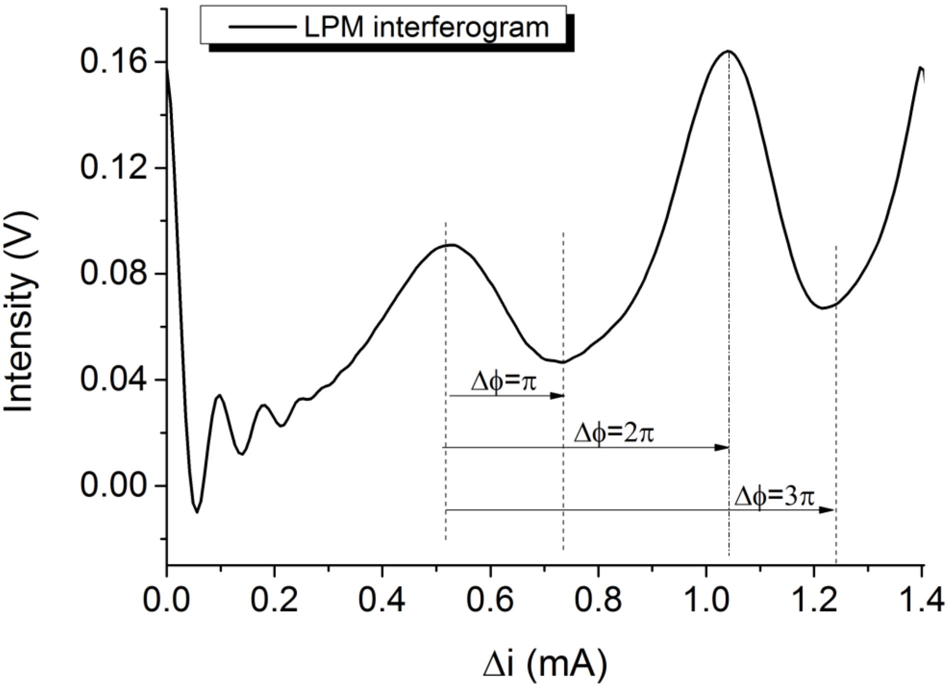

Fig. 40. Laser intensity normalized LPM interferogram.

$$\Delta\phi = 12.9\Delta i \quad \textbf{Eq. 45}$$

And we can derive from :***Eq. 44*** and ***Eq. 45*** that:

$$S = 12.9 \times \frac{\lambda_0^2}{2\pi L} \quad \textbf{Eq. 46}$$

where, as stated earlier, L=2.26 mm, $\lambda_0 = 850\ nm$, we obtain <u>**S= 0.62 nm/mA**</u> for the VCSEL under consideration. Based on the obtained S value, we can now estimate the

doi:10.6342/NTU201700804

amount of Δi needed to generate $\Delta\phi_a = 3.8317$ in case of SiSPR. This estimation is of vital importance as it lies at the core of SiSPR phase extraction. Typically, Kretschmann angle of water lies at 65 degree of incidence (cf. **Fig. 36**). Based on the result from **Fig. 29**, we know that the OPD is 1.267 mm for incident angle of 65 degree. We have therefore come to a $\Delta\phi_a$ vs Δi functions for SiSPR:

$$\Delta\phi_a = 6.793\left(\frac{rad}{mA}\right) \times \Delta i(mA)$$

Which is for the case where Kretschmann angle is at 67 degree. Both of the estimation is plotted in the figure and the insets. In case of 65 degree Kretschmann angle**,** it requires 0.56 mA to obtain meet the condition of $\Delta\phi_a = 3.8317$ for phase extraction.

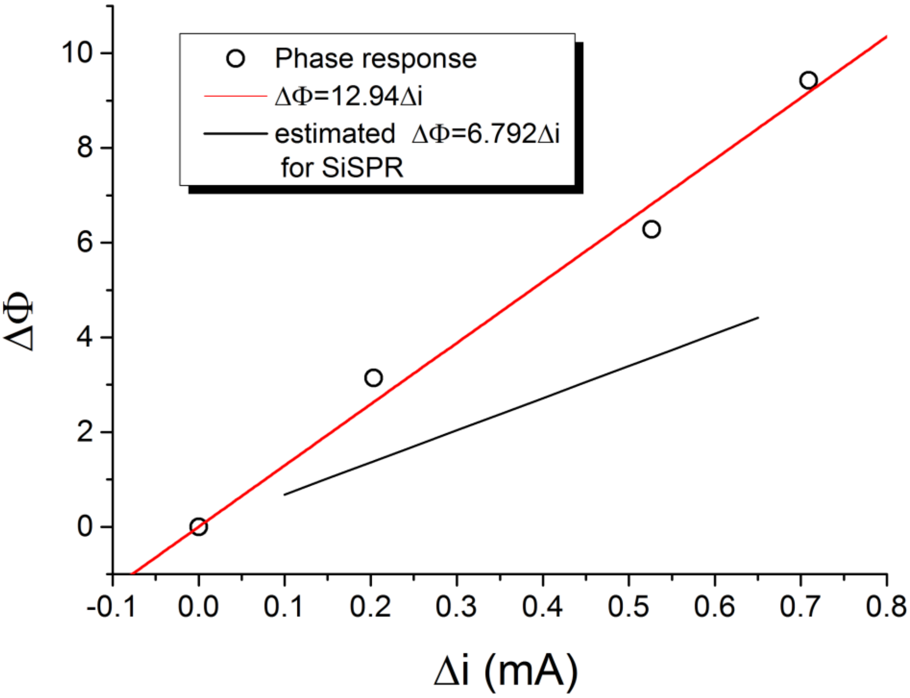

Fig. 41 Fitted $\Delta\phi/\Delta i$ for evaluation of S value.

Note that S value for each VCSEL has to be measured independently for precise

doi:10.6342/NTU201700804

estimation of S and $\Delta\phi_a$. The calculation demonstrated herein serves as an example, but the value may subject to change depending on the diode used.

Section 9-3. Imaging of beam profile of SiSPR

In this part, we will provide an image based analysis on SiSPR interference fringe. To this end, a IR camera is made from model C170 webcam from Logitech^{TM} , Taiwan. As shown in **Fig. *42***, the IR camera is used in place of the P and S photodetector in the laboratory prototype (cf. **Fig. *33***). To image the beam cross sectional profile, the IR camera is placed farther than focal point of the coupling prism. This this distance from prism, the beam is diverging slightly.

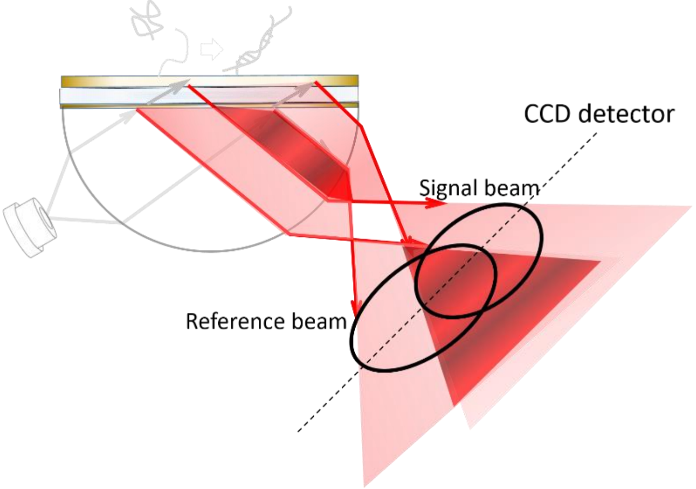

Fig. 42 optical set-up for imaging of the SiSPR beam cross section profile .

The capture can SiSPR beam cross sectional profile and interference can be seen in **Fig. 43.** The image is taken under idc=0.968 mA (Vdc=2.2 V) for VCSEL at different incident angle without any Δi.

doi:10.6342/NTU201700804

For this particular set of SiSPR chip, the reflective layer is 8 nm of gold with 2 nm of adhesion layer. In the captured image, we can clearly observe the signal beam and reference beam as discussion in wave optics analysis (Red circle: signal beam/Blue circle: reference beam). As shown in the image, we can observe clear fringes in the overlapping zone. When SiSPR is placed in air, without any micro-fluidic system, we can see clearly how signal beam is absorbed at 42.5 degree due to the SPR effect. After 43 degree of incidence angle, we can clearly see how signal beam recover its intensity.

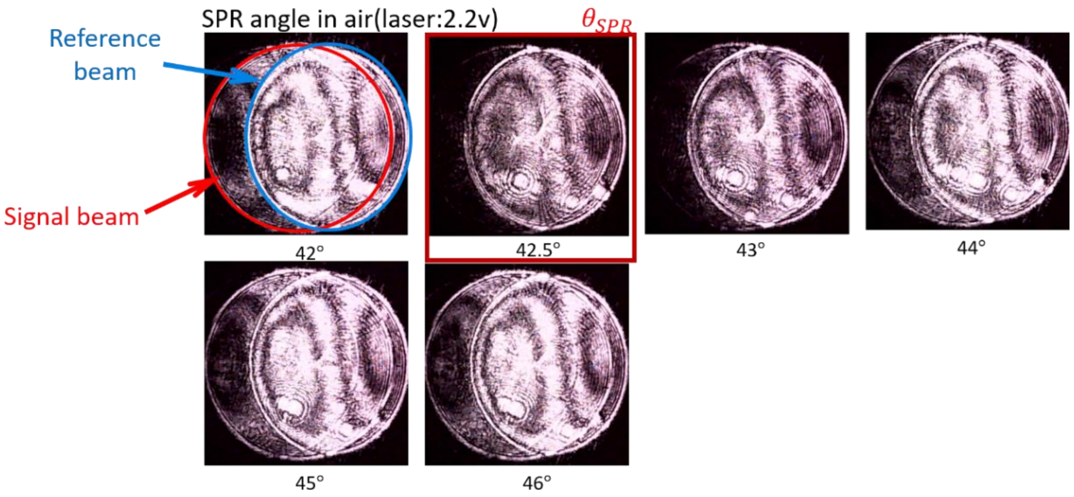

Fig. 43 image of SiSPR fringe and beam cross sectional profile.

We have also performed same image process when SiSPR chip is place under deionized water using microfluidic channel. The result can be seen in ***Fig. 44***. As we can see, the SPR dip is around 65.40 degree, near the simulation results. This angle will be used for SiSPR sensing experiments. We have observed a shape distortion in reference beam, which may likely originated from the relatively small size of prism as compared to beam size, which could be further optimized in near future.

Note that effect of reflective thickness can also be observed by imaging the cross sectional beam profile of SiSPR. As shown in **Fig. *45***, we compare the beam profile between SiSPR chip with different reflective layer thickness. In one chip, the reflective layer is composed of 8 nm of gold plus 2 nm of adhesive layer (right hand side of the

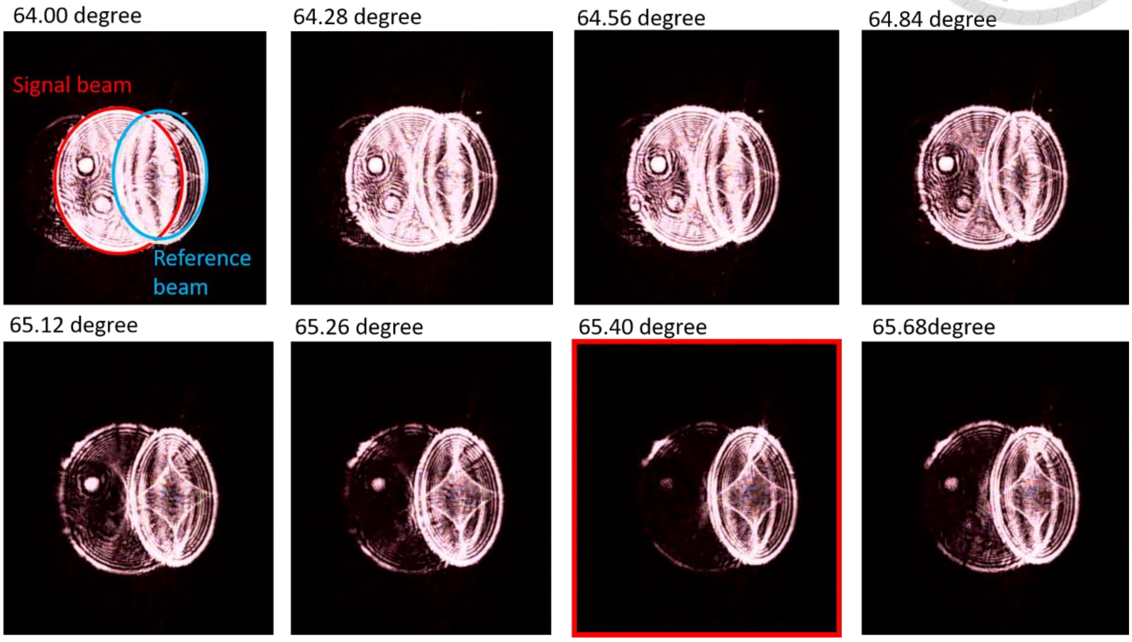

Fig. 44 SiSPR signal when device is under pure water.

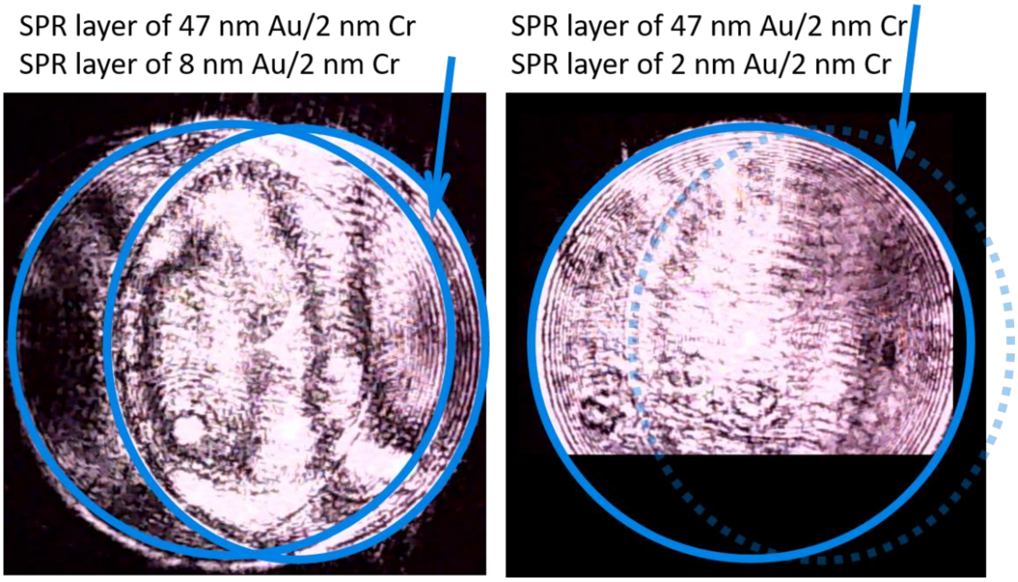

Fig. 45 Image of SiSPR signal with different thickenss of reflective layer.

doi:10.6342/NTU201700804

figure), while another SiSPR chip is composed of 2 nm of Au plus 2 nm of adhesive layer). As can be observed from the figure, when reflective layer is overly thin, the intensity of reference beam would be too small to be observed in the image. Moreover, due to low intensity in reference beam, the contrast is strongly decreased. As result, the fringe can hardly be observed in the image. Therefore, the thickness of SiSPR's reflective layer need to be carefully decided via image based analysis. For present work, the reflective layer is 8 nm of gold plus 2 nm of adhesive layer.

Section 9-4. SiSPR sensing performance:

In this section, we will examine the sensitivity $(\Delta\phi/\Delta n)$ of the SiSPR and compare it with the past literature. For this purpose, the SiSPR chip with 44 nm and 47 nm of plasmonic layer is tested against reference solutions.

To evaluate the sensitivity $(\Delta\phi/\Delta n)$ of SiSPR chips, glucose solutions are used as reference solutions as their refractive index has well defined behavior at λ=850nm with relationship of $n = 0.0018xC + 1.33$, where C is the glucose concentration in terms of weight percentage (w/w%). In this way, the phase response of the SiSPR chip with different surface refractive index can be estimated. The gluocse concentration for reference solutions ranged from 0 % to 11 % (w/w%), which is marked in the upper inset of the figure. The measured phase response is recorded to calculate the sensitivity later on.

doi:10.6342/NTU201700804

Based on our calculation in **chapter 9-2**, we use a V_{DC} of 2.35 V and a V_{AC}=0.239 V to achieve a $\Delta\phi_a$ of 3.8317 rad (Where S~0.62 nm/mA for this typical VCSEL). The μ is measured to be 0.59. Before the measurement, a rough scanning of SPR angle is performed with CCD to find the dip. Then, the P & S photo-detectors are placed around 0.35° higher than the resonance angle. A good level of contrast, as can be seem in ***Fig. 46***, is of fundamental importance to obtain low noise sensing results.

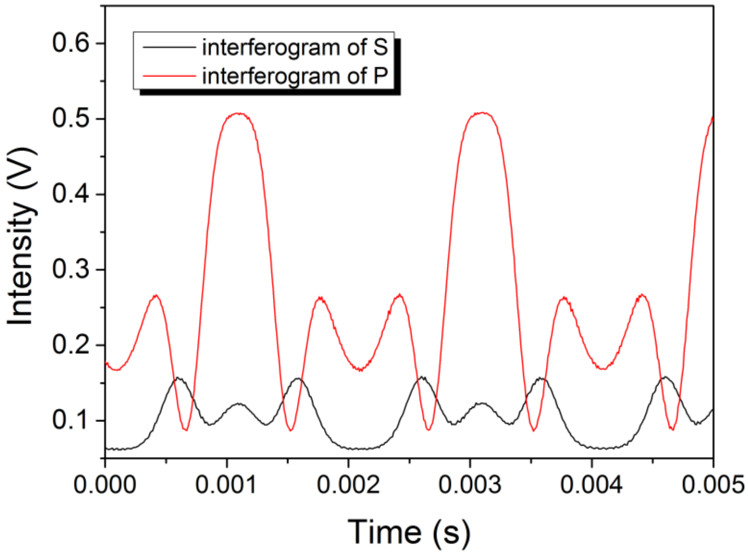

Fig. 46 Interferogram from p-polarization and s-polarization of SiSPR signal.

Fig. 47 and **Fig. *48*** reveals the phase response of SiSPR chips with 44 nm and 47 nm of plasmonic layer thickness. The sensing process are comprised of three consecutive cycles for obtaining statistically significant data. Each cycle starts with D.I water (n as a baseline, followed by several glucose reference solution. For example, in **Fig. *47***, solution of 0.75% (n=1.33135), 0.75% (n=1.33135), 1.00% (n=1.33180), 1.50% (n=1.33270),

doi:10.6342/NTU201700804

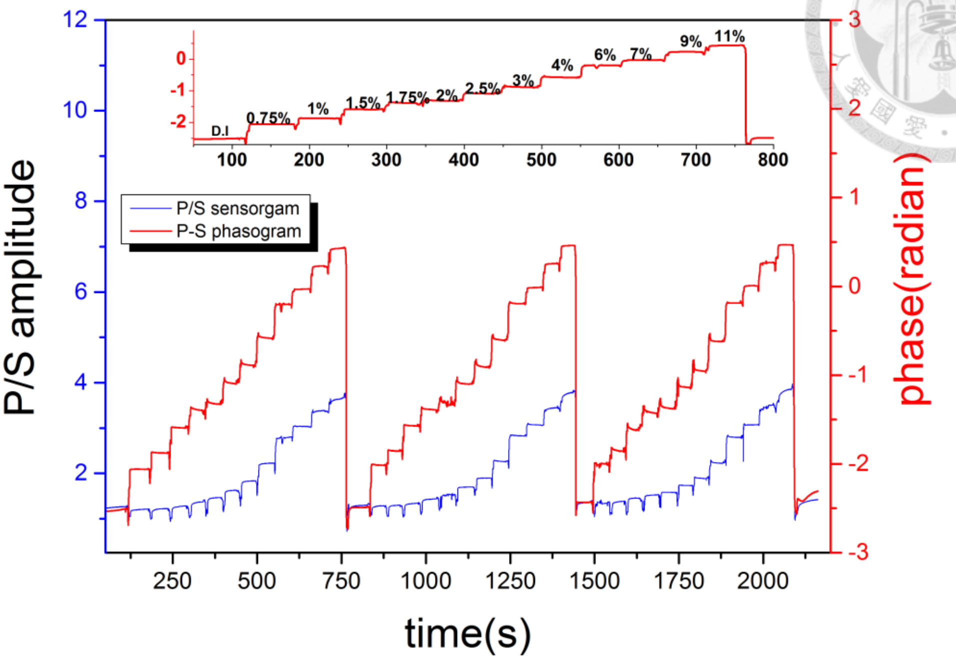

Fig. 47 Phase and Amplitude response of SiSPR chip with 44 nm of plasmonic layer

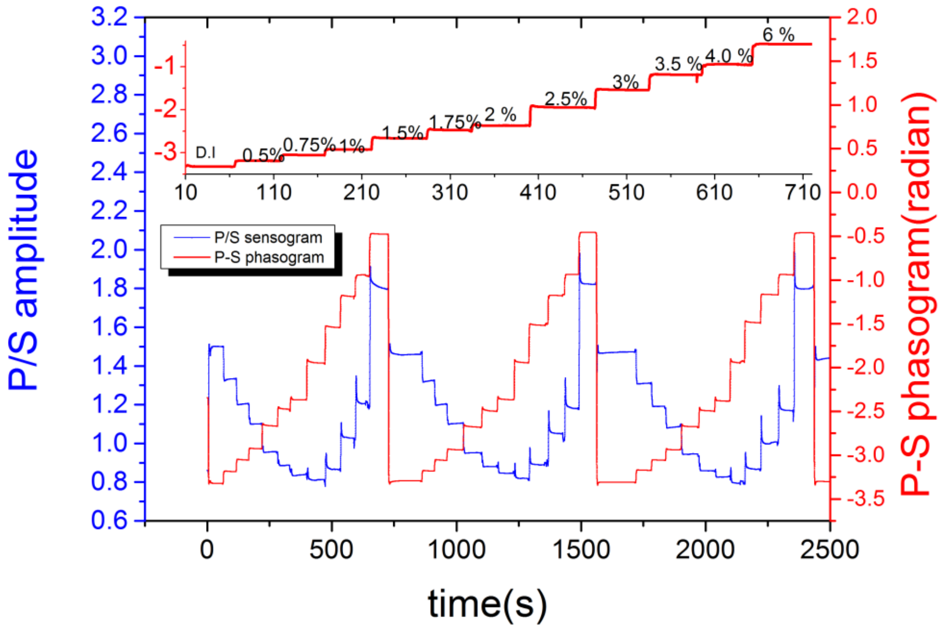

Fig. 48 Phase and Amplitude response of SiSPR chip with 47 nm of plasmonic layer

doi:10.6342/NTU201700804

1.75% (n=1.33315), 2% (n=1.33360) and 2.5% (n=1.33450), 3% (n=1.33540), 4% (n=1.33720), 6% (n=1.3408), 7% (n=1.34260), 9% (n=1.34620) and 11% (n=1.34980) glucose concentraion with a total refractive index change of 0.0198 are used to retrieve $\Delta\phi/\Delta n$ of the SiSPR chip. The phase steps, for one measurement cycle (out of three), are marked with the corresponding concentration in the inset for easy comprehension. The red trace indicates the P-S phasogram, while the blue trace marks the P/S amplitude sensorgram. As can be seen from the figures, when the glucose concentration in the microfluidic channel rises, we observe a monotonic increase in the P-S phase signal. In P/S amplitude sensorgram, we observed first a reflection dip followed by increase in reflection. This trend is expected as we start with an incident angle a bit higher than the resonance angle. Being near the center of the reflective dip, it allows us to give a good estimation of maximum phase sensitivity. In case of 44 nm plasmonic layer, we have observed 3.00 radian over 0.0198 refractive index change, while it is 3.25 radian for 0.0108 refractive index change when plasmonic layer is 47 nm.

Based on the phasogram shown in ***Fig. 47*** and **Fig.** ***48***, $\Delta\phi$ vs Δn calibration curves are built to discuss sensitivity ($\Delta\phi/\Delta n$), dynamic range and minimum resolvable signal of the SiSPR chip. The result can be seen in ***Fig. 49***. Linear fits are applied to the curve to obtain the sharpest response of the chip. The fitted results indicates that:

$$\Delta\phi = 226n - 304 \text{ for SiSPR with 44 nm plasmonic layer}$$

doi:10.6342/NTU201700804

$$\Delta\phi = 475n - 637 \text{ for SiSPR with 44 nm plasmonic layer}$$

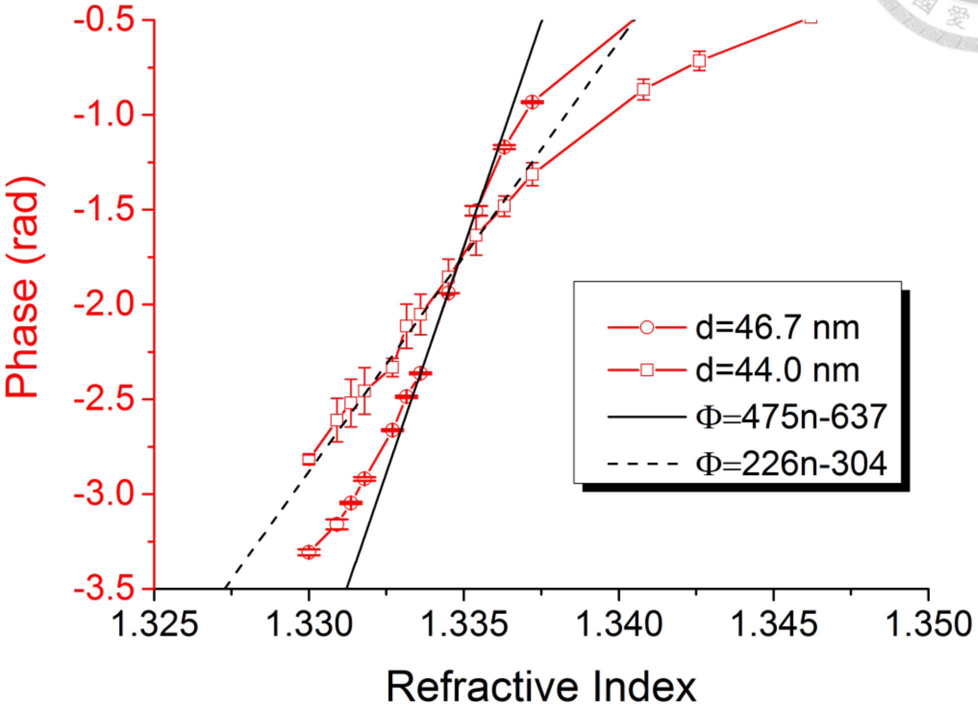

Fig. 49 P-S phase response vs refractive index

The noise of the phase noise for our measurement is typically around 0.0002 rad over a period of 150 seconds. We have therefore obtain theΔn_{min} for SiSPR chip around 2.1 x10^{-6} RIU at 44 nm and 1.2x10^{-6} RIU at 47 nm. And the linear range for the SiSPR chip is 0.0072 RIU for 44 nm of SiSPR chip and 0.0018 RIU for chip with nominal thickness of 47 nm.

The result, which indicate sharper phase response with increasing plasmonic film thickness, is as predicted from simulation based the matlab code mentioned in **Section.8-5** which is made to calculate the reflectivity of an arbitrary multilayer stack with varying

doi:10.6342/NTU201700804

surface refractive index (to simulate the reference solutions), from the knowledge of the thicknesses of the materials and the Fresnel coefficients (determined by the complex refractive indices). In the simulation, SiSPR chip is consit of a reflective layer of 2 nm ZnO with the plasmonic layer thickness ranging between 44 to 49 nm. The wavelength is 850 nm. The coupling prism is BK-7 (n=1.514). The refractive index for ZnO is 1.9540, and it is 0.1649+5.374i for the gold layer. The simulation reveals the effect of changing refractive index from 1.3315 to 1.330 with different plasmonic film thickness, as shown in **Fig. 50**. As indicated by the simulation, the slope of the phase response increase dramatically with increasing plasmonic layer thickness. Judging on the dynamic range and the sensitivity of the film, as compared to the simulation results, we consider that there are further spaces for greatly improve the sensitivity of the chip.

We now proceed to discuss this $\Delta\phi_{min}$ and the corresponding Δn_{min}. In present context, Δn_{min} is defined as the limit of detection of the system. Therefore, noise of the system is firstly determined from standard deviation of a static measurement. The “static measurement” is made when SiSPR chip is placed in background solution for a lone period of time without any perturbation in microfluidic channel. The noise in P-S phasogram is determined from a data with 300 seconds of measurement and with 3000 points of data. In case of 47 nm of plasmonic layer, where the slope of phase response is sharpest, we have measured a noise is around 2 x10^{-4} radian. The phase noise level is around 2 times smaller as compared to literature, which may be attributed to the monolithic design in combination with the performance of generalized Lock-in Amplifier.

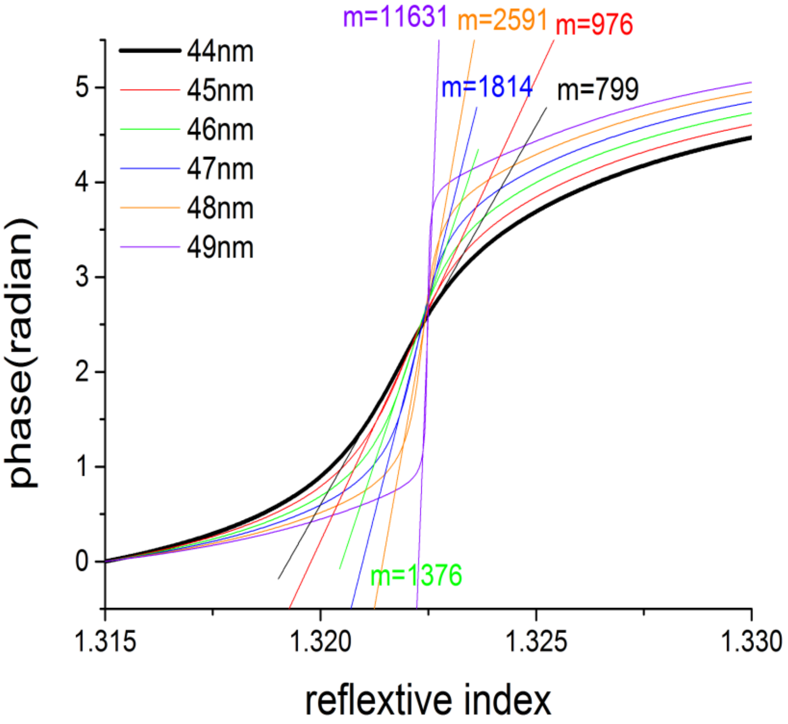

Fig. 50 Simulation on SiSPR phase response upon different refractive index. The color of the trace marks the phase response of SiSPR at different incident angle as marked in the legend.

In context of metrology, the minimally detectable signal, i.e the limit of detection, have to be at least 3 times the size of the noise to be regarded as statistical meaningful signal. Since $\Delta\phi/\Delta n$=475 rad/ RIU, we therefore conclude, for P-S phase detection, that

$$\Delta n_{min} = \frac{1}{475}\frac{RIU}{rad} \times 0.0006\, rad = 1.26 \times 10^{-6}\, RIU$$

Same calculation is performed on amplitude response of the SiSPR chip, based on the **Fig. *51***, to evaluate the claimed sensitivity advantage of phase measurement against amplitude measurement. Based on the estimated noise and the slope ($\frac{\Delta R}{\Delta n} = 207$ for

SiSPR with 47 nm thickness), we conclude that the Δn_{min} for the amplitude measurement is

$$\Delta n_{min} = \frac{1}{207}\frac{RIU}{rad} \times 0.0045\, rad = 2.1 \times 10^{-5}\, RIU$$

Therefore, we have come to a first conclusion that, using SiSPR setup, phase measurement provides a 17 times better resolution as compared to amplitude based measurement. Since that P/S amplitude sensogram and P-S phasogram is obtained by entirely identical system and signal processing method, we consider this comparison provides a rather fair ground. We would like also to discuss the implication of the interesting data above. As shown earlier, despite the nominal 47 nm design, our chip still has less $\Delta\phi/\Delta n$ slope as compared to the simulation results. According to the simulation,

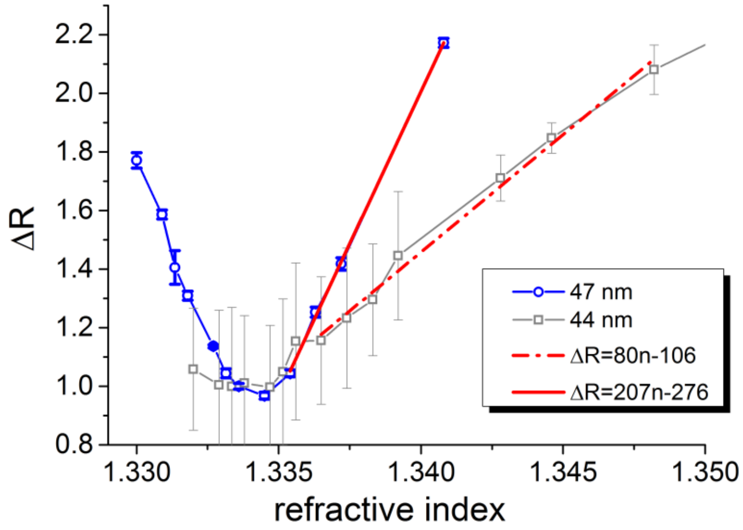

Fig. 51 SiSPR P/S amplitude response vs refractive index.
The P/S amplitude response as well as the noise, are normalized by the intensity of the reflective dip for comparison of between chips.

doi:10.6342/NTU201700804

if we increase plasmonic layer thickness to 49 nm, the simulation result suggest a slope of 11631 rad/RIU which is 24 times greater than what we have measured herein. If such chip is feasible, through annealing or precise control of film thickness, we would have achieved a SiSPR chip with much higher sensitivity if noise remain at the same level. It would also be interesting to see what is the maximum sensitivity advantage that phase measurement offers over amplitude detection.

Effect of P-S different interferometry and temperature drift effect

In case of SiSPR, due to the use of low tunability source with long OPD chip, the temperature drift of the laser emission wavelength require special attention in order to achieve a stable measurement results. **Fig.** ***52*** , which demonstrates the difference of P-S and p-ploarized phasogram, is presented to indicate the importance of the differential phasogram. In this figure, glucose sensing between 0-2.5% is conducted with a concentration steps of 0.25%, 0.5%, 0.75%, 1%, 1.5%, 1.75%, 2% and 2.5%. As can be seen in this typical case, P-S phasogram (red trace) offers a sharp and distinct phase transition upon refractive index change, while we observe trends of baseline shifting as well as noise with abrupt changes when only p phasogram is considered.

The drift is prominent in p-polarized phasogram since the temperature induced wavelength drift is not negligible in case of SiSPR. The VCSEL, in present work, has

doi:10.6342/NTU201700804

temperature dependence of lasing wavelength ($\Delta\lambda(T)$) is 0.06 nm/K[i] and a current dependence of lasing wavelength of (S) of 0.6 nm/mA. In SiSPR phase extraction process, we have a sinusoidal wavelength modulation amplitude of 0.34 nm[j]. In other words, it would lead to a 0.68 radian of phase drift if there exist only a 1 degree temperature perturbation in laboratory environment. It is therefore strongly required to has differential interferometry set-up to taken out this temperature drift effect.

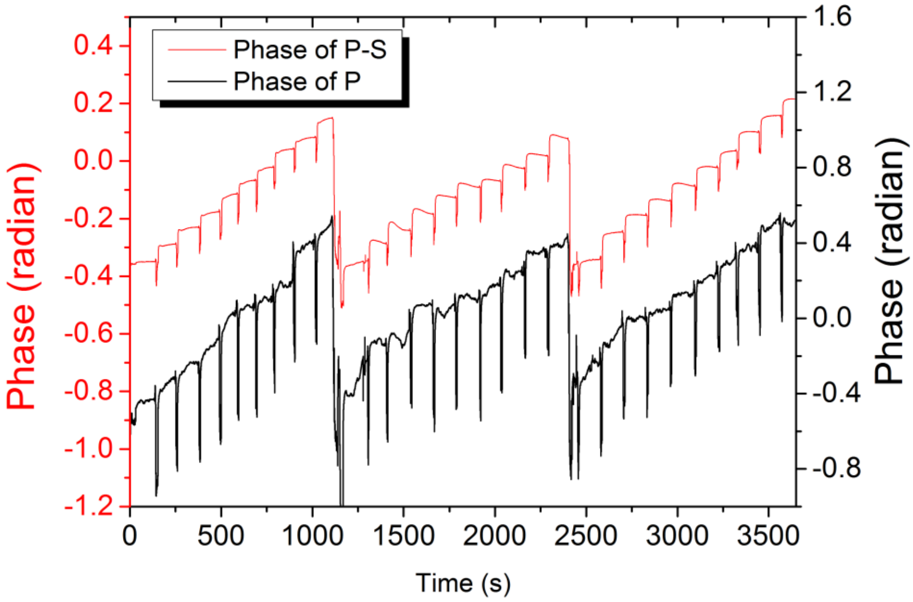

Fig. 52 P-S phasogram and P polarized phasogram in detection of different glucose solution.

Aside from temperature, differential phasogram also help to ease strain induced chip deformation when micro-fluidic channel is performing withdraw/forward action. This strain lead to phase drift (most frequently in forms of spikes), presumably due to change

---

[i] As can be found in the spec. of the VCSEL.

[j] Corresponding to $\Delta\phi_a$ of 3.8317, induced by a Δi of 0.56 mA.

doi:10.6342/NTU201700804

in optical path length when chip is deformed under fluidic pressure, which can be clearly observed with an IR camera by looking at the fringes when withdrawing solution from the microfluidic channel. Again, this kind of strain induced spikes, are presented equally in S polarization and P polarization, and can therefore be simply canceled out by extracting the P-S phase. The same idea applies to P/S amplitude information as compared to the only P amplitude information, where changes in the optical source amplitude are compensated by performing the ratio of the two amplitudes.

In brief, the P-S differential phasogram is strongly suggested in SiSPR measurement due to unique design of the phase extraction process. However, the readers should note that a temperature PID controller might still offer further stabilization in the near future, since P-S phasogram cannot exclude the temperature effect on the refractive index of aqueous solution despite this effect is undesirable.

Section 9-5. Preliminary bio-sensing Data

In this section, we demonstrate the preliminary result of biosensing using SiSPR sensor chip. To begin with, Tro4 aptamer[42] is modified SiSPR chips and the reactions are monitored via the P-S phasogram. We will use diffusion limited Langmuir model to have a closer look at the surface modification condition. Finally, we will introduce our preliminary results on the cardiac troponin I detection.

"Aptamer" refers to a short strand DNA that has a functionality of antibody to a specific

doi:10.6342/NTU201700804

protein. Due to the room temperature stability, ease of synthesis and the potential for further chemical structure amendment, aptamer has been widely applied as probe molecule in detection of Platelet-Derived Growth Factor (PDGF)[25], interferon gamma for Tuberculosis screening[16] and human chorionic gonadotropin detection[15].

In 2015, Hunho Jo et. al.[42] has reported a series of Aptamer obtained by "Systematic Evolution of Ligands by Exponential enrichment" (SELEX)[43] for detection of Cardia Troponin I (cTnI). cTnI is considered as a gold standard biomarker for screening of Acute Myocardial Infraction (AMI)[44]. Based on report from Hunho Jo et. al., they have reported a "Tro4" 40 mer aptamer sequence that has a dissociation constant (K_d) of 270 pM for cTnI monomer and has a Kd of 3.10 nM even for Troponin Complex. In the reported electrochemical sensing experiment, the aptamer can reach a limit of detection around 1 pM (S/N=3), which is lower than clinical cut-off value of 70-400 pg/mL. This suggest a high clinical value of such screening in case of AMI. Since AMI is an indication that suits the targeted application of the portable diagnostics, surface modification of Tro4 aptamer for cTnI detection is selected as a demonstration of bio-sensing efficacy in present work.

The sequence of the Tro4 is 5'-TTT TTT CGT GCA GTA CGC CAA CCT TTC TCA TGC GCT GCC CCT CTT A-3' (46 mer). The synthesis of the sequence is carried out by Purigo™ in Taiwan. The 5' end of the Tro4 aptamer is modified with a thiol functional group for reaction with SiSPR gold surface. The running buffer for the sensing process is

doi:10.6342/NTU201700804

1X TE buffer (10 mM Tris + 1 mM EDTA from Protech Technology Enterprise) with 1 M of NaCl. Thiolated Tro4 is firstly mixed with 20 mM of TCEP (Tris(2-Carboxyethyl)phosphine hydrochloride) for reduction of disulfide bond. The purpose of the reduction is to confer consistent surface modification efficiency and it typical stand for more than one hour.

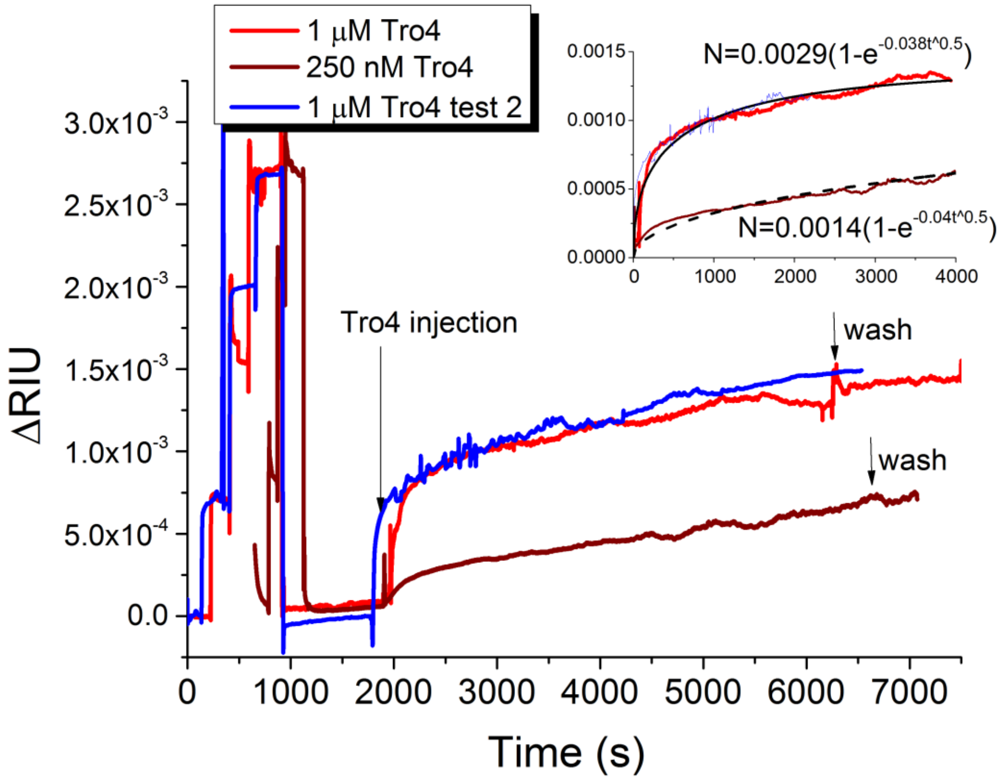

Fig. 53 Tro4 Aptamer surface modification
A calibration is first carried out with four reference solutions, followed in influx of Tro4 aptamer. After ~4000 seconds of surface modification, running buffer is flowed again to take confirm the binding of the aptamer.

As shown in **Fig. 53**, before surface modification, a calibration step curve is firstly established by four reference solutions. The calibration step starts with running buffer as baseline, followed by 0.5 % glucose solution, 1 % glucose solution and 1.5 % glucose

doi:10.6342/NTU201700804

solution respectively[k]. The existence of calibration steps helps to transfer phase information into refractive index unit and allows fair comparison of surface modification performance between different chips. After calibration steps, running buffer is used again to re-establish the baseline. The First black arrow in the graph indicates the influx of the Tro4 aptameric probe. The brown trace indicates the inflow of 250 nM Tro4 DNA while the red and blue trace indicate the influx of 1 μM sample. Finally, running buffer is flown again to cast away the non-specifically bound aptamer as well as to confirm the stringency of probe binding to the plasmonic layer. By blue and red trace, we can see that the modification results are reproducible between different chip trial run.

There are some points that worth discussion before we continue to explore the cTnI detection results. First, judging on papers from Peterlinz et. al.[45] and from Peterson et. al. [46], Δn for ssDNA modification is on order of 10^{-3}~10^{-2} RIU[l], which correspond to our results here. To be more specific, Peterlinz et. al. conducted the surface modification of 25 mer DNA in 1 M KH2PO4 (pH~3) while Peterson et. al. concluded that 1 M KH2PO4 has more less the same surface modification performance as TE buffer with 1 M NaCl. Therefore, we can say that, in terms of surface chemistry, we have similar condition as the work from Peterlinz. Under condition mentioned above, Peterlinz's surface modification lead to a Δn of 0.0052 RIU for thiolated ssDNA. Considering the fact that

---

[k] Glucose reference solutions are prepared in TE running buffer background

[l] Assuming that DNA has similar refractive index between 650 nm and 850 nm.

doi:10.6342/NTU201700804

Tro4 aptamer that we use herein has 46 codon, which should have 1.84 times more refractive index change as compared to the sequence used by Peterlinz et. al., $\Delta \mathrm{n}$ for our case should be somewhere below 0.00968 . To further analyze surface modification data, we have conducted a curve fitting using diffusion limited Langmuir model:

$$\Delta \mathrm{n} = n_{max}(1 - e^{-kt^{\frac{1}{2}}})$$

The results is shown in the inset of **Fig. 53**. The fitting indicates that for surface modification of Tro4 with 2 μM concentration, the fitting gives:

$$\Delta \mathrm{n} = 0.0029(1 - e^{-0.038t^{\frac{1}{2}}}) \text{ with } \mathrm{R}^2 \text{ of } 0.96$$

And for Tro4 modification with 250 nM, the fitting gives

$$\Delta \mathrm{n} = 0.0014(1 - e^{-0.040t^{\frac{1}{2}}}) \text{ with } \mathrm{R}^2 \text{ of } 0.96$$

For both cases, the maximum amount of surface modification (n_{max}) is smaller than 0.00968. The difference may partly due to the stem-loop structure [42]of the Tro4 aptamer which requires more free space for ease of steric effect.

Fig. 54 black trace demonstrates the results for cTnI detection using SiSPR sensor chips. As in case of Tro4 Modification, a calibration step is flown for transferring phase information into refractive index unit. The running buffer of cTnI is 1X TE buffer with 150 mM of NaCl. As indicated in the insets, the prominent sensing signal is revealed at 120 nM of cTnI concentration. Considering the fact that molecular weight of cTnI is

doi:10.6342/NTU201700804

similar to Tro4 aptamer[m], we can directly use $\Delta \mathrm{n}_{cTnI}$ vs $\Delta \mathrm{n}_{Tro4}$ to calculate the binding efficiency. Based on the fact $\Delta \mathrm{n}_{Tro4}$ (the red trace in the figure) is 0.001375 when 5000 s of surface modification is done and $\Delta \mathrm{n}_{cTnI}$ is around 0.0001 as shown in the inset, we conclude that that There is around 7% of surface Tro4 bound of cTnI at 120 nM. This value is much lower judging from the reported 270 pM K_D[42]. With a dissociation constant of 270 pM, based on chemical kinect, we can derive that:

$$270\, pM = \frac{[A] \times 120nM}{[AB]}$$

Where $[AB]$ is the cTnI bound Tro4 and [A] is the free Tro4. As results, we know that

$$\frac{[A]}{[AB]} = \frac{270\, pM}{120\, nM} = 0.225\ \%$$

In other words, 99.78 % of Tro4 should be complex with cTnI as compared to what we have measured. We considered that the difference in binding performance is due to buffer background. In the reports from Jo. et. al.[42], they uses PBS with 10 mM of NaCl, 5 mM of KCl and 1 mM of $MgCl_2$. Apparently, the Tro4 in such condition has much more effective charge (longer Debye length). Moreover, Tro4 would have more stable secondary structure due to the presence of Magnesium ion and lack of EDTA. Therefore, in the future work, we would substantial change the buffer background to reach the maximum performance of the sensor.

---

[m] cTnI molecular weight is around 24 kDa. The DNA has around 500 D on average for a single base pair. In other words, Tro4 has a molecular weight of 46*500~23 kDa.

doi:10.6342/NTU201700804

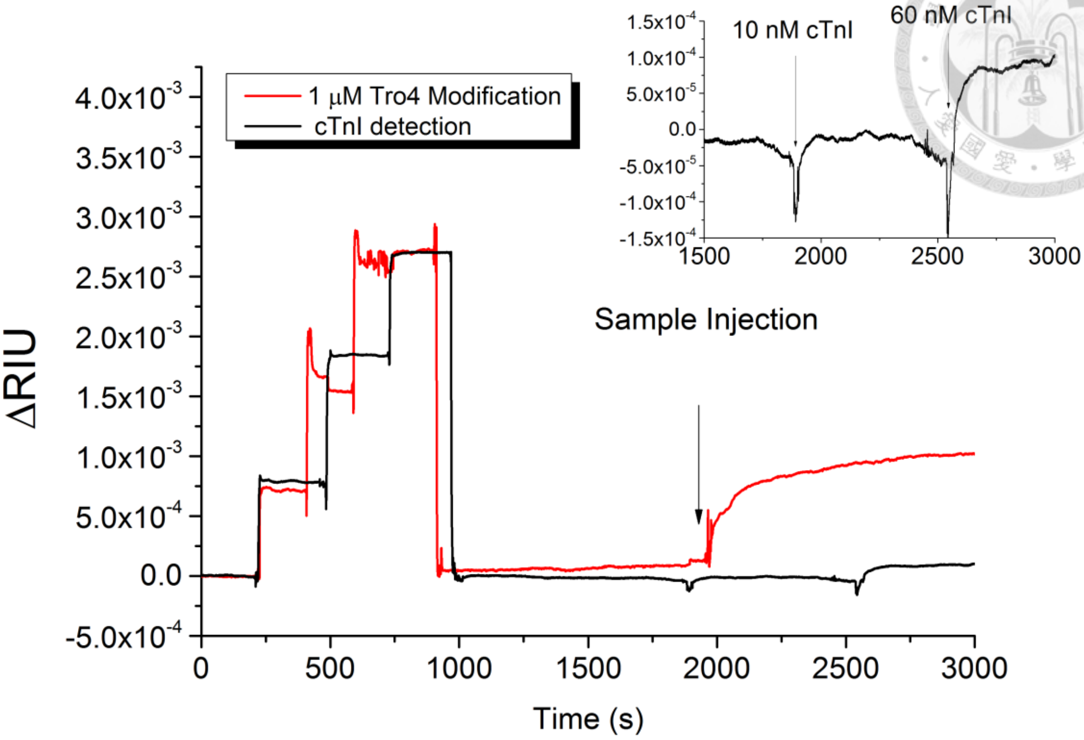

Fig. 54 SiSPR cTnI detection

Section 9-6. Summary and conclusion on SiSPR

In this second part of the thesis, we have demonstrated novel SiSPR biosensor device from working principle, theoretical derivation, the analysis of detection limit and provided some preliminary sensing result. Through the demonstration, we have shown a novel SPR device that allows phase sensitive measurement to be carried out on conventional Kretschmann configuration down to 10^{-6} RIU. SiSPR combines the advantage of amplitude based SPR measurement with the sensitivity from phase sensitive SPR.

The double layer design of the SiSPR allows interference fringes to be generated without the need for extra beam splitters or mirrors. This monolithic design is also less sensitive to environment vibrational noise. Using current-induced phase modulation, we avoid the use of expensive phase modulator such as AOM, piezo-actuators or PEM, that are key components for phase extraction method but too costly and bulky for really portable application.

To extract the phase information from a current- induced phase modulation, we have devised a new phase extraction method. Such method is modified from our previous report of generalized Lock-In amplifier. The newly devised phase extraction tackles the issue of phase extraction when a large amplitude modulation is present at the same frequency than the phase modulation. Such issue, in case of monolithic homodyne interferometer, has not been addressed in literature. The proposed method can extract phase from $-\pi$ to π full range, provided that the phase modulation depth $\Delta\phi_a$ is around 3.8317 rad. We have revealed that $\Delta\phi_a$ is linearly dependence on Δi within desired working range. The precision of the $\Delta\phi_a$ calculation depends on precision of S value for VCSEL. Therefore, a glass slide based shearing interferometer was built to verify S and $\Delta\phi_a$.

Through a series of sensing experiment on glucose solution, we have demonstrate that the SiSPR has a Δn_{min} on order of 10^{-6} RIU, which is the same as reported in other phase sensitive SPR, despite not to the very limit of it (~10^{-7} RIU). Through the phasogram, we

doi:10.6342/NTU201700804

have also demonstrated why differential interferometry is crucial for stable measurement of SiSPR. Judging on the phase response of SiSPR, we came to conclusion that SiSPR can be more sensitive than its amplitude measuring counterpart at 47 nm of plasmonic layer. It would be one of our future goal to see if it provide more sensitivity advantage when film thickness reach ideal value.

Before the end of chapter 9, we have also demonstrated a preliminary surface modification results for Tro4 aptamer with different surface modification condition. In static non-flowing surface modification process, Tro4 aptameric probe lead to ~$3x10^{-3}$ RIU changes. It seems that initial aptameric concentration may help to control the surface probe density. A cardiac Troponin I sensing experiment is conducted to reveal the efficacy of biosensing using SiSPR. Preliminary results indicates a 60 nM cTnI detection is possible with SiSPR. We believe that buffer composition may greatly improve the sensing limit, judging from the literature review. As a last remark, we point out that the more technical aspects regarding the integration of the portable prototype can be found in the appendix (sections A3-A5).

doi:10.6342/NTU201700804

Chapter 10. General conclusion and future perspectives

Through this dissertation, we have demonstrated the implementation of plasmonic sensor chip with smartphone devices, with special attention on interferometry and different types of digital LIA. In the first part, from chapter 1 to chapter 5, we have revealed use of smartphone platform as User Interface , opto-electric circuitry driver and as a powerful digital processor. The product of the efforts is a smartphone based digital LIA based AuNP colorimetry DNA sensor, which provide 0.77 nM of detection limit within 15 minutes of waiting time.

With the experience in first integration, we proceed to integrate more advanced interferometric plasmonic devices with smartphone. The major difficulties of the integration lies in the optical configuration of homodyne which need to be adapted to POC environment. We have therefore proposed SiSPR as solution of the issue. In SiSPR, phase modulator is done by wavelength modulation using low tunability source. To reduce number of optical pieces, we have adapted shearing interferometry design to the SPR sensor chip. To extract the phase, where amplitude is strongly modulating with phase term at the same frequency, a novel phase extraction method is proposed. In results, SiSPR demonstrate 20 times superior sensitivity and the capacity to suppress vibrational noise right on top of conventional Kretschmann configuration. At the moment, SiSPR reaches a detection limit of 1.26x10^{-6} RIU at 47 nm plasmonic layer thickness. We believe

doi:10.6342/NTU201700804

that SiSPR may provide more sensitivity advantages with optimized layer thickness, based empirical data and simulation. To the best of our knowledge, SiSPR is not reported to any literature up to the moment. Before the end of thesis, we have demonstrated preliminary results on biosensing using SiSPR. The attempt is not just to showcasing the performance but also to build protocol of DNA aptamer probe modification and detection. Considering the scope and conciseness of the dissertation, SiSPR integration with smartphone platform is not detailed in the main body of the work. The readers are encouraged to find more discussion in appendix, where an android-Arduino driven SiSPR platform is proposed. Also, readers may find an extended French abstract in the end of the dissertation as a remark of French-Taiwan joint efforts on this dissertation.

From our point of view, the combination of phase sensitive plasmonic chip with portable platform has opened up many possibilities, as well as un-solved questions, that will be the target of pursue in near future.

“Sensitivity” of SiSPR is among many interesting issues that deserves attention and further research efforts. We have indeed preliminarily addressed the sensitivity of SiSPR in terms of minimally detectable refractive index which is $1.26\text{x}10^{-6}$RIU. However, from bio-medical point of view, the superior of sensitivity has to be put in context of diagnostic, to have an indication[n], to validate its value. Consequently, we propose here two possible

---

[n] By the word “Indication”, the author refers to the reason to use a certain diagnostic tool, curing strategy in a specific symptom. Although this term is widely used in biomedical field, it is noted here for the

doi:10.6342/NTU201700804

research direction and some insights on SiSPR's sensitivity. First, when amplification reaction is considered, superior sensitivity lead to fasted on-set time and reduced miscellaneous amplificon due to prolonged reaction time. In this perspective, we believe that Hybridization Chain Reaction (HCR) from Roberts M. Dirks et. al.[47] may serve a good method to combine with SiSPR. The combination may lead to iso-thermal detection of ultra-low target concentration with reduced diagnostic time. In another perspective, it would also be interesting to compare the sensitivity of SiSPR with market/clinically approved ELISA kits. While SPR has advantages in real-time detection without the need for molecular tagging, ELISA remains to be one of the most commonly used tool for study of bio-chemical reaction or clinical diagnostic tool. Sensitivity is among one of the issue to be resolved. Several past literatures[48, 49] has indicated that ELISA has sensitivity advantages over conventional amplitude based SPR by a factor of 10~100. For example, Lofgren et. al. has indicated that, in sensing of anti-panitumumab Ab, ELISA has a detection limit of 10 ng/mL while a commercially SPR can reach only 1 μg/mL. With 20 times more sensitivity, SiSPR may provide the same sensitivity as that of ELISA while offering real-time and label-free advantages.

Asides from sensitivity, we foresee the need for imaging base SiSPR. As is well-known, multi-target sensing panel very often improves detection sensitivity, selectivity and

---

diverse range of reader that are potentially interested to this dissertation.

doi:10.6342/NTU201700804

provide many complementary information thereby making SPR a more powerful device. For example, in case of Tuberculosis rapid detection[28], sensing panel composed of endotoxin and surface protein provide an alternative choose asides from conventional blood smear test. To this end, two technical barrier need to be addressed. To begin with, we need to provide a stringent multi-probe modification method. This is one of the under developing technology that we have been working on. Our proposition is to use thiol-ene click chemistry together with a UV exposure system, instead of conventional thiol-gold or amine chemistry, to achieve spatial selective surface modification. Briefly, the SiSPR chip is coated, via Chemical Vapor Deposition (CVD)[o], with functional polymer with vinyl group for later on thiol-ene reaction. When designated probe DNA molecule, which has a thiol at 5’ end, reaches surface, specific UV pattern is exposed onto the chip surface to define the location for surface modification. Such patterning can be achieved with

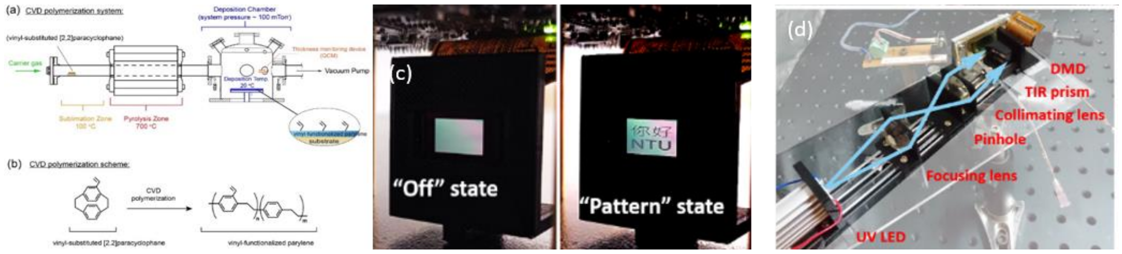

Fig. 55 (a) CVD system for deposition of polymer (b) DMD pattern control (c) preliminary exposure system.

---

[o] The system, as well as the image of CVD system in **Fig. 55**, are provided by prof. Hsien-Yeh Chen from Biointerface Engineering Laboratory NTU

Digitla Mirror Device (DMD). Asides from the being spatial selective, such method also largely reduce non-specific binding due to the thickly coated SiSPR chip.

Another technical barrier, for such multi-target screening process, is the need to develop an imaging SiSPR. In case of phase imaging, “frame rate” of the phase image is of major concern. The frame rate of phase imaging is typically low, for example it may take seconds to obtain one phase image. The reason is mainly due to the large number of pixels , each requires Fourier transformation or so, which bring heavy calculation. Proper algorithm need to be proposed for imaging based SiSPR which provides good phase extraction results while maintaining sufficient time resolution.

doi:10.6342/NTU201700804

Appendix

doi:10.6342/NTU201700804

Section A1. List of mathematical relations

There are few mathematical relations that we use repeatedly in the derivation of phase extraction method. They are listed below, although some of them are very well-known and basics, in order to follow the derivation more smoothly.

***Jacobi-Anger expansion*:**

Jacoby-Anger expansion can be used to express signal like $cos(asin(\omega t))$ and $sin(asin(\omega t))$ as an infinite sum of harmonics. Jacobi-Anger expansion states that:

$$cos(asin(\omega t)) = J_0(a) + 2\sum_{n=1}^{N} J_{2n}(a)cos(2n\omega t) \quad A.\ 1$$

$$sin(asin(\omega t)) = 2\sum_{n=1}^{N} J_{2n-1}(a)\, sin\big((2n-1)\omega t\big) \quad A.\ 2$$

Where $J_n(a)$ is the Bessel function of the first kind.

Trigonometric sum-to-product and product-to-sum relationships

$$cos(a+b) = cos(a)\, cos(b) - sin(a)\, sin(b) \quad A.\ 3$$

$$cos(a)cos(b) = \frac{1}{2}(cos(a+b) + cos(a-b)) \quad A.\ 4$$

$$sin(a)sin(b) = \frac{1}{2}(cos(a-b) - cos(a+b) \quad A.\ 5$$

Integration of trigonometric function

Due to their symmetry, the integration of the basic trigonometric functions over multiple of complete periods gives a sum of zero, i.e:

$$\int_0^{2K\pi} cos(t)\, dt = \int_0^{2K\pi} sin(t)\, dt = 0 \; A.\ 6$$

doi:10.6342/NTU201700804

Section A2. Detail in phase extraction

In this section, we provide a more detailed derivation of SiSPR phase extraction method.

In section 8-3-2, we know that I_{det-1} and I_{det-2} and we know the Rx and Ry for part 1 from our previous report on generalized Lock-In

$$R_{X-part1} = \frac{1}{2} cos\phi m I_0 (1 + J_0(2a) - 2J_0(a)^2) A.\ 7$$

$$R_{y-part1} = \frac{1}{2} sin\phi m I_0 \big(1 - J_0(2a)\big) A.\ 8$$

Now we can proceed to study the R$_x$ from $I_{\widetilde{det-part2}}$. First, for ①:

$$R_X = \frac{1}{2\pi}\int_0^{2\pi} m\mu sin(\omega t)[J_0(\Delta\phi_a) + 2\sum_{n=1}^{N} J_{2n}(\Delta\phi_a)\, cos(2n\omega t)]dt\ A.\ 9$$

R$_X$ for ① gives zero. R$_X$ for ② gives:

$$R_X = \frac{1}{2\pi}\int_0^{2\pi} m\mu cos\phi\, J_0(a) sin(\omega t)[J_0(\Delta\phi_a) + 2\sum_{n=1}^{N} J_{2n}(\Delta\phi_a)\, cos(2n\omega t)]dt\ \ A.\ 10$$

Again, R$_X$ for ② is zero. R$_X$ fo r③ gives:

$$R_X = \frac{1}{2\pi}\int_0^{2\pi} m\mu cos\phi\ sin(\omega t)[2\sum_{n=1}^{N} J_{2n}(\Delta\phi_a)\, cos(2n\omega t)]\ [J_0(\Delta\phi_a) + 2\sum_{n=1}^{N} J_{2n}(\Delta\phi_a)\, cos(2n\omega t)]dt\ \ A.\ 11$$

The term in the integrand proportional to sin(ωt) gives zero. We can further simplify the signal as:

$$R_X = \frac{1}{2\pi}\int_0^{2\pi} 4m\mu cos\phi sin(\omega t)[\sum_{n=1}^{N} J_{2n}(\Delta\phi_a)\, cos(2n\omega t)]\ [\sum_{n=1}^{N} J_{2n}(\Delta\phi_a)\, cos(2n\omega t)]dt\ \ A.\ 12$$

Since $\cos(a)\sin(b) = \frac{1}{2}(\sin(a+b) + \sin(b-a))$, we find that Rx for ③ is again

doi:10.6342/NTU201700804

zero. Now we can derive Rx for ④:

$$R_X = \frac{1}{2\pi}\int_0^{2\pi} m\mu sin\phi\, J_1(\Delta\phi_a) sin(\omega t) sin(\omega t)[J_0(a) +$$

$$2\sum_{n=1}^{N} J_{2n}(\Delta\phi_a)\, cos(2n\omega t)]dt \quad A.\ 13$$

$$R_X = \frac{1}{2\pi}\int_0^{2\pi} \frac{1}{2} m\mu sin\phi\, J_1(\Delta\phi_a)(1 - cos(2\omega t)\, [J_0(a) +$$

$$2\sum_{n=1}^{N} J_{2n}(\Delta\phi_a)\, cos(2n\omega t)]dt$$

A. 14

So that:

$$R_X = \frac{1}{2} m\mu sin\phi J_1(\Delta\phi_a) J_0(\Delta\phi_a) -$$

$$\frac{1}{2\pi}\int_0^{2\pi} \begin{array}{c} \frac{1}{2} m\mu sin\phi\, J_1(\Delta\phi_a) cos(2\omega t) \\ * \, [2J_2(\Delta\phi_a) cos\omega t + 2\sum_{n=2}^{N} J_{2n}(\Delta\phi_a)\, cos(2n\omega t)]dt \end{array} \quad A.\ 15$$

and

$$R_X = \frac{1}{2} m\mu sin\phi J_1(\Delta\phi_a) J_0(\Delta\phi_a) - \frac{1}{2\pi}\int_0^{2\pi} [\frac{1}{2} m\mu sin\phi \Delta\phi_a J_2(\Delta\phi_a)[1 + \frac{1}{2} cos(4\omega t)] +$$

$$m\mu sin\phi J_1(\Delta\phi_a) J_2(\Delta\phi_a) cos(2\omega t) \sum_{n=2}^{N} J_{2n}(a)\, cos(2n\omega t)]dt \quad A.\ 16$$

As a result, Rx for ④ $= \frac{1}{2} m\mu sin\phi J_1(\Delta\phi_a) J_0(\Delta\phi_a) - \frac{1}{2} m\mu sin\phi J_1(\Delta\phi_a) J_2(\Delta\phi_a)$

Rx for ⑥:

$$R_X = -\frac{1}{2\pi}\int_0^{2\pi} \frac{1}{2} m\mu sin\phi J_1(\Delta\phi_a)[J_0(\Delta\phi_a) + 2\sum_{n=1}^{N} J_{2n}(\Delta\phi_a) \cos(2n\omega t)]dt$$

$$Rx = -\frac{1}{2} m\mu sin\phi J_1(\Delta\phi_a) J_0(\Delta\phi_a) A.\ 17$$

Rx for ⑤

$$R_X = -\frac{1}{2\pi} m\mu sin\phi \int_0^{2\pi} sin(\omega t)[2\sum_{n=2}^{N} J_{2n-1}(\Delta\phi_a) \sin((2n-1)\omega t)][J_0(\Delta\phi_a)$$

$$+ 2\sum_{n=1}^{N} J_{2n}(\Delta\phi_a) \cos(2n\omega t)]dt$$

doi:10.6342/NTU201700804

And therefore we have the result for R_X and R_Y

doi:10.6342/NTU201700804

Section A3. Matlab code for simulation of SPR performances

```
function []=A_vs_P()
% to estimate the advantage of phase measurmeent
% in SPR
% reflection as a function of angle
% based on transfermatrix3
% TransferMatrix3 calculates transmission, reflection and absorption
of a multilayer of planar homogenous films
% inputs:
% angle of incidence: thetai
% wavelength of incident light: lambda
% thicknesses of the layers: h
% refractive index of the layers: n (may be absorbing and dispersive,
but this may require a subfunction)
%  polarization: s or p (need one calculation for each for unpolarized
light)

clear all;%close all
LW=1.5;%linewidth
%close all
% edit untitled
load matnormal
L=850;%close all
n_end=1.330;
n_Au=sqrt(Au(L))
n1=1.514;  %BK7
nZinc_Oxide=1.9540;
nCr=4.12+4.14i;
thetai=[60:0.005:72]; %angle of incidence (degrees)
%lambda=670; %vacuum wavelength (nm)
h=[NaN,2,44,NaN]; %film thicknesses in nm, equal in length
                 %to n, start and end with NaN
pol=1; %polarization, 1 for p and 0 for s
; %refractive index data, NaN for frequency dependence


for a=1:length(thetai)
```

doi:10.6342/NTU201700804

```
[r(a),FR(a),FT(a),FA(a)]=Fresnel(L,thetai(a),h,[n1,nZinc_Oxide,
n_Au,n_end],pol);
end



%plot results:
figure
%subplot(2,1,1)
 hold on
% plot(L,FT,'b')
% plot(L,FR,'r')
% plot(L,FA,'g')
% plot(L,L*0,':')
% plot(thetai,FT,'b')
 norm=2*pi;%(2*pi)
 h1=plot(thetai,FR,'r')
 h2=plot(thetai,(angle(r)+pi)/(norm),'g:')
 U=unwrap(angle(r));Un=(U-min(U))/norm;
 h3=plot(thetai,Un,'g')
 plot(thetai,L*0,':')
 %h1=h2
 Angle_out=thetai.';
 FR_out=FR.';
 Un_Out=Un.';
 Out=[Angle_out, FR_out, Un_Out]
 xlswrite('d:\850nm_44nmAu_2nmZnO_water.xls',Out, 'sheet1')


 set([h1,h2,h3],'linewidth',LW)




xlim([thetai(1),thetai(end)])
%ylim([min([FA FR FT 0]) max([1 FA FR FT])])

set([gca],'color',[1 1 1])
% hl=legend('R','Phase', 'unwrapped')
```

doi:10.6342/NTU201700804

```
% set(hl,'Edgecolor',[1 1 1],'fontsize',6)

% xlabel('Angle (nm)')
% ylabel('Fresnel coefficient')
% ht=title(['Thickness=' num2str(h)])

% % subplot(2,1,2)
% % plot(L,real(n),'g');hold on
% % plot(L,imag(n),'x'),
% % plot(L,L*0,':')
% % legend('real(n)','imag(n)')
 set([gca],'color',[0 0 0])
% % xlim([L(1),L(end)])
% % xlabel('lambda (nm)');
%


end

function [r,FR,FT,FA]=Fresnel(lambda,thetai,h,n,pol)

%Snell's law:
theta(1)=thetai*pi/180;
for a=1:length(n)-1
theta(a+1)=real(asin(n(a)/n(a+1)*sin(theta(a))))-
1i*abs(imag(asin(n(a)/n(a+1)*sin(theta(a)))));
end

%Fresnel coefficients:
if pol==0 %formulas for s polarization
for a=1:length(n)-1
Fr(a)=(n(a)*cos(theta(a))-
n(a+1)*cos(theta(a+1)))/(n(a)*cos(theta(a))+n(a+1)*cos(theta(a+1)));
Ft(a)=2*n(a)*cos(theta(a))/(n(a)*cos(theta(a))+n(a+1)*cos(theta(a+1)))
;
end
elseif pol==1 %formulas for p polarization
for a=1:length(n)-1
Fr(a)=(n(a)*cos(theta(a+1))-
```

```
n(a+1)*cos(theta(a)))/(n(a)*cos(theta(a+1))+n(a+1)*cos(theta(a)));
Ft(a)=2*n(a)*cos(theta(a))/(n(a)*cos(theta(a+1))+n(a+1)*cos(theta(a)))
;
end
end

%phase shift factors:
for a=1:length(n)-2
delta(a)=2*pi*h(a+1)/lambda*n(a+1)*cos(theta(a+1));
end

%build up transfer matrix:
M=[1,0;0,1]; %start with unity matrix
for a=1:length(n)-2
M=M*1/Ft(a)*[1,Fr(a);Fr(a),1]*[exp(-
1i*delta(a)),0;0,exp(1i*delta(a))];
end
M=M*1/Ft(length(n)-1)*[1,Fr(length(n)-1);Fr(length(n)-1),1];

%total Fresnel coefficients:
Frtot=M(2,1)/M(1,1);
Fttot=1/M(1,1);

%special case of single interface:
if length(n)==2
Frtot=Fr(1);
Fttot=Ft(1);
end

%total Fresnel coefficients in intensity:
FR=(abs(Frtot))^2;
FT=(abs(Fttot))^2*real(n(length(n))*cos(theta(length(n))))/real(n(1)*c
os(theta(1)));
FA=1-FR-FT;
r=Frtot;

end

function epsilon=Au(lambda)
```

doi:10.6342/NTU201700804

```
%analytical formula for gold based on wavelength in nm, fits J&C data:
epsiloninf=1.54;
lambdap=143;
gammap=14500;
A1=1.27;
lambda1=470;
phi1=-pi/4;
gamma1=1900;
A2=1.1;
lambda2=325;
phi2=-pi/4;
gamma2=1060;

%other parameters, worse fit to J&C but seems more accurate often:
%epsiloninf=1.53;
%lambdap=155;
%gammap=17000;
%A1=0.94;
%lambda1=468;
%phi1=-pi/4;
%gamma1=2300;
%A2=1.36;
%lambda2=331;
%phi2=-pi/4;
%gamma2=940;

for a=1:length(lambda)
epsilon(a)=epsiloninf-
1/(lambdap^2*(1/lambda(a)^2+1i/(gammap*lambda(a))))...
+A1/lambda1*(exp(phi1*1i)/(1/lambda1-1/lambda(a)-1i/gamma1)+exp(-
phi1*1i)/(1/lambda1+1/lambda(a)+1i/gamma1))...
+A2/lambda2*(exp(phi2*1i)/(1/lambda2-1/lambda(a)-1i/gamma2)+exp(-
phi2*1i)/(1/lambda2+1/lambda(a)+1i/gamma2));
end

end
```

Section A4. Design of the SiSPR portable prototype

A SiSPR portable prototype is shown in ***Fig. 56***. The portable system is comprised of three parts: an android OS system for User Interface and information collection, an Arduino (Cortext M3) for synchronized output/input as well as for performing GLIA, and one SiSPR/Microfluidic Chip set. In this laboratory prototype Arduino due is used with a 12- bits two channel ADC for reading S and P channels. A 12-bits DAC is used to drive the VCSEL laser diode. The algorithm is developed through open source Arduino Integrated Development Environment.

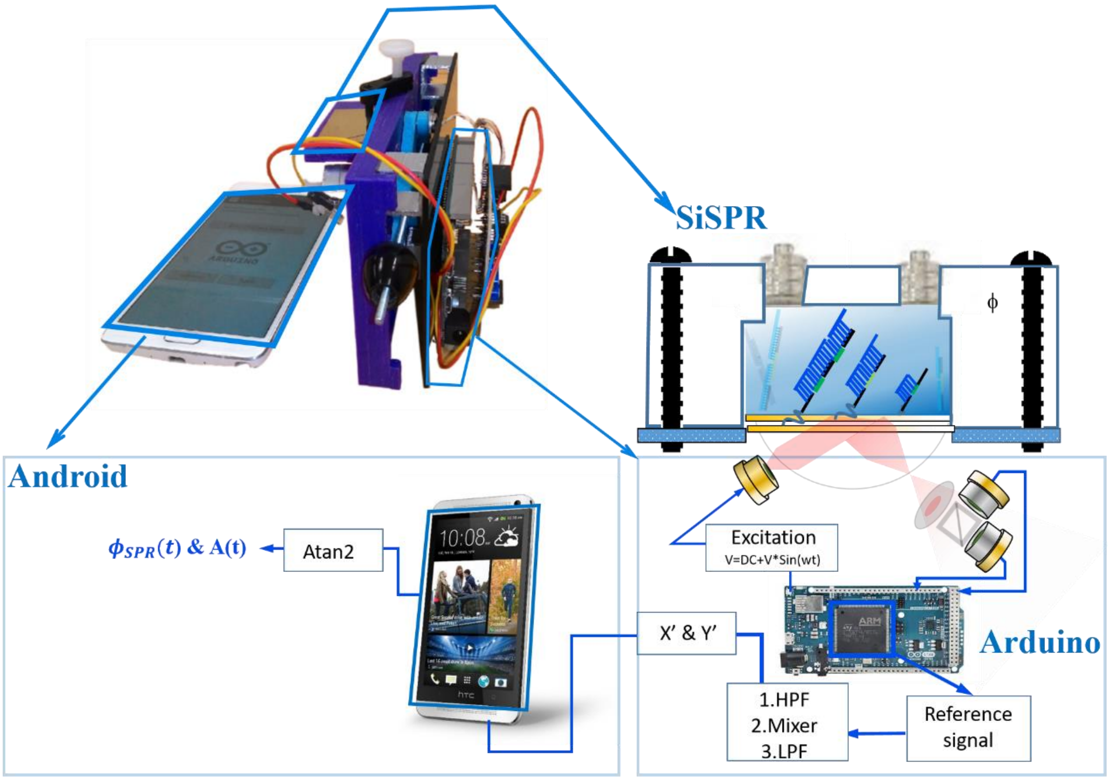

Fig. 56 SiSPR portable prototype and system structure

doi:10.6342/NTU201700804

Section A4. GLIA algorithm on Arduino

The developed Arduino algorithm is shown below:

```
void functionGen(){
    analogWrite(DAC1,(Modulation[loopIndex%N]-
    Phase_modulation_On_Off*b*0.016*(Slow_Variation_Index%20)/20));
/*Writing the signal to DAC1 for output*/
/*to calculate the phase    change corresponding to slow power modulation, we need
to know that first d(lambda)=S*di, in current case S=0.46 nm/mA, 0.11 Arudino
output correspond to 0.25 mA in case of 220 ohm load resistor.*/
    SignalS=analogRead(A8);/*Read from the S-detector*/
    SignalP=analogRead(A9);/*Read from the P-detector*/
    /*FIR-HPF*/
    dc_store_S+=SignalS;
    dc_store_P+=SignalP;
    if((loopIndex%100)==0){
        dc_component_S=(dc_store_S/100);
        dc_component_P=(dc_store_P/100);
        dc_store_S=0;
        dc_store_P=0;
    }
    FilteredS=(SignalS-dc_component_S);
    FilteredP=(SignalP-dc_component_P);

    /*End of HPF
    *Due to US of FIR filter and to safe some space don't use the data from first period
of SLIA
    */

    Xs+=(FilteredS*RefX[loopIndex%N]);/*RefX Low-Pass Filter(LPF)*/
    Ys+=(FilteredS*RefY[loopIndex%N]);
    Xp+=(FilteredP*RefX[loopIndex%N]);/*RefX Low-Pass Filter(LPF)*/
    Yp+=(FilteredP*RefY[loopIndex%N]);

    l/*Nothing in this lock-in loop should pass here. Th*/
    (loopIndex%(5*tau))==0? (Slow_Variation_Index++):(0);
    if((loopIndex%tau)==0){
        Xsout=20*Xs*SLIA_k/tau;
        Ysout=20*Ys*SLIA_k/tau;
        Xpout=20*Xp*SLIA_k/tau;
        Ypout=20*Yp*SLIA_k/tau;
        Xs=0;
        Ys=0;
        Xp=0;
        Yp=0;
    }
```

The use of Arduino grants free control on synchronizing capacity of reading at 12-bits and writing of voltage function (up to 3.3 V). However, to provide synchronized read and write capacity at micro-second level, Interrupt Service Routine (ISR) is needed in place

doi:10.6342/NTU201700804

of general loop structure as demonstrated in the code.

In the algorithm, the ISR controls all the time relevant events such as capture of data, writing of data and GLIA function. To save the memory and enhance the performances of the ISR, all variablse and waveform are registered as array in SetUp(). Since the waveform is registered as array, this makes indexing waveform at the given time relatively less resource consuming. The main loop() serves to run the less time relevant function such as connecting to android system as well as updating phase information to android system.

```
void setup() {
  // Initializing all array and parameter
    Serial.begin(19200);/*USB 傳輸速度*/
    analogWriteResolution(12);/*設定輸出解析度為 4096 作為最大值*/
    analogReadResolution(12);
    Timer1.attachInterrupt(functionGen).start(SamplingTime);/*Attach Interrupt Service
Routine (ISR) for action very SamplingTime*/
    for(int i=0;i<N;i++){
        b=pow(2,res)/2;
        Modulation[i]=(b*(0.77+0.11*sin(2*PI*i*k/N))+b);/*Types of output function can be
defined herein. It is very much worth noting here: At roughly 70~degree incidence, a hugh
modulation is still required.*/
        //0.11 output equals to ~0.25 mA
        RefX[i]=(cos(3.8317*sin(2*PI*i*k/N)));/*For now, k=2 and N=100. Therefore, the
waveform goes 50 point for one period, where one point is defined by SamplingTime=100 us. In
conclusion: 5000 us for one period=>200 Hz*/
        RefY[i]=(sin(3.8317*sin(2*PI*i*k/N)));
    }
```

Section A5. Android-Arduino data exchange algorithm

The most important function addressed by the android system is to maintain the serial connection to the Ardunio system. In this way, the phase information as well as other command can works properly. The following code demonstrate the core part of the android code-the serial read function.

```
private void Serial_Read(final UsbDevice device) {
    // TODO Auto-generated method stub
    final Thread Serial_Read = new Thread(new Runnable() {
        public void run() {
            /////////initialization of parameter
            UsbInterface intf = device.getInterface(1);
            UsbEndpoint Ep_In = intf.getEndpoint(1);
            connection = manager.openDevice(device);
            connection.claimInterface(intf, true);
            connection.controlTransfer(0x21, 34, 0, 0, null, 0, 0);
          /*connection.controlTransfer(0x21, 32, 0, 0, new byte[] { (byte) 0x80, 0x25,
0x00, 0x00, 0x00, 0x00, 0x08 }, 7, 0);9600*/
            connection.controlTransfer(0x21, 32, 0, 0, new byte[], 7, 0);//Setting baud-
rate at 19200;
            Serial_Write(connection, device);
            int TimeOUT=10000;
            boolean a=true;
            /////////Main loop structure in the thread to keep reading USB
            while(a){
                NData_Received = connection.bulkTransfer(Ep_In, buffer, 1024,
                TimeOUT);
                try {
                    Thread.sleep(250);
                } catch (InterruptedException e) {
                    // TODO Auto-generated catch block
                    e.printStackTrace();
                }
            }
        }
    }, "Serial_Read");
    Serial_Read.start();
}
```

doi:10.6342/NTU201700804

Due to the serial connection nature, it is necessary to encode the data for sending as well as for reading. **Fig.** *57* demonstrate how Xs, Ys, Xp and Yp are encoded into serial type of data. Principally, due to the non-synchronized nature of serial communication. It is necessary to start the data with an “initiator”, so that all data can be properly read and sent. In present work, this “initiator” bits is 97 (or “a” im ASCII table).

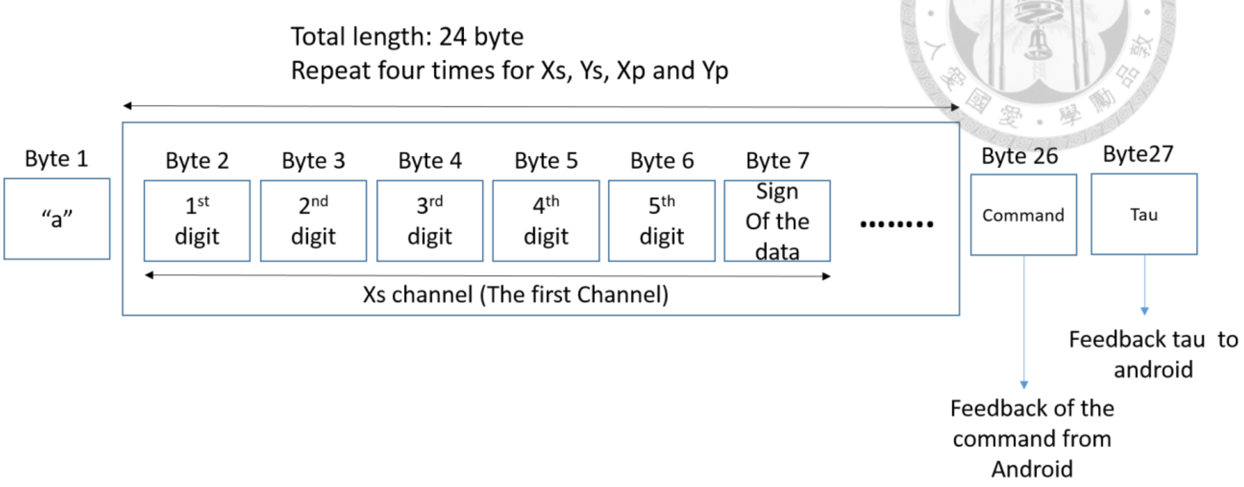

Fig. 57 Android-arduino encoding of data

```
private void Serial_Write(final UsbDeviceConnection connection2,final UsbDevice
device) {
    // TODO Auto-generated method stub
    final Thread Serial_Read = new Thread(new Runnable() {
        public void run() {
            UsbInterface Intf2=device.getInterface(1);
            UsbEndpoint Ep_OUT=Intf2.getEndpoint(0);
            int TimeOUT=10000;
            boolean a=true;
            while(a){
                Data_Sent = connection.bulkTransfer(Ep_OUT, buffer_Out,50,
TimeOUT);
                try {
                    Thread.sleep(100);
                                } catch (InterruptedException e) {
                    // TODO Auto-generated catch block
                    e.printStackTrace();
                }
            }
        }
    }, "Serial_Read");
    Serial_Read.start();
}
```

Phase acquisition function in android:

After *ASCIIencoder()* parsed the phase data that we acquired from the serial cable, the phase data is then sent to PhaseSolver() unit to retrieve the phase response of SPR.

```
void PhaseSolver(){
    //The code is fully examined in 2016/06/17, T.-H
    //Note: Arduino sends un-process X and Y data
    double cos=0;
    double sin=0;
    double u=0.3;
    //Arduino: Vdc=0.77 vs Vac=0.12, u=1/3=0.333; Vpd_dc=3V, Vpd_ac~1V
    double b=0.9162*0.759-u*u*0.1734*0.1734;

    /////////////Extracting Phase of P
    //Adding mu function-0.0
    float X_data=(Xpout[0]+0*Xpout[1])/2;
    float Y_data=(Ypout[0]+0*Ypout[1])/2;

    cos=(0.759*X_data-u*0.1734*Y_data)/b;
    sin=(0.9162*Y_data-u*0.1734*X_data)/b;

    double phase=Math.atan2(sin,cos);
    double amplitude=Math.sqrt(cos*cos+sin*sin);
    phase=360*phase/6.28;
    PhaseData_P.add(phase);
    Amp_P.add(amplitude);

    /////////////Extracting Phase of S
    float Xs_data=(Xsout[0]+0*Xsout[1])/2;
    float Ys_data=(Ysout[0]+0*Ysout[1])/2;
    cos=(0.759*Xs_data-u*0.1734*Ys_data)/b;/*assume u=0.2*/
    sin=(0.9162*Ys_data-u*0.1734*Xs_data)/b;
    phase=Math.atan2(sin,cos);
    phase=360*phase/6.28;
    PhaseData.add(phase);
};
```

Section A6. SiSPR interferogram from portable prototype

Fig. 58 demonstrae the SiSPR interferogram that is obtained from our portable prototype. The data suggest that we have a good contrast around 0.5 in practical measurement which is beneficial for phase retrieval. By varying the power modulation given by the MCU, we can control the phase modulation depth *a* from 0.96 to 3.8317 rad without difficulties. With *a*=3.8317 rad, we can now readily carry out phase detection.

doi:10.6342/NTU201700804

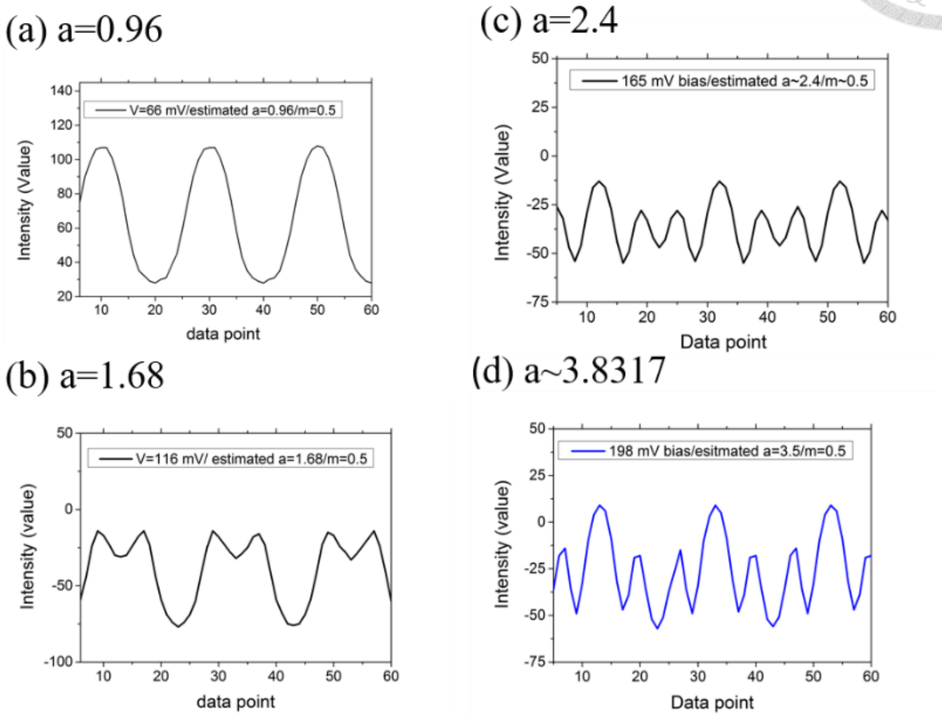

Fig. 58 SiSPR interferogram from portable prototypes.

The phase modulation depth is varied from 0.96 to 3.8317 rad. Each data point in the figure presents 2 *ms*

Appendix A6.Scientific production on the project

1.**Book Chapter**：“Interferometry based on Generalized Lock-in Amplifier (G-LIA): a versatile approach forhase-sensitive sensing and imaging”, ISBN 978-953-51-5116-6, InTech, accepted, 2016
Aurelien Bruyant, Julien Vaillant, Yi Huang, Yunlong Zhu and Tzu-Heng Wu

2.**International Journal**: “DNA biosensor combining single-wavelength colorimetry and digital Lock-in Amplifier within a Smartphone “Tzu-Heng WU**,** Chia-Chen CHANG, Julien VAILLANT, Aurélien BRUYANT* and Chii-Wann LIN*, *Lab-On-a-Chip*, under accepted, 2016

3. .**International Journal**：“Characteristic investigation of scanning surface plasmon microscopy for neucleotide functionalized nano-array”, Shih-Chung WEI, Pei-Tung YANG, Tzu-Heng WU, Yin-Lin LU, Frank GU, Kung-Bin Sung and Chii-Wann Lin. *Optics Express,* 2015, 23, 20104

5. .**International Journal**:“Scanning surface plasmon resonance microscope for nano-array biochip imaging” PT Yang, SC Wei, YL Lu, TH Wu, HH Lu, KB Sung, CW Lin, *Japanese Society for Medical and Biological Engineering*, 2013

6. .**International Journal**:“Aptamer-based colorimetric detection of platelet-derived growth factor using un-modified gold nanoparticles” Chia-Chen Chang, Shih-Chung Wei, Tzu-Heng Wu, Chung-Han Lee, Chii-Wann Lin*,*Biosensor and Bioelectronics,* 2012,42, 119

7. .**International Journal:**Label-free colorimetric aptasensor for IgE using DNA pseudoknot probe” CC Chang, CY Chen, X Zhao, TH Wu, SC Wei, CW Lin, *Analyst* 2014,139 (13), 3347-3351

8. .**International Journal**：“Nano-wire Transistor based Ultrasensitive Virus Detection with Reversible Surface Functionalizaion” PL Chiang, TC Chou, TH Wu, CC Li, CD Liao, JY Lin, MH Tasi, CC Tasi, CJ Sun, CH Wang, JM Fang and YT Chen, *Chemistry-An Asian Journal*, 2012,9, 2073

9. .**International Journal**:“Aptamer-based colorimetric detection of proteins using a branched DNA cascade amplification strategy and unmodified gold nanoparticles” CC Chang, CY Chen, TL Chuang, TH Wu, SC Wei, H Liao, CW Lin Biosensors and Bioelectronics 2016, 78, 200-205

10.**Seminar paper**:Proceedings of 2015 International Symposium on Smart-Sensing Technology (2015 ISST) and 20th Symposium of Association for Chemical Sensors in

doi:10.6342/NTU201700804

Taiwan (20th SACST) “Aptamer based gold nano-particle colorimetry detection of cancer marker using smartphone” Tzu-Heng WU, Chia-Chen CHANG , Chii-Wann LIN

11. **Seminar paper**:2013 Asian Conference of Chemical Sensors at Chiang-Mai, Tai-Land, ” Nano-dots enhanced fluorescence beacon sensor array for interferon-g 2-D sensing” Tzu-Heng Wu, Shih-Chung Wei, Chia-Chen Chang, Hui-Shin Lu, and Chii-Wann Lin

12. **Seminar paper**:2015 Asian Conference of Chemical Sensors at Penang, Malaysia ” Cancer Biomarker Screening via Aptameric Colorimetry with Smart Phone” Tzu-Heng WU, Chia-Chen CHANG, Julien VAILLANT, Aurélien BRUYANT* and Chii-Wann LIN*

13. **Seminar paper**:Symposium of Association for Chemical Sensors in Taiwan, “Using gold nano-disk array as microscope based bio-sensor: from fabrication to potential application” Tzu-Heng Wu, Shih-Chung Wei and Chii-Wann Lin

14. **Patent:** Apparatus and method for compact interferometric sensor based on bi-reflective layer” Inventor: Aurelien BRUYANT, Julien VAlAINT, Tzu-Heng WU, Chii-Wann LIN,WIPO-PCT, 2016, reference:PCT/EP2016/054852

doi:10.6342/NTU201700804

Appendix A7.Extended French Abstract

Au cours des dix dernières années, deux facteurs impactant fortement la sphère socio-économique ont pu apporter un nouvel éclairage et une accélération au champ de recherche des capteurs, en particulier dans le domaine médical. Le premier facteur est l’augmentation importante et continue de la population mondiale, qui atteint 7,4 milliards d’individus au début d’année 2017. Si nous regardons la structure de cette population au sein des pays développés, les personnes âgées de plus de 65 ans représentent 12 à 20% de cet ensemble. Le vieillissement et l’accroissement d’une large population a de nombreuses conséquences fondamentales sur nos sociétés, et particulièrement sur les systèmes de soins médicaux. A titre d’exemple, en France, la maintenance du système de santé occupe près de 20% du produit intérieur brut (PIB), ce qui correspond à une taxe annuelle de près de 3000 euros pour chaque citoyen. A Taïwan également, le cout annuel de ce secteur s’élève à près de 12% du PIB. Autrement dit, l’augmentation de la durée de vie et la croissance de population font peser une pression énorme et toujours plus importante sur les prestations de services de santé.

Le deuxième facteur d’importance correspond à l’expansion spectaculaire, depuis 12 ans, des dispositifs électroniques grand public que sont en particulier les dispositifs intelligents ou « smart devices » comme les tablettes, téléphones mobiles et smart-phones. Il est en effet remarquable que près de 70% de la population mondiale possède

doi:10.6342/NTU201700804

aujourd’hui au moins un de ces dispositifs, au point qu’ils apparaissent, par leur omniprésence et leurs capacités techniques, comme un modus operandi inespéré pour repenser la mise en œuvre de dispositifs de soin en intégrant des capteurs pour du dépistage ou du diagnostic, au plus près des patients.

Par exemple, la prise audio jack d’un smartphone comme celui représenté sur l’illustration ci-après, peut être utilisée comme convertisseur analogique/digital 16 bits bidirectionnel (1 entrée/ 2 sorties), c'est-à-dire un convertisseur dont les performances sont comparables à des cartes d’acquisition suffisamment performantes pour extraire, traiter, et analyser avec une grande précision des flux de données issus de capteurs. Par cette même voie, l’échantillonnage synchronisé de données possède une résolution temporelle atteignant 26 µs par point, largement suffisante par exemple pour des mesures

Fig. 1 smartphone capacité

doi:10.6342/NTU201700804

de temps de fluorescence exigeantes[p] ou l’extraction de signaux modulés à haute fréquence, pour la mesure de phase notamment. Cette voie audio-jack a ainsi été employée pour des mesures d’Électrocardiogrammes (ECG) et d’oxymétrie de pouls[6]. Smartphones et tablettes possèdent également, pour l’essentiel, une source optique blanche pour la prise de photo (LED blanche, au dos), et un écran à LED sur la face avant. L’écran à LED possède 3 couleurs d’émission distinctes pouvant être utilisées indépendamment, comme indiqué sur la **Fig. 1**

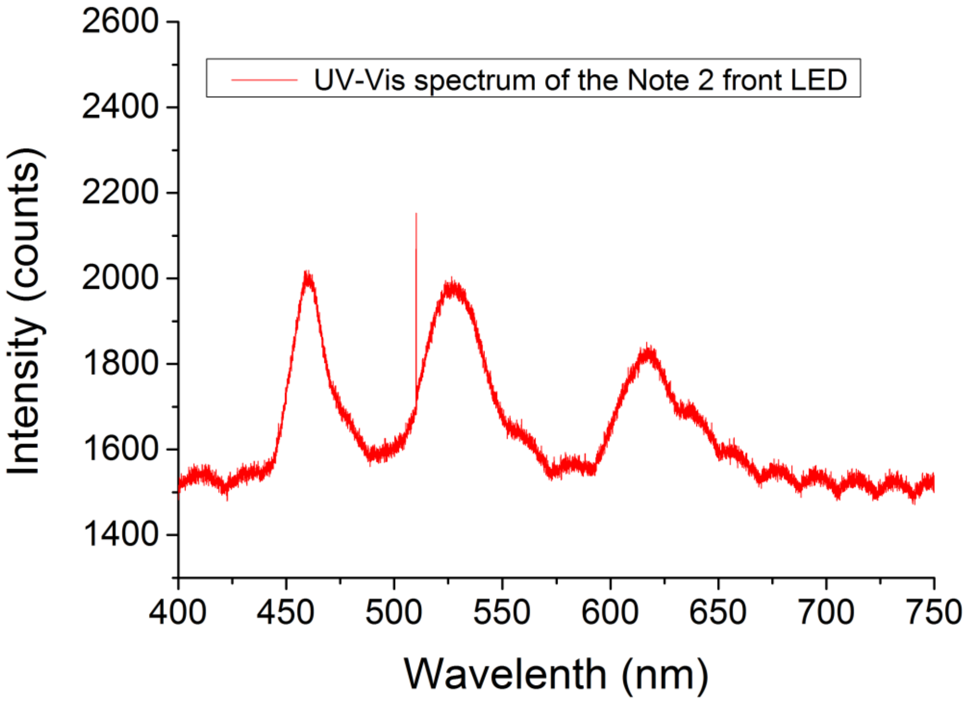

Fig. 2 Spectre d’émission du panneau de LED principal du Note 2 (Samsung).

---

[p] On pense notamment aux techniques d’imagerie de temps de vie de fluorescence (FLIN : Fluorescence-lifetime imaging microscopy).

doi:10.6342/NTU201700804

Certains travaux utilisent ainsi ce type de sources pour réaliser l'excitation de Résonance de Plasmon de Surface[7], technique de choix pour la détection d'éléments biochimiques. Les smartphones possèdent aussi des caméras intégrées, des CMOS pour la plupart, pouvant naturellement être utilisées comme puissance-mètre optique[4, 8, 9]. En sus d'une puissance de calcul relativement importante, les smartphones peuvent également fournir une connexion à d'autres systèmes intégrés par connexion sans fil ou USB. Ces connecteurs peuvent également servir de source de puissance pour alimenter des capteurs intégrés venant suppléer le smartphone (e.g. protocoles USB-On-The-Go).

Dans ce contexte favorable à la « e-santé » visant à alléger le coût des systèmes de soin et de dépistage, et compte tenu de l'intégration croissante de micro-capteurs à visée métrologique au sein des dispositifs électroniques intelligents (gyroscope, capteur à effet hall, etc.), l'utilisation de smartphones comme plateforme technologique disponible au « chevet du malade » (Point of Care, POC) pour du diagnostic ponctuel, ou du suivi, est une approche émergente appelée à se développer. Par ce biais, des diagnostics ou des tests médicaux pourront être réalisés de manière « décentralisée », en contraste avec les modèles conventionnels de diagnostic qui s'effectuent dans les laboratoires d'analyse et les hôpitaux, réduisant alors le coût lié au transport de ressources médicales vers les centres de soins, la mobilisation de personnels médicaux, etc. Ce scénario est supporté par des rapports issus du secteur public. Par exemple la FDA (Food and Drug

doi:10.6342/NTU201700804

Administration) aux Etats-Unis mentionnait début 2015 dans “Mobile Medical Applications” que:

~“*The Food and Drug Administration (FDA) recognizes the extensive variety of actual and potential functions of mobile apps, the rapid pace of innovation in mobile apps, and the potential benefits and risks to public health represented by these apps.*”

L’organisation mondiale de la santé mentionne également [10]:

~“*Mobile technologies have the potential to bridge systemic gaps needed to improve access to and use of health service, particularly among underserved populations.”*

Au-delà du secteur publique, nous notons une croissance rapide dans les nouveaux produits disponibles dans le marché de la santé mobile (m-health) [11].

Pour résumer, des outils de diagnostic traditionnellement centralisés en laboratoires pourront a priori être intégrés sur des dispositifs électroniques grand public et fournir une assistance au diagnostic sans limite géographique et dans des délais réduits. Ce but ne peut cependant pas être réalisé sans transdisciplinarité, ne serait-ce que pour la réalisation de ces plateformes de détection intégrées (biologie, optique, physique, électronique, …). Le design du capteur optique, du circuit de lecture et d’acquisition, ainsi que l’application logiciel nécessaire au traitement et à l’interfaçage doivent être considéré avec soin.

C’est l’objet de cette thèse. Plus précisément, nous nous intéressons au développement de biocapteurs de type plasmonique qui puisse être aisément être couplé à un smartphone

doi:10.6342/NTU201700804

ou une tablette avec un coût faible et une grande fiabilité et sensibilité. Pour mettre en perspective ce travail dans le contexte applicatif mentionné, nous tâcherons également d'identifier des besoins et des utilisateurs finaux pertinents pour le dispositif développé, c'est-à-dire définir des cibles à détecter pertinentes, où la portabilité offre un réel intérêt. Le manuscrit, que nous résumons ici, est découpé en deux parties principales, correspondant à deux dispositifs plasmoniques de détection, couplés directement à un smartphone. Ces deux dispositifs portables et bas cout sont réalisés dans l'optique de pouvoir être utilisé facilement, sans ressource instrumentale particulière, avec comme perspective à plus long terme, la possibilité de pouvoir être utilisés, par exemple, dans des cabinets de médecin ou au chevet du patient, pour réaliser ces tests que l'on désigne sous le sigle anglais POCT pour « Point of Care Testing ».

doi:10.6342/NTU201700804

1) Partie 1 : Approche colorimétrique, mono-longueur d’onde

Dans une première partie de ce manuscrit, nous démontrons la possibilité de détecter des brins d’ADN 15-mer[q], dans un laps de temps de 15 minutes et une limite de détection de 0.77 nM. Pour la longueur d’onde considérée, cette limite de détection est environ 6 fois supérieure à celle d’un spectromètre UV-Visible conventionnel.

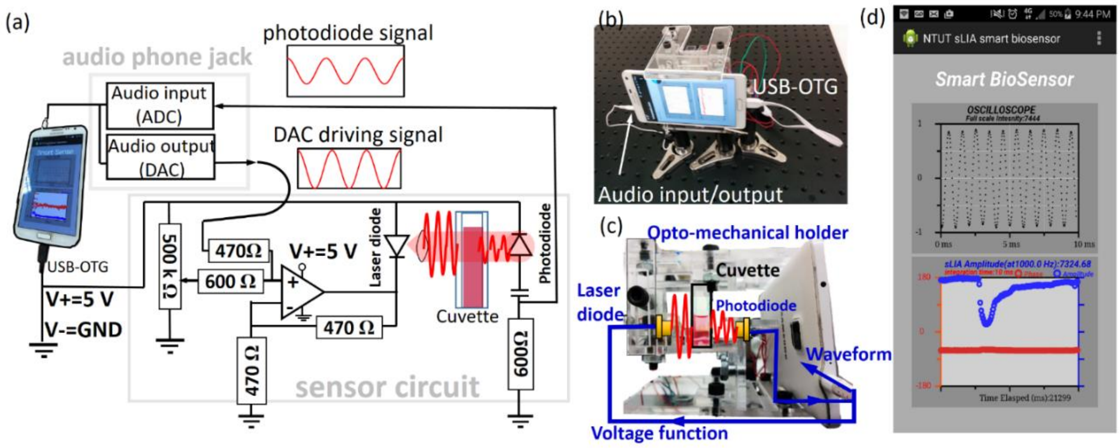

Fig. 3 Prototype permettant d’effectuer la colorimétrie de nano-particules d’or sur smartphone (mono-longueur d’onde). (a) Schéma électrique. L’alimentation de 5V provient du port mini-USB du smartphone. La détection synchrone (SBLIA) est logicielle. (b) Photographie du prototype en face avant et (c) en vue de profil. (d) Interface utilisateur (UI) de l’application Android. Le graphe du haut représente, le signal brut reçu de l’entrée audio. Le graphe du bas représente l’amplitude (bleu) et la phase (rouge) du signal démodulé.

Parmi les nombreux outils de diagnostic basés sur l’utilisation d’un smart-phone et de son capteur CMOS intégré, la colorimétrie de nano-particules d’or (dénommé SCB-AuNP colorimetry dans le corps du manuscrit) a démontré un grand potentiel[3, 14-16] pour la détection de matériel ADN. La présence d’une caméra couleur sensible évite l’utilisation

---

[q] “-mer”: du grecque *meros*, significant part, ou partie. Ce suffixe est utilisé pour dénoter la longueur des oligonucléotides, soit le nombre d’acides nucléiques formant le brin ADN ou ARN.

d’un spectromètre classique, typiquement encombrant et couteux, tout en permettant une mesure quantitative, et sur site, des résultats de colorimétrie de type SCB-AuNP.

Pour la détection d’ADN, de l’ADN mono-brin (ssDNA: single-strand DNA), dit ADN « sonde », est ajouté à une solution de nano-particules d’or mono-disperse, dans le but de prévenir l’agrégation naturelle des particules d’or en présence d’une solution saline. Lorsque le brin d’ADN complémentaire, qui est l’ADN cible, est présent dans la solution, une hybridation entre l’ADN sonde et cible se produit. L’ADN double brin (dsDNA) résultant est nettement plus rigide dans sa structure moléculaire et n’empêche plus efficacement l’agrégation des particules d’or. Cette agrégation de particules, induit un changement de couleur détectable de la solution par la caméra couleur, si celle-ci est suffisamment sensible et après traitement et analyse des images. Grâce à l’interface utilisateur (UI) qu’offre le smartphone, on obtient ainsi un rapport mis à jour en temps réel sur la présence ou non de l’ADN cible.

Cette approche présente néanmoins des limitations notables :

- L’utilisation d’un capteur CMOS ou CCD, limite la profondeur d’échantillonnage, ceux-ci étant typiquement limité à un codage sur 8 bits (256 niveaux), ce qui limite nécessairement la sensibilité.
- La vitesse acquisition vidéo est nécessairement limitée (~100 Hz maximum pour les produits les plus performants seulement).

doi:10.6342/NTU201700804

Ces contraintes empêchent la détection SCB-AuNPs sur caméra d'atteindre les niveaux de détection accessibles par détection synchrone (LIA : Lock-in amplifier) de signaux modulés à haute fréquence. En comparaison, la voie audio Jack, pour rappel, permet d'atteindre 16 bits à une cadence de *44100* points par seconde. Ceci permet de travailler avec des signaux optiques modulés à des fréquences suffisantes pour limiter le bruit en *1/f* et permettre, a priori, d'effectuer une détection synchrone pour repousser les seuils de détection de la colorimétrie par smartphone. Nous avons donc proposé d'effectuer la détection du changement de couleur en travaillant à une longueur d'onde fixe et en utilisant un détecteur ponctuel relié à la prise jack des smartphones. Dans cette approche, une photodiode silicium reliée à la carte son du téléphone se substitue donc au capteur CMOS, et une sensibilité très importante peut être obtenue en implémentant un LIA logiciel (SBLIA : Software-Based LIA) directement sur le portable. Cette approche est représentée sur la figure **Fig. 3**.

Comme nous pouvons le voir sur la **Fig. 3** (a), le smartphone est utilisé comme générateur de fonction sinusoïdale via la sortie audio-jack pour moduler une diode laser émettant à 650 nm. La lumière rouge modulée traverse la solution contenant les nanoparticules et l'ADN monobrin. Le photodétecteur également branché à la prise jack transmets le signal modulé détecté à une application codée pour effectuer la SBLIA, permettant d'extraire l'amplitude du signal modulé tout en filtrant les autres composantes

doi:10.6342/NTU201700804

fréquentielles, sources de bruit. Les éventuelles modifications dans l'amplitude du signal modulé pouvant être provoquées par un changement de couleur en cas d'agrégation (cf. **Fig. 3**) sont affichées sur l'interface utilisateur de l'application qui présente la transmission optique en temps réel.

Analyse des signaux

Pour qualifier les performances du prototype, les performances des voies audio pour enregistrer et générer des signaux ont été analysés. La **Fig.4** (a) montre que la voie audio de sortie permets de générer une tension d'amplitude allant de 2 mV à 240 mV. Une fréquence de 4kHz peut être atteinte sans distorsion notable du signal ; au-delà , en revanche, une distorsion est observée, (cf. **Fig.4** (c)).

doi:10.6342/NTU201700804

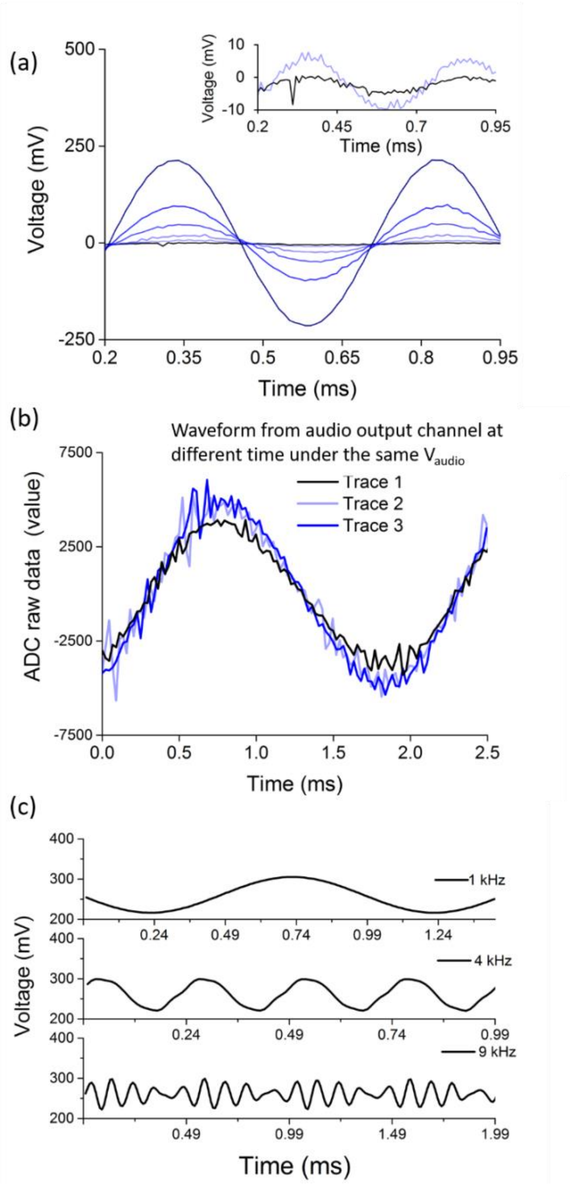

Fig.4 Evaluation de la voie audio de sortie (générateur) pour le SBLIA

(a) Signal $V_{audio\ out}(t)$ pour plusieurs amplitudes V_{audio}. L’insert représente le signal $V_{audio\ out}(t)$ avec une échelle agrandie pour les faibles V_{audio} (rapport signal à bruit dégradé).

(b) $V_{audio\ out}(t)$: Représentation de plusieurs traces en différents temps.

(c) $V_{audio\ out}(t)$ pour des fréquences croissantes (de haut en bas : 1 kHz, 4 kHz et 9kHz respectivement).

Nous avons également observé le spectre de bruit et les paramètres de travail permettant d’optimiser les performances du SBLIA. Les résultats sont représentés **Fig. 5**

doi:10.6342/NTU201700804

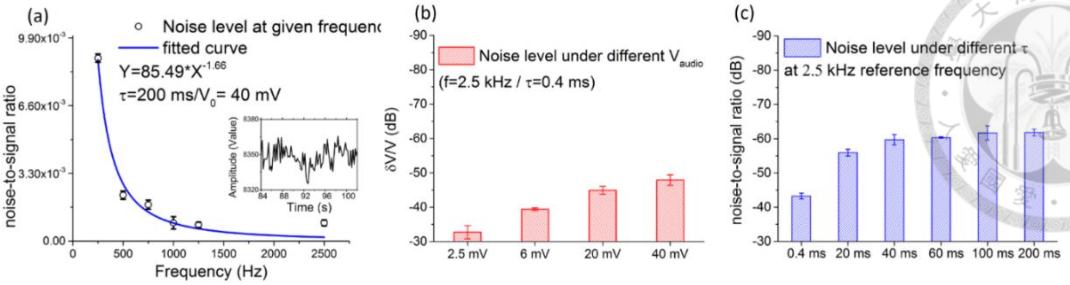

Fig. 5 Niveau de bruit et effet des paramètres de travail sur le SBLIA.
(a) Spectre de bruit en sortie de SBLIA: observation du bruit de Flicker en 1/f. L'évaluation est menée pour une fréquence *f=2.5* kHz et le niveau de bruit est estimé sur τ=200 ms. L'insert représente une trace de signal SBLIA en amplitude utilisée pour l'estimation du rapport bruit sur signal. (b) Bruit mesuré pour différents niveaux de sortie V_{audio} à fréquence fixe. L'évaluation est réalisée pour f=2.5 kHz et un faible temps d'intégration (τ=0.4 ms). (c) montre l'évolution du rapport bruit sur signal pour différents temps τ, qui tends à saturer vers -63dB. L'évaluation est réalisée pour f =2.5 kHz, et V_0 =40 mV. Les écarts type sur les mesures de bruit sont obtenus à partir de trois ensembles de mesures.

Table 5. Comparaison de la méthode SBLIA et SCB

Technologie	**Coût du système**	**Resolution fréquence**	**NSR**	**Materiel requis**	**Suppression du fond lumineux ambient**
SCB	Smartphone: 400-600 USD [21] et ~15 USD pour le support optique	8 à 12 bits 100 Hz	-48 dB[22]	1. source optique 2. camera (built-in)	Stratégies: 1. Réglage de la balance des blancs 2. Calibration[18] 3. Boite
SBLIA		16 bits 44.1 kHz	-63 dB	1. source optique, 2.photodetecteur 3. port son (built-in)	Non affecté

Comme représenté sur la Fig. (a), un bruit Flicker présentant une décroissance caractéristique en fréquence est présent. La modélisation du rapport bruit sur signal (NSR ; noise to signal ratio) indique une dépendance fréquentielle de la forme : $NSR(f)=85.49\,f^{-}$

$^{1.66}$. Cette dépendance explicite le gain apporté par l'utilisation de la méthode SLBIA réalisée à une fréquence suffisante (e.g. >2.5 kHz). On constate que le SBLIA diminue largement le bruit environnemental (Le bruit est réduit de 85%). La figure 6.(c) montre que le SBLIA permet d'atteindre un NSR de -63dB en choisissant une fréquence et un temps d'intégration suffisant, correspondant à une amélioration d'un facteur 30 environ sur les méthodes SCB rapportées par ailleurs. Le SBLIA permet aussi de rendre la détection relativement insensible aux conditions d'éclairage ambient comme mentionné sur la **Table 1**, celui-ci n'étant pas modulé à la fréquence choisie.

Mesures et discussion

Finalement, la détection d'ADN 15-mer est reportée sur la **Fig. 7 Colorimétrie de nanoparticules d'or par SBLIA**. Dans ce test, le DNA cible est successivement mélangé en concentration de 20, 40, 80 et 120 nM dans les solutions aqueuses de nanoparticules d'or contenant une concentration de 200 nM d'ADN sonde. Ces solutions sont réalisées en incubant pour 5 minutes l'ADN sonde dans une concentration de sel donnée.

doi:10.6342/NTU201700804

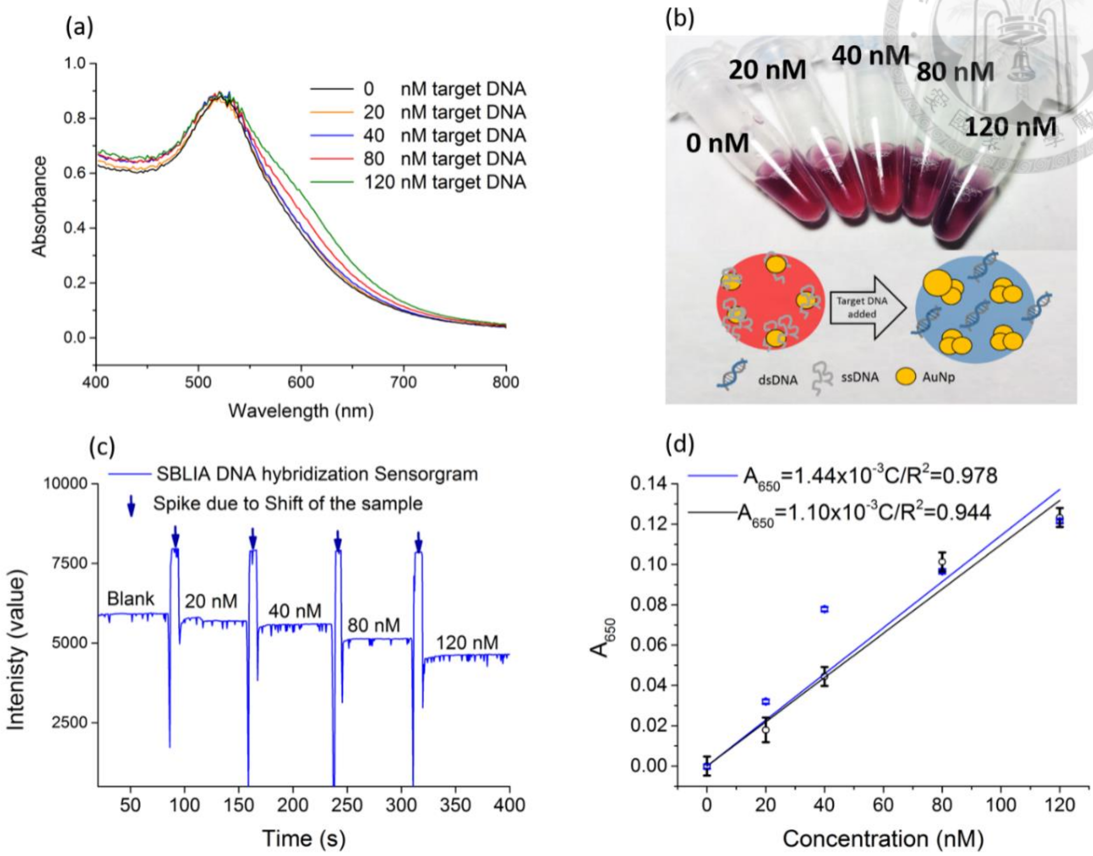

Fig. 7 Colorimétrie de nanoparticules d'or par SBLIA. (a) Spectre UV-visible des solutions de concentrations croissantes en ADN cible (avec 200 nM d'ADN mono-brin). (b) Image des échantillons et représentation schématique du mécanisme de détection. (c) Colorimétrie par SBLIA à longueur d'onde fixe. La concentration en ADN cible est indiquée. (d) Courbe de calibration pour l'approche colorimétrique (trace bleue) et par spectroscopie UV-Visible (trace noire).

L'ADN cible est ensuite ajouté et laissé à reposer pour 10 minutes dans la solution avant de réaliser la mesure. Des spectres UV-visble en transmission sont alors réalisés à travers les solutions. Les mesures sont représentées sur la **Fig. 7 (a)**. La couleur des solutions peut être observée sur la **Fig. 7 (b)**. Les échantillons de concentration croissantes présentent un gradient de couleur allant du rouge au violet foncé après que la cible ait été ajoutée. Ce gradient de couleur, comme mentionné, est dû à la propension différente des simples et doubles brins à prévenir l'agrégation des sels de nanoparticules d'or. L'agrégation des particules modifie sensiblement l'absorption, en particulier autour de *650* nm, comme nous pouvons le constater sur les spectres. Le même ensemble d'échantillon est mesuré par SBLIA comme représenté sur la **Fig. 7 (c)**. Pour comparer les performances des deux systèmes, les données sont transformées en unité d'absorption à *650* nm et les courbes de calibration correspondantes sont générées et représentées sur la **Fig. 7 (d)**. Dans les deux cas, l'absorbance à 650 nm (A_{650}) a une dépendance similaire, linéaire à la concentration (C, in unit of nano-molar) en ADN cible : ($A_{650}=1.44x10^{-3}$ C, $A_{650}=1.1x10^{-3}C$) pour le SBLIA et le système for UV-Visible respectivement. Cette similitude est compréhensible d'après la loi de Beer-Lambert, considérant que les deux systèmes utilisent une cuvette ayant les mêmes dimensions (même chemin optique). L'analyse du bruit sur ces systèmes montrent également que le SLBIA offre un bruit 4.3 inférieur au système UV-Visible à la même longueur d'onde (3.7×10^{-4} AU vs. 1.6×10^{-3} AU). Compte tenu du bruit obtenu et des courbes de calibration, nous calculons une limite de détection (LOD: Limit of Detection) de 0.77 nM, contre 4.36 nM par spectroscopie UV-Visible, soit un facteur d'amélioration de 5,7.

doi:10.6342/NTU201700804

Au-delà de ce simple résultat numérique et de la méthode colorimétrique employée, l'intérêt est ici de constater la pertinence de la détection synchrone logicielle sur smartphone (SBLIA), à l'aide d'une application permettant de synchroniser modulation et référence électronique de démodulation pour réduire drastiquement le bruit.

En effet, la SBLIA développée peut être employée sans cout supplémentaire pour améliorer les performances métrologiques de nombreux capteurs optiques amenés à se développer sur smartphone.

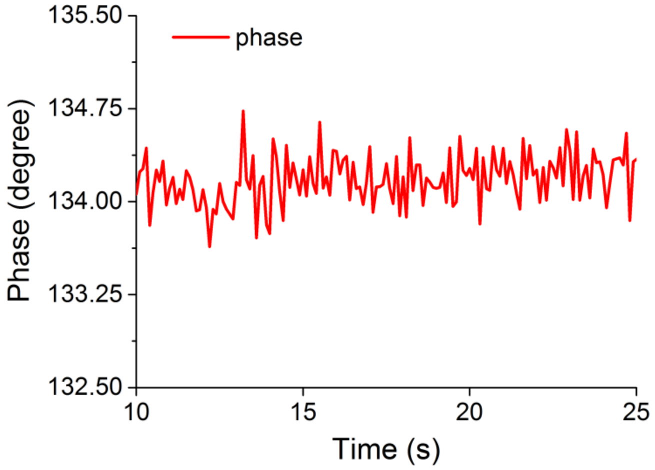

Fig. 8 Signal de phase du SBLIA.

La SBLIA permet également de déterminer la phase d'un signal modulé, et peut être envisagée pour extraire la phase optique au sein de dispositifs interférométriques mettant en œuvre des modulateurs de phase. Dans notre cas, pour les temps d'intégration employés, le bruit de phase descend à 0.2° (cf. **Fig.8**). Ainsi, la détection synchrone logicielle sur smartphone peut-être aussi employée pour des applications « biocapteur » reposant, par exemple, sur une mesure de fluorescence modulée[23], la détection en phase

doi:10.6342/NTU201700804

de résonance plasmonique[24], ou encore sur des systèmes holographiques (détection en phase « multicanal »). Concernant l'utilisation d'un dispositif similaire à celui développé pour du diagnostic PCOT, il convient de relativiser les possibilités immédiates pour ce type d'application. Remarquons que les performances finales d'outils de diagnostic reposant sur l'utilisation principale de smartphone font encore l'objet de débats[8], tant il vrai qu'un nombre important de facteurs rentre en jeux lorsqu'il s'agit de détection en dehors des conditions idéales d'un laboratoire, dans lequel par exemple des solutions relativement pures peuvent être utilisées. Il convient de souligner la complexité des échantillons physiologique[26] et les problèmes de préparation et de purification afférents[27]. Néanmoins des appareils de diagnostic "smart" ont déjà atteint les niveaux de références requis par l'OMS ou d'autre standards [3,9], et ont déjà été appliqués sur site pour le dépistage de maladies[4]. Notre travail illustre cette capacité de détection performante pour le diagnostic à l'aide de smartphone, en démontrant la possibilité d'obtenir des performances égales ou supérieures à certains systèmes de laboratoire couramment employé pour ces tâches.

2) Partie 2 : plateforme de détection interférométrique « SPR »

Dans la seconde partie de cette thèse, nous nous intéressons au développement d'un dispositif de détection « Résonance à Plasmon de Surface (SPR) » ultra-sensible sur smartphone, en vue d'application comme biocapteur pour du POCT. Les dispositifs SPR

doi:10.6342/NTU201700804

sont notamment utilisés pour de la détection biologique immunitaire obtenue en fonctionnalisant une surface optiquement résonante avec des anticorps ou d'autres ligands. Dans le visible, la surface résonance est typiquement constituée d'une fine couche métallique d'or ou d'argent. Bien que l'argent produise une sensibilité accrue ce métal se sulfurise à l'air. L'or, inerte et facilement fonctionnalisable est généralement employé avec des épaisseurs de 50 nm environ. Nous détaillons les caractéristiques principales de ce type détection dans le manuscrit.

Pour ce second prototype, l'interfaçage par la voie audio jack, quoique possible, est délaissée au profit d'une connexion sur le port mini-USB à un microcontrôleur de type Arduino, branché au smartphone, qui permet de gérer un nombre plus important de signaux, et permet plus de flexibilité dans le design. Notre plateforme optique est donc un système SPR, qui se distingue cependant de l'existant par le fait qu'il permet de monitorer la résonance plasmonique par une lecture de phase optique. Le dispositif optique permettant cette lecture de phase s'apparente, sur la forme, à interféromètre à dédoublement latéral (« shearing interferometer ») tout en incorporant une modulation de phase et un système de démodulation électronique. Ce dispositif et son principe sera ainsi désigné par le sigle SiSPR pour "Shearing Interferometry based Surface Plasmon Resonance (SiSPR)". Ce type de dispositif a été développé dans le rouge et le proche infrarouge (850nm). La sensibilité intrinsèque des système SPR est généralement estimée

doi:10.6342/NTU201700804

en donnant la variation d’indice de réfraction minimale détectable (donné en « RIU » pour Refractive Index Unit). La mesure de phase apparait d’une très grande stabilité et en intégrant sur des temps courts (<100ms), une valeur de 2.10^{-6} RIU en sensibilité est obtenu à l’aide de couche d’or. A titre de comparaison, dans des conditions similaires, la sensibilité des dispositifs fonctionnant en amplitude est typiquement de 10^{-5} RIU, pour des systèmes commerciaux notamment. La dynamique en phase obtenue est, quant à elle, autour de $7.0x10^{-3}$ RIU. Une étude des publications antérieures semble montrer que le SiSPR est le premier dispositif SPR résolu en phase réellement portable. Nous fournissons dans le manuscrit, une étude complète du SiSPR sur le plan théorique, de sa réalisation, de la méthode d’extraction de la phase et sur la manière d’implémenter le système sur un portable.

La force principale des systèmes de détection SPR est sans doute la possibilité de détecter

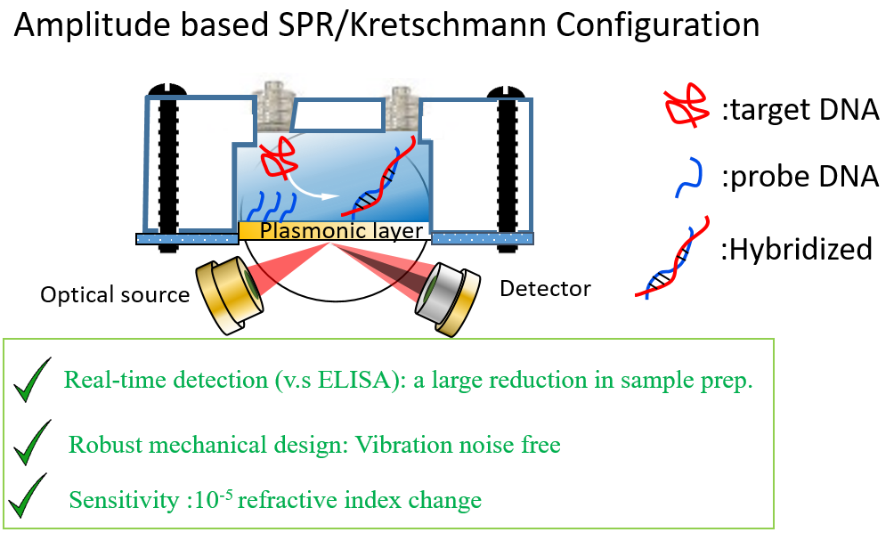

✓ Real-time detection (v.s ELISA): a large reduction in sample prep.

✓ Robust mechanical design: Vibration noise free

✓ Sensitivity :10^{-5} refractive index change

Fig. 9 Configuration SPR Kretschmann.

sans marqueur et en temps réel, ce qui explique leur succès comme biocapteur et pour le diagnostic[16]. L'arrangement optique le plus courant et le plus utilisé est correspond à la « configuration Kretschmann » représentée **Fig. 9** Au-delà des avantages mentionnés ci-dessus, les SPR fonctionnant en "Kretschmann" sont mécaniquement robuste et simple, dans le sens où très peu d'optiques sont nécessaires à la fabrication. Cependant pour le POCT, un niveau faible de préparation/purification de l'échantillon à analyser est aussi important. La sensibilité à un biomarqueur est en effet dégradée lorsque celui-ci est au sein d'un fluide physiologique, qu'il s'agisse d'un échantillon complètement « brut » ou bien seulement filtré. Des études précédentes on montrées que les SPR classiques voient leur sensibilité réduite d'un facteur 100 dans ces conditions[50] (sérum, salive, urine). Ceci porte alors les limites de sensibilité classiques du nano-molaire ou mieux au domaine micro-molaire. Cette réduction en sensibilité est réellement préjudiciable car elle empêche de détecter de nombreux biomarqueurs importants dans le domaine de la santé et dont les concentrations d'intérêt sont souvent dans le domaine nano-molaire. Pour résoudre ce dilemme, l'interrogation en phase, par nature plus sensible, a été avancée comme solution potentielle. On considère effectivement que la mesure SPR en phase permet d'obtenir une augmentation d'un facteur 100 sur la sensibilité par rapport à une mesure en amplitude seule. Néanmoins, l'interrogation SPR en phase utilise souvent de nombreux composants optoélectroniques tel que des séparatrices, des cristaux

doi:10.6342/NTU201700804

piézoélectriques, des modulateurs acousto-optiques ou des sources optiques cohérentes accordables, etc. Ceci accroit la complexité, le poids et le cout du dispositif final. De plus, les interféromètres sont, presque par nature, très vulnérables aux vibrations mécaniques produites par la voie, des déplacements, du trafic routier avoisinant, etc. Le challenge de notre approche est donc de lever ces verrous reconnus, propres à l'interférométrie.

Présentation du dispositif

Le dispositif interférométrique à séparation latérale que nous proposons est représenté sur la **Fig. *10*** La puce plasmonique est une lame de verre recouverte d'une fine couche d'or sur sa face supérieure. L'épaisseur, typiquement 50 nm, est choisie pour permettre l'existence d'une onde de surface lorsque la surface est éclairée sous le bon angle dit « angle de Kretschmann ». A cet angle, une grande partie du flux de lumière incident est donc dissipée dans la couche plasmonique supérieure où elle résonne et se propage. La réflexion sur cette couche supérieure se caractérise par un minimum marqué, ce qui permet de savoir que l'angle est correct. Notons encore que l'angle de résonance dépend fortement de l'indice du milieu supérieur et que, en pratique, le milieu supérieur recouvrant la couche sera le plus souvent un fluide à analyser. La couche d'or quant-à-elle, peut être fonctionnalisée pour détecter une cible donnée au sein d'un fluide (biomarqueur).

Un VCSEL émettant à 850 nm (Vertical Cavity Surface Emitting Laser, VCSEL) ou

doi:10.6342/NTU201700804

dans le visible est ainsi orienté, en direction de la couche d’or plasmonique, à l’angle de Kretschmann pour exciter l’onde plasmonique de surface. Pour exciter la puce plasmonique avec un angle unique, la face de sortie du VCSEL est placé au foyer focal objet d’une lentille hémisphérique. La lumière se trouve ainsi collimatée à l’angle choisi et la largeur du faisceau collimaté est notée *w*. Par rapport à un système SPR conventionnel, notre lame déposée sur la demi-boule a aussi une spécificité : nous effectuons également un dépôt sur la couche inférieure. La face inférieure joue donc le rôle de séparatrice. La lumière incidente par le bas est d’abord réfléchit sur cette première interface. Cette portion de faisceau en amont du 1^{er} point de contact est nommé “Beam 1”.

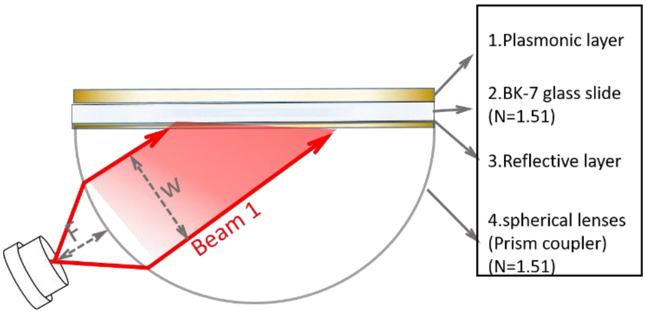

Fig. 10 “Beam 1” dans le système SiSPR.

Ce faisceau est partiellement réfléchit sur la face inférieure de la puce pour former la seconde portion de faisceau, notée « Beam 2 » sur la **Section (a)**, qui ne perçoit pas l’interface supérieure et servira donc de faisceau de référence pour le SiSPR. En retraversant la demi-boule, “Beam 2” converge vers un foyer du dioptre sphérique. Le centre du spot elliptique formé à la première réflexion est représenté par une ligne

doi:10.6342/NTU201700804

pointillée verticale sur la figure. La partie qui, à la première interface, n'est pas réfléchie mais transmise est la portion « beam 3 » (cf. ***Fig 11(b)***). On note que le faisceau est transmis avec une réfraction nulle dans la puce, car les indices optiques de part et d'autre de l'interface sont identiques. Ce faisceau, ayant l'inclinaison requise excite une résonance plasmonique dans la couche d'or supérieure. Il est finalement réfléchit pour former le « Beam 4 » (**Section (c)**). Le centre du spot elliptique formé sur la surface supérieure est également représenté par une ligne en pointillée verticale. On note que le Beam 4 est fortement atténué et déphasé, et qu'il contient en cela l'information utile. En effet, l'atténuation d'amplitude et le déphasage varient si des liaisons moléculaires se forment sur les ligands en surface de la couche d'or. Le "Beam 4" est réfléchit avec le même angle que le "Beam 2" et peut donc interférer correctement avec lui; mais ces deux faisceaux sont cependant latéralement décalés l'un par rapport à l'autre, d'où le terme « interféromètre à décalage latéral ». Comme l'indique la **Section (d)**, ces deux faisceaux se recouvrent partiellement et interfèrent donc dans la puce, et en dehors après avoir retraversé le dioptre sphérique. Une caméra dépourvue de filtre IR peut être utilisée pour visualiser le motif d'interférence entre le faisceau signal (Beam 4) et le faisceau référence (Beam 2), en sortie, par exemple le long de la ligne en pointillé, représentée sur la **Section**

doi:10.6342/NTU201700804

(d).

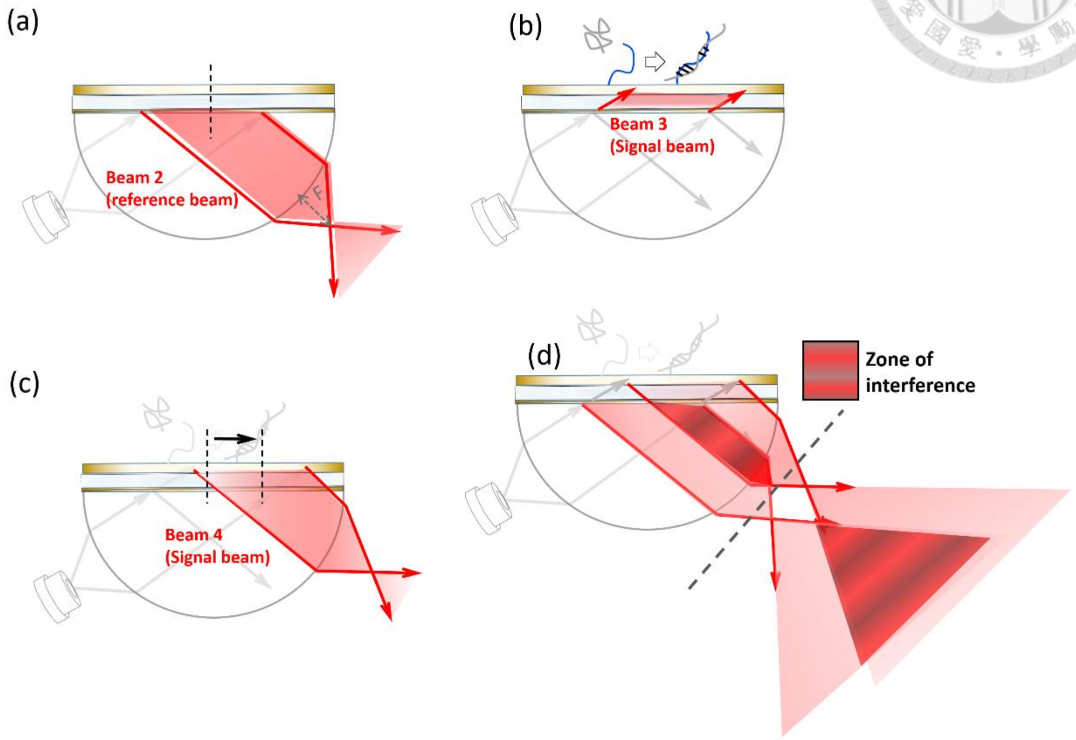

Fig. 11 Dispositif sensible à la phase développé.

La **Fig.** ***12*** représente l'atténuation caractéristique du faisceau signal lorsque l'angle correct est atteint, observée sur la caméra. Dans cet exemple, la réflexion sur l'interface du bas est réalisée par une couche de 8 nm d'or et une couche d'accroche de 2 nm de Cr. Le faisceau signal s'atténue notablement autour de l'angle Kretschmann (42.5°-43°). Les interférences restent très visibles quelque soient l'angle, ce qui indique la possibilité de déterminer la phase à la résonance mais aussi autour de la résonance. Le même effet peut être observé lorsque le milieu supérieur est recouvert d'eau. Dans ce cas, le couplage

doi:10.6342/NTU201700804

optimum se produit autour de 65°-66°, cf. **Fig.** ***12***

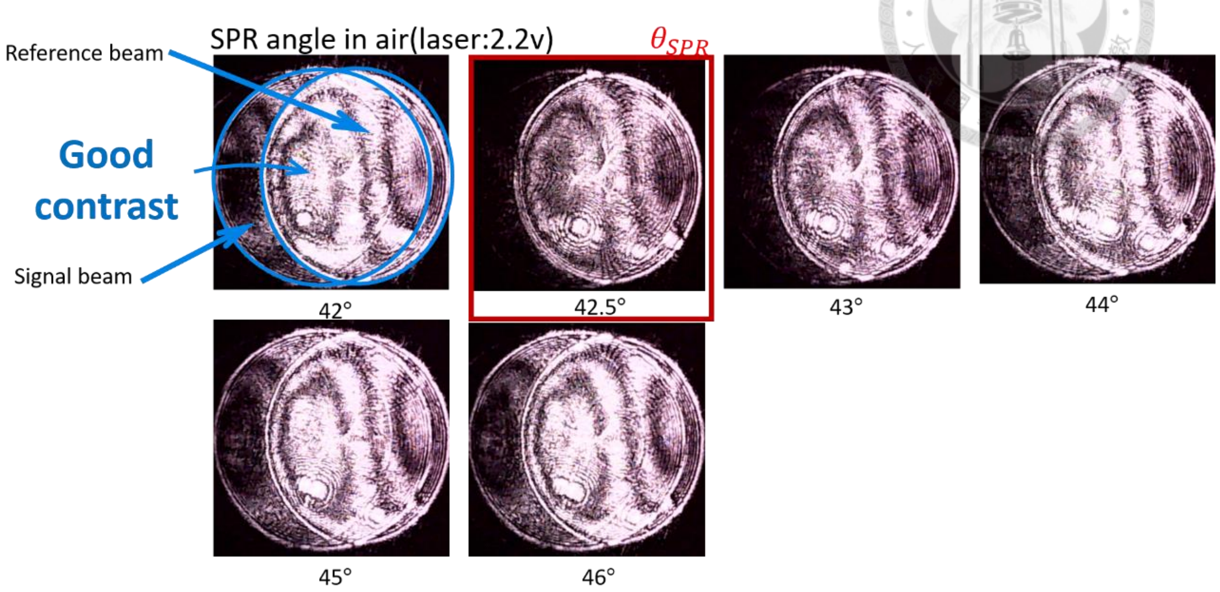

Fig. 12 Mesure dans l'air. Motif d'interférence du SiSPR dévelopé, observé à l'aide d'une caméra pour différents angles, autour de l'angle de Kretshmann.

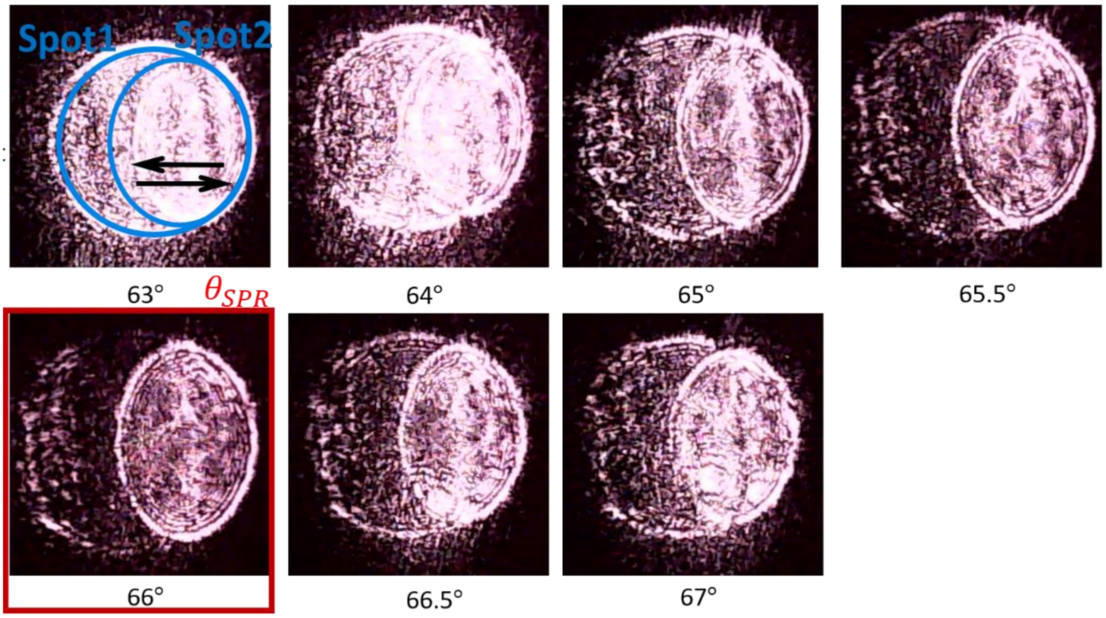

Fig. 13 Mesure dans l'eau. Mesure identique au cas précédent, lorsque le milieu supérieur est de l'eau. L'angle de Kretschmann est ici autour de 66°.

Méthode d'extraction de la phase

Dans les motifs d'interférences présentés précédemment, les informations d'amplitude et de phase sont mélangées. Pour les discriminer, une modulation de phase peut être employée. Dans notre approche, la modulation de phase est réalisée en modulant le courant d'injection du VCSEL. La légère modulation de longueur d'onde qui en résulte induit un déphasage entre les deux faisceaux, du fait que le chemin optique parcouru n'est pas le même entre le bras « signal » et le bras « référence ». La modulation de phase est ainsi introduite sans coût ni matériel supplémentaire. Le manuscrit détaille la méthode mise en place pour extraire en temps réel l'information de phase en présence d'une modulation sinusoïdale du courant d'injection (et de la phase). Pour des raisons de place, nous ne reprenons pas, dans ce résumé, le détail théorique de cette méthode. Mentionnons que l'effet de le modulation d'amplitude optique induite par la modulation de courant y est prise en compte, et que les conditions précises permettant d'extraire la phase dans ces conditions sont présentées. Pour arriver à ce résultat, le signal détecté est filtré de sa composante continue et une « détection synchrone généralisée » modifiée permettant de prendre en compte des modulations de phase relativement arbitraires (ici sinusoïdale) est employée. Cependant, il faut noter qu'il est nécessaire de connaitre et d'ajuster précisément la profondeur de modulation de phase *a*, ci-dessous, qui est fonction de la différence de chemin optique *L* entre les deux faisceaux de sortie, et de l'amplitude de modulation en longueur d'onde réalisée :

$$a = \frac{2\pi n L}{{\lambda_0}^2} S\,(di) \qquad \textbf{\textit{Eq. 1}}$$

où l'accordabilité en courant S est donnée par *dλ/di* et (di) représente l'amplitude de la modulation de courant, *n* est l'indice de la lame, λ_o est la longueur d'onde du VCSEL. Le dispositif permettant de déterminer S est représenté sur la **Fig.14** . Dans ce dispositif, un détecteur supplémentaire est utilisé pour normaliser les variations de puissances et étudier principalement les variations induites par la modulation de phase. La profondeur de modulation de phase réalisée est obtenue en comptant le nombre d'interférences constructives obtenue lors d’une période de modulation (nombre de pics). Pour obtenir une précision plus importante, une large différence de chemin optique peut être employée, ce qui permet d’avoir un nombre de franges important pour des modulations modestes (non représenté).

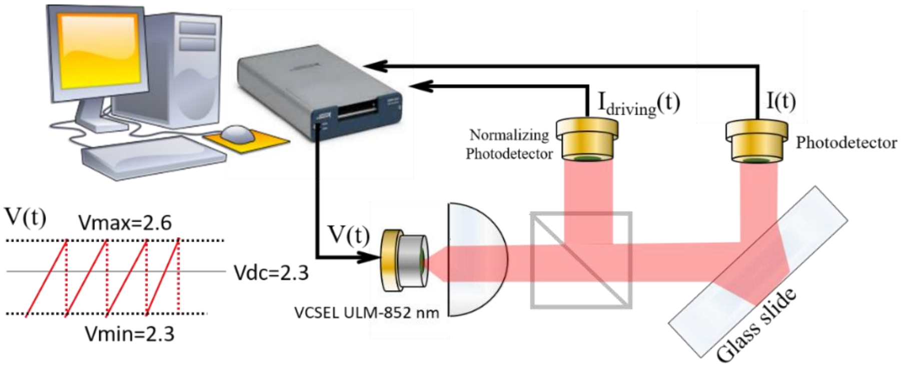

Fig. ***14*** Dispositif permettant d’estimer l’accordabilité S.

L’accordabilité des VCSELs testés est modeste (de l’ordre de 1nm/mA), si bien que tous ne permettent pas d’obtenir une modulation de phase suffisante pour des épaisseurs de verre standard, néanmoins beaucoup de modèles le permettent.

Mesures et discussion

Nous reprenons ici des exemples de mesures issues du manuscrit et permettant d’estimer la sensibilité RIU du SiSPR. La mesure est faite en plaçant dans le milieu supérieur des solutions de glucose de concentration croissante, et la puce est la même que précédemment. La mesure de phase associée est représentée **Fig.** ***15*** et la sensibilité du SiSPR à l’indice peut être tracé (**Fig. 16**), puisque l’indice de réfraction est connu pour chaque concentration. Une sensibilité de *6,4* 10^4 RIU est obtenue sur la pente maximale. A partir de cette courbe, la limite de détection en RIU peut être déterminée connaissant le

doi:10.6342/NTU201700804

bruit de phase. Le calcul de l'écart type sur les traces de signaux donne une valeur de *0.051°*, ce qui correspond à une limite de détection raisonable de *0.153°*. La limite de détection ainsi calculée est autour de *2,3* 10^{-6} RIU, et la plage dynamique est de *7,0* 10^{-3} RIU.

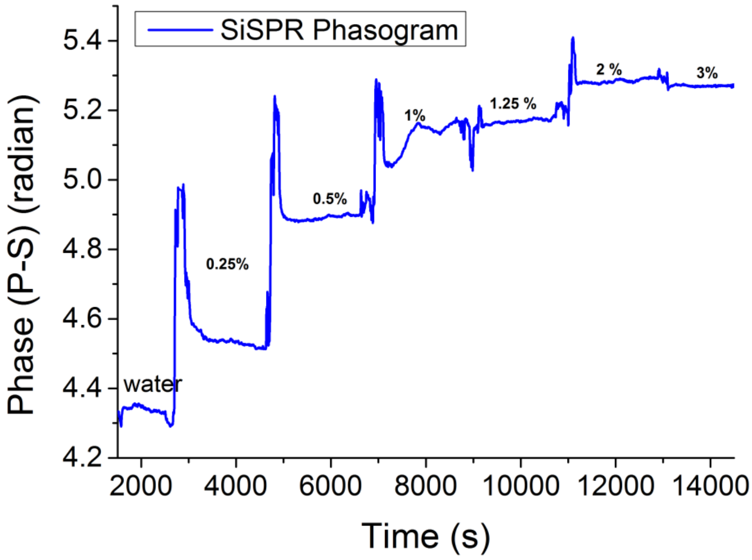

Fig. 15 Mesure de phase à l'aide du SiSPR sur des solutions de glucose de concentration croissante.

Comme nous l'avons mentionné, la sensibilité obtenue excède d'un facteur 10 les performances usuellement reportées pour des mesures en amplitude dans des conditions similaires (longueur d'onde, matériau), qui se situent souvent en deçà de 10^{-5} RIU. Au cours de cette thèse, plusieurs prototypes fonctionnels du SiSPR ont été réalisés. Une version relativement compacte, en vue d'application sur portable est représentée sur la

doi:10.6342/NTU201700804

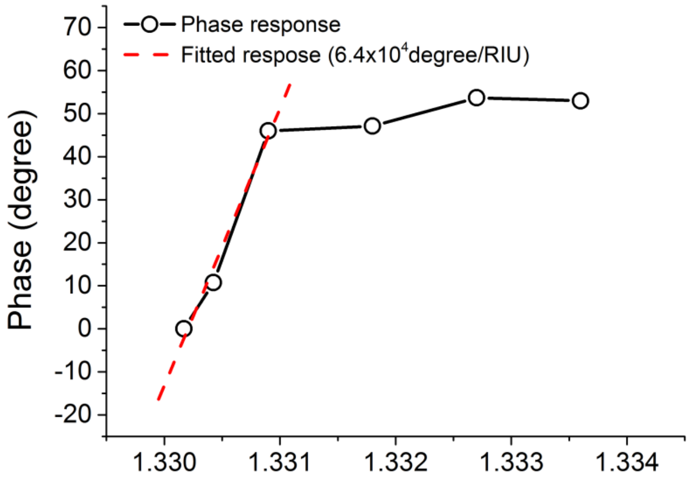

Fig. 16Réponse en phase du SiSPR, donnée en fonction de l'indice de réfraction.

Fig. *17*

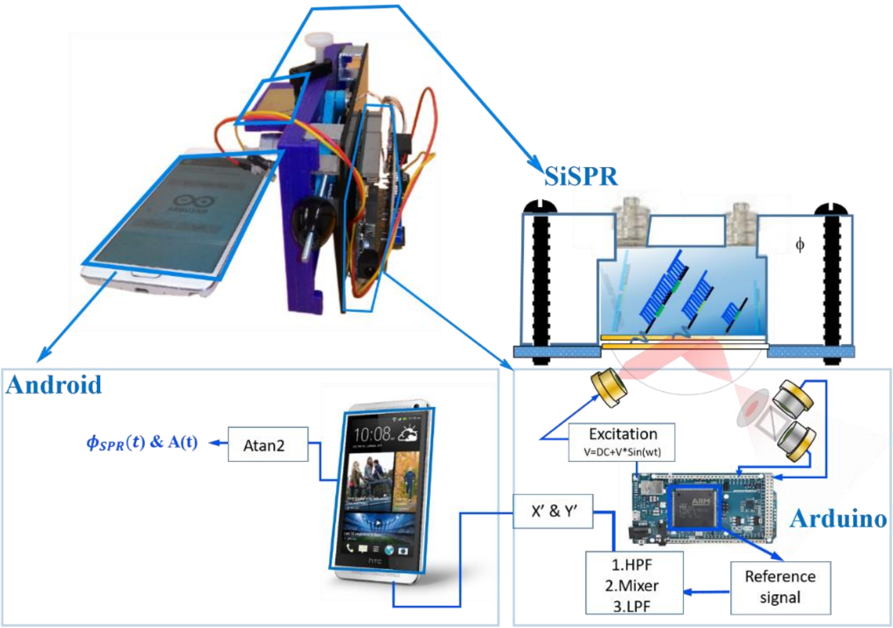

Fig. 17 Exemple de version compacte du SiSPR, réalisée dans cette thèse .

References

1. S. Verma, A. Robinson and P. Dutta, presented in part at the Proceedings of the 10th ACM Conference on Embedded Network Sensor Systems, Toronto, Ontario, Canada, 2012.
2. A. Lopez Gerardo, M. C. Estevez, M. Soler and M. Lechuga Laura, *Nanophotonics*, 2016, **6**, 123.
3. Q. Wei, R. Nagi, K. Sadeghi, S. Feng, E. Yan, S. J. Ki, R. Caire, D. Tseng and A. Ozcan, *ACS Nano*, 2014, **8**, 1121-1129.
4. L. Jiang, M. Mancuso, Z. Lu, G. Akar, E. Cesarman and D. Erickson, *Scientific Reports*, 2014, **4**, 4137.
5. OECD, Health care expenditure per GDP, http://stats.oecd.org/Index.aspx?DataSetCode=SHA).
6. C. L. Petersen, T. P. Chen, J. M. Ansermino and G. A. Dumont, *Sensors*, 2013, **13**, 16882-16893.
7. P. Preechaburana, M. C. Gonzalez, A. Suska and D. Filippini, *Angewandte Chemie*, 2012, **51**, 11585-11588.
8. L. Shen, J. A. Hagen and I. Papautsky, *Lab On a Chip*, 2012, **12**, 4240-4243.
9. A. I. Barbosa, P. Gehlot, K. Sidapra, A. D. Edwards and N. M. Reis, *Biosensors and Bioelectronics*, 2015, **70**, 5-14.
10. S. Agarwal, A. E. LeFevre, J. Lee, K. L’Engle, G. Mehl, C. Sinha and A. Labrique, *BMJ*, 2016, **352**.
11. S. Vashist, E. Schneider and J. Luong, *Diagnostics*, 2014, **4**, 104-128.
12. H. Li and L. Rothberg, *Proceedings of the National Academy of Sciences of the United States of America*, 2004, **101**, 14036-14039.
13. S. R. Steinhubl, E. D. Muse and E. J. Topol, *Science translational medicine*, 2015, **7**, 283rv283-283rv283.
14. E. A. Tyburski, S. E. Gillespie, W. A. Stoy, R. G. Mannino, A. J. Weiss, A. F. Siu, R. H. Bulloch, K. Thota, A. Cardenas, W. Session, H. J. Khoury, x, S. Connor, xE, S. T. Bunting, J. Boudreaux, C. R. Forest, M. Gaddh, T. Leong, L. A. Lyon and W. A. Lam, *The Journal of Clinical Investigation*, 2014, **124**, 4387-4394.
15. C.-C. Chang, C.-P. Chen, C.-H. Lee, C.-Y. Chen and C.-W. Lin, *Chemical Communications*, 2014, **50**, 14443-14446.
16. C.-C. Chang, S. Lin, C.-H. Lee, T.-L. Chuang, P.-R. Hsueh, H.-C. Lai and C.-W. Lin, *Biosensors and Bioelectronics*, 2012, **37**, 68-74.
17. Y.-S. Kuo, *Proceedings of the First ACM Symposium on Computing for Development*

doi:10.6342/NTU201700804

Article, 2010 **24**.

18. J. I. Hong and B.-Y. Chang, *Lab on a Chip*, 2014, **14**, 1725-1732.
19. J. F. Masson, L. Obando, S. Beaudoin and K. Booksh, *Talanta*, 2004, **62**, 865-870.
20. T.-L. Chuang, C.-C. Chang, Y. Chu-Su, S.-C. Wei, X.-h. Zhao, P.-R. Hsueh and C.-W. Lin, *Lab on a Chip*, 2014, **14**, 2968-2977.
21. S. K. Vashist, T. van Oordt, E. M. Schneider, R. Zengerle, F. von Stetten and J. H. T. Luong, *Biosensors and Bioelectronics*, 2015, **67**, 248-255.
22. J. R. Askim and K. S. Suslick, *Analytical Chemistry*, 2015, **87**, 7810-7816.
23. G. Marriott, S. Mao, T. Sakata, J. Ran, D. K. Jackson, C. Petchprayoon, T. J. Gomez, E. Warp, O. Tulyathan, H. L. Aaron, E. Y. Isacoff and Y. Yan, *Proceedings of the National Academy of Sciences of the United States of America*, 2008, **105**, 17789-17794.
24. Y. H. Huang, H. P. Ho, S. Y. Wu and S. K. Kong, *Advances in Optical Technologies*, 2012, **2012**, 12.
25. C.-C. Chang, S.-C. Wei, T.-H. Wu, C.-H. Lee and C.-W. Lin, *Biosensors and Bioelectronics*, 2013, **42**, 119-123.
26. L. J. Steven, *Physics in Medicine and Biology*, 2013, **58**, R37.
27. E. Stern, A. Vacic, N. K. Rajan, J. M. Criscione, J. Park, B. R. Ilic, D. J. Mooney, M. A. Reed and T. M. Fahmy, *Nature Nanotechnology*, 2010, **5**, 138-142.
28. S.-C. Hsieh, C.-C. Chang, C.-C. Lu, C.-F. Wei, C.-S. Lin, H.-C. Lai and C.-W. Lin, *Nanoscale Research Letters*, 2012, **7**, 180-180.
29. M. Pawula, Z. Altintas and I. E. Tothill, *Talanta*, 2016, **146**, 823-830.
30. Y. H. Huang, H. P. Ho, S. K. Kong and A. V. Kabashin, *Annalen der Physik*, 2012, **524**, 637-662.
31. A. J. T. Richard B M Schasfoort, *Handbook of Surface Plasmon Resonance*, RSC, 2008.
32. B. Sepulveda, L. G. Carrascosa, D. Regatos, M. A. Otte and D. Farina, *Proceedings of SPIE 7397, Biosensing II*, 2009, **73970Y**
33. P. P. Markowicz, W. C. Law, A. Baev, P. N. Prasad, S. Patskovsky and A. Kabashin, *Opt. Express*, 2007, **15**, 1745-1754.
34. C.-M. Wu, Z.-C. Jian, S.-F. Joe and L.-B. Chang, *Sensors and Actuators B: Chemical*, 2003, **92**, 133-136.
35. Y. Wu, H. P. Ho, C. L. Wong, S. K. Kong and L. Chinlon, *Sensors Journal, IEEE*, 2007, **7**, 70-73.
36. S.-P. Ng, C.-M. L. Wu, S.-Y. Wu, H.-P. Ho and S. K. Kong, *Biosensors and Bioelectronics*, 2010, **26**, 1593-1598.
37. A. V. Kabashin and P. I. Nikitin, *Optics Communications*, 1998, **150**, 5-8.
38. T. M. Chinowsky, J. G. Quinn, D. U. Bartholomew, R. Kaiser and J. L. Elkind, *Sensors and Actuators B: Chemical*, 2003, **91**, 266-274.

doi:10.6342/NTU201700804

39. W. J. Bates, *Proceedings of Physical Society*, 1947, **59**, 6.

40. A. Al Mohtar, J. Vaillant, Z. Sedaghat, M. Kazan, L. Joly, C. Stoeffler, J. Cousin, A. Khoury and A. Bruyant, *Opt. Express*, 2014, **22**, 22232-22245.

41. S. Ekgasit, C. Thammacharoen, F. Yu and W. Knoll, *Applied Spectroscopy*, 2005, **59**, 661-667.

42. H. Jo, H. Gu, W. Jeon, H. Youn, J. Her, S.-K. Kim, J. Lee, J. H. Shin and C. Ban, *Analytical Chemistry*, 2015, **87**, 9869-9875.

43. M. Darmostuk, S. Rimpelova, H. Gbelcova and T. Ruml, *Biotechnology Advances*, 2015, **33**, 1141-1161.

44. P. O. Collinson, F. G. Boa and D. C. Gaze, *Annals of Clinical Biochemistry*, 2001, **38**, 423-449.

45. K. A. Peterlinz, R. M. Georgiadis, T. M. Herne and M. J. Tarlov, *Journal of the American Chemical Society*, 1997, **119**, 3401-3402.

46. A. W. Peterson, R. J. Heaton and R. M. Georgiadis, *Nucleic Acids Research*, 2001, **29**, 5163-5168.

47. R. M. Dirks and N. A. Pierce, *Proceedings of the National Academy of Sciences of the United States of America*, 2004, **101**, 15275-15278.

48. S. K. Vashist, M. Saraswat and H. Holthšfer, *Procedia Chemistry*, 2012, **6**, 184-193.

49. J. A. Lofgren, S. Dhandapani, J. J. Pennucci, C. M. Abbott, D. T. Mytych, A. Kaliyaperumal, S. J. Swanson and M. C. Mullenix, *The Journal of Immunology*, 2007, **178**, 7467-7472.

50. C.-Y. Yang, E. Brooks, Y. Li, P. Denny, C.-M. Ho, F. Qi, W. Shi, L. Wolinsky, B. Wu, D. T. W. Wong and C. D. Montemagno, *Lab on a Chip*, 2005, **5**, 1017-1023.

doi:10.6342/NTU201700804